

Ultrasonic modeling : Application to deep-water multiples imaging

by

Philippe Guérendel

Ingenieur de l'Ecole Centrale de Lyon - France -

Submitted to the Department of Earth, Atmospheric, and Planetary Sciences

in partial fulfillment of the requirements for the degree of

Master of Science

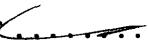
at the

MASSACHUSETTS INSTITUTE OF TECHNOLOGY

September 1990

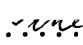
© Massachusetts Institute of Technology 1990

All rights reserved

Signature of Author 

Department of Earth, Atmospheric, and Planetary Sciences

August 10, 1990

Certified by 

M. Nafi Toksöz

Professor of Geophysics

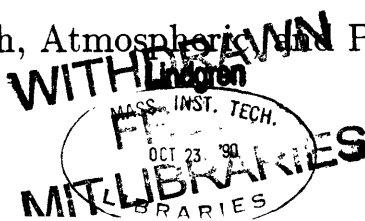
Thesis Advisor

Accepted by

Thomas H. Jordan

Chairman

Department of Earth, Atmospheric and Planetary Sciences



Ultrasonic modeling : Application to deep-water multiples imaging

by

Philippe Guérendel

Submitted to the Department of Earth, Atmospheric, and Planetary Sciences
on August 10, 1990 in partial fulfillment of the requirements for the
Degree of Master of Science in Geophysics

Abstract

The technique of ultrasonic modeling is used to demonstrate the imaging of subsurface deep-water multiples in typical marine seismic environment, using a ray-based Kirchhoff 2D pre-stack depth migration. Two separate experiments are carried out in an ultrasonic modeling water-tank. The first represents a two-layer structure separated by a plane interface dipping 10 degrees. The model is constructed using neoprene over aluminum. The recording geometry consists of an ocean-bottom hydrophone (O.B.H) and a line array of 72 sources. The image produced by combining the primary and the water multiple reflections is much better than that obtained using the primary reflection alone. The effect of post-critical reflections is studied. In a second experiment, a three-layer model with a fault is imaged with a water bottom streamer configuration. Joint migration of primaries and multiples improve the image. For both models, synthetic seismograms are computed and migrated. These are compared with the results of ultrasonic experiments in order to illustrate the resolution and reliability of the ultrasonic acquisition. Characteristics of ultrasonic modeling such as scaling factor, transducers, signal-to-noise ratio, modeling materials are studied and implemented in the actual experiments.

Thesis Advisor: M. Nafi Toksöz

Title: Professor of Geophysics

Acknowledgements

I would like to thank my advisor M. Nafi Toksöz for his valuable help, advice and guidance. I am grateful to him for providing me the opportunity to learn and enjoy ultrasonic modeling.

Ed Reiter taught me basic seismic processing and spends a lot of time to help and advise me. I warmly thank him.

Many thanks to Bob Cicerone who just did not correct the spelling (spelling !) and grammar of that page in the first phase and Wenji Dong for the interest he shares with me on some ultrasonic data.

The Earth Resources Laboratory is an enjoyable environment and I thank its staff and students. Jeff Meredith, Jack Foley, Chuck Doll, Sadi Kuleli, Burc Oral, Delaine Thompson, Rick Gibson, Xiaming Tang, Frederic Lefevre and many others provide me help in geophysics and computer matters. Fatih Guler taught me a lot about turkish songs and ultrasonics. I thank Roger Turpening for interesting discussions and Sara Brydges, Naida Buckingham, Sue Turbak, and Liz Henderson for providing me help in administrative matters.

This thesis was supported by the Founding Members Earth Resources Laboratory and by Oyo Corporation development grant.

Contents

1	Imaging with deep water multiples	2
1.1	General introduction	2
1.2	Multiple imaging scheme	3
1.3	Application	5
1.4	Computer programs	6
1.4.1	Depth migration program	6
1.4.2	Synthetic seismogram modeling program	7
2	Ultrasonic modeling	13
2.1	Introduction	13
2.2	Water tank	14
2.3	Acquisition devices	14
2.4	Transducers	16
2.4.1	General comments	16
2.4.2	Frequency response	16
2.4.3	Directivity pattern	19
2.4.4	Transducer applications	20
2.4.5	Backscattering	21
2.4.6	Choice of transducers	21
2.4.7	Transmitter	21
2.4.8	Receiver	22

2.4.9	Signal to noise optimization	23
2.5	Models	23
2.5.1	Modeling materials	24
2.5.2	Multi-layer models	25
2.6	Scale factor	26
3	Dip interface imaging of a two-layer model	34
3.1	Introduction	34
3.2	Description of the set-up	34
3.3	Raw data	36
3.3.1	Ultrasonic data	36
3.3.2	Synthetic data	38
3.4	Images	40
3.4.1	Dip filter	40
3.4.2	Ultrasonic data	40
3.4.3	Synthetic data	41
4	Fault unconformity model ; Conclusion	67
4.1	Description	67
4.2	Raw data	68
4.2.1	Ultrasonic data	68
4.2.2	Synthetic data	69
4.3	Images	70
4.3.1	Ultrasonic data	70
4.3.2	Synthetic data	71
4.4	General conclusion	71
4.4.1	Ultrasonic modeling	71
4.4.2	Ultrasonic experiments	72
4.4.3	Water-multiple imaging	73

A	Piezoelectricity and transducer applications	93
B	Transmitter power and receiver sensitivity	96
C	Source wavelet improvement	102
D	Acoustical properties of materials	104
E	Additional comments on the transmitter	107
F	Deconvolution of the ultrasonic time sections	111
	F.1 Introduction	111
	F.2 Time domain deconvolution	111
	F.2.1 Theory	111
	F.2.2 Application	112
	F.3 Frequency domain	113
G	Fault-syncline model	115
	References	118

Chapter 1

Imaging with deep water multiples

1.1 General introduction

In a typical marine seismic survey, primary and water-multiple reflections usually overlap. Predictive deconvolution allows one to recover the primary wavefield, provided that the geologic structures are simple (nearly flat beds). More generally, velocity analysis, such as hyperbolic τ - p velocity filtering (Mitchell and Kelamis, 1990) allows one to better separate primary and multiple wavefields, and the latter might also be processed.

In deep-water, the primary and multiple reflections are separated enough to make a direct analysis of the water-multiple wavefield possible. Reiter et al. (1990) show that the multiple wavefield can be processed when recorded by an ocean-bottom hydrophone (O.B.H) in soft marine sediments. The theoretical basis of such an analysis is described in the next section.

In this study, the multiple imaging scheme developed by Reiter et al. (1990) is applied to water-tank ultrasonic modeling data with a dual purpose:

- To test the deep-water multiple imaging technique for the delineation of typical geological structures, and evaluate its advantages.

- To validate ultrasonic modeling as a reliable and useful technique for obtaining complete wavefield seismic data.

Time computation in three-dimensional (3D) complete-wavefield modeling techniques, such as finite difference, complexity due to inhomogeneity and anisotropy are nowadays the key issues in producing reliable synthetic seismograms. Hence, the ultrasonic technique can be a valuable alternative, provided that it can generate in a short time high quality data from models, which faithfully portray a given geological structure. This requirement involves proper scaling, receiver and source characteristics, material and model construction, and are discussed in the next chapter. Although 3D water-tank modeling is the main focus in this thesis, most of the discussion can be applied to 3D and 2D solid modeling.

None of the two issues mentioned above take place for our purpose since simple 2D1/2 models are implemented. However, it is important that an adequate acquisition scheme be realized. In particular, the ultrasonic set-up must faithfully portray the kinematic of the problem, i.e., the receiver position has to be scaled correctly to a true O.B.H.

Two models have been used:

- A simple two-layer model with the interface dipping 10 degrees and an O.B.H receiver.
- A fault unconformity, three-layer model with a water-bottom streamer.

The corresponding synthetic models have been generated for comparison. Chapter 3 and 4 discuss the main results.

1.2 Multiple imaging scheme

For the first water-multiple, two sets of data are included, as shown in figure 1-1:

- The receiver multiple,

- The source multiple.

When a receiver is at the surface of the water, the receiver multiple and source multiple rays which have the same travel-time come from two different image points. Their amplitudes are of the same order and one cannot differentiate them in the data (figure 1-2). In that case, the multiple information is useless.

On the other hand, in the case of an ocean-bottom receiver, the ratio between the source multiple amplitude and the receiver multiple equivalent travel-time amplitude is $R/(1+R)$ at normal incidence where R is the reflection coefficient of the water bottom layer (figure 1-3). This ratio ranges over 0 and 0.5 and is usually very small. The bottom layer most often is a highly porous sedimentary layer with a P velocity ranging from 1600 m/s to 2200 m/s and density from 1.1 to 1.4 g/cc. For these values, R is between 0.08 and 0.35 and $R/(1+R)$ between .075 and .26. Therefore, most energy in the first water multiple data set come from the receiver multiple. In terms of a ray-based migration scheme:

- Migrating along the receiver multiple path gives a strong image with a small artifact due to the source multiple energy.
- Migrating along the source multiple path gives a poor image blurred by a strong artifact due to the receiver multiple energy.

In the first case, the reflectors are well imaged whereas in the second case, they are not. Reiter et al. (1990) have illustrated this with a simple dipping interface. Consequently, reflectors can be accurately imaged by migrating the multiple data only along the receiver multiple path. Advantages of the method are:

- The improvement of the signal-to-noise ratio by the addition of both primary and multiple images.
- The lateral extension of the image due to the coverage of the receiver multiple rays (figure 1-4).

- If the point of a reflector (e.g nearly flat) is impinged by both rays, the receiver multiple ray angle of incidence θ_m with that reflector is larger than the primary ray angle θ_p (figure 1-5). When θ_p is close or greater than the critical angle, the reconstruction of the reflector by the migration routine is deteriorated due to the phase shift of the post-critical reflected wave. This is discussed in chapter 3. In a more general case, the angle consideration implies that a receiver multiple image is less affected by the head waves, converted waves, and layer multiples waves than the primary image within the same imaging zone.
- The receiver multiple ray amplitude is slightly larger than the primary ray amplitude for deep reflectors. Indeed, for the O.B.H, the contribution of the bottom reflection for the incoming multiple ray is $(1+R)$ greater than the primary (figure 1-3). The geometric spreading factor is not included here but the water column path difference has no significant effect in the amplitude ratio for deep reflectors.

The second water multiple (figure 1-6) does not provide the advantage that the first receiver multiple does because two sets of water multiples have similar amplitudes but their equivalent travel-time rays impinge two different image points.

1.3 Application

The use of a digitally recorded in-situ O.B.H (Koelsch et al., 1982) is an experimental set-up. On the other hand, the technology of water bottom streamers and hydrophones (e.g. HC2002¹, classical seismic 2000 meters depth capability hydrophone) is available. The multiplexing and digital technology can be easily used to transmit the seismic signals via a standard streamer cable or a 7-conductors Schlumberger cable as it is done for the multilock V.S.P tool². Direct advantages of ocean-bottom

¹trademark I.F.P - Geomecanique

²trademark I.F.P - C.G.G

recording are:

- Improvement of the signal-to-noise ratio, mainly due to the low level ambient noise.
- The ability to record large source-receiver offset data, providing for the possibility of converted waves processing.
- The possibility of processing the first water-multiple reflections as shown above, either directly in deep water or with a velocity analysis scheme to separate primary and multiple wavefield.

For example, Reiter et al. (1990) succeeded in imaging very deep reflectors, blurred in the conventional C.M.P surface data gather.

Other challenges are the supplementary use of well-coupled ocean bottom seismometers (O.B.S) to provide velocity information in addition to the hydrophone data, and the implementation of very long movable streamers, as it has been done in the ultrasonic experiment of chapter 4.

1.4 Computer programs

1.4.1 Depth migration program

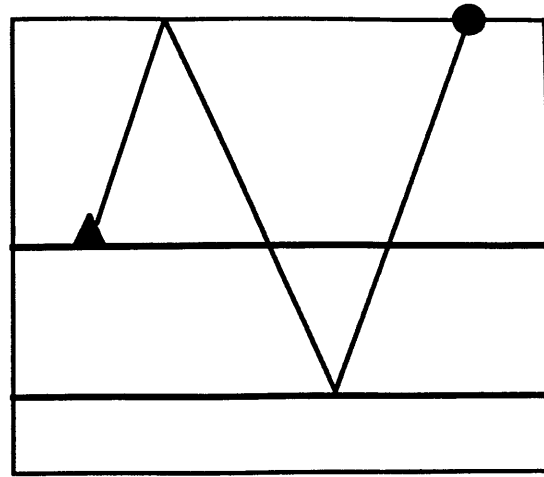
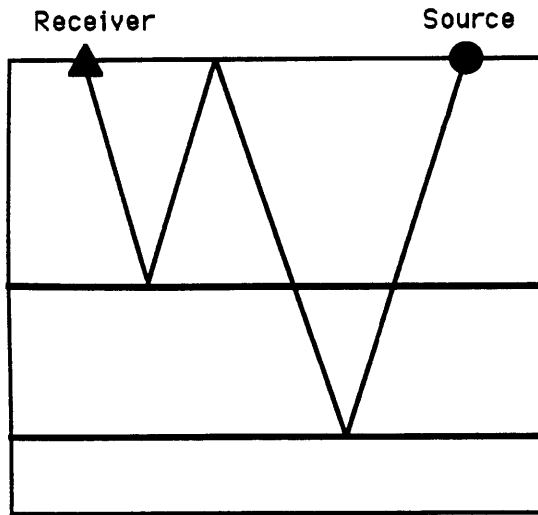
The imaging of the primary and multiple data has been performed by a ray equation based 2-D pre-stack Kirchhoff depth migration code written by Reiter. The image zone is defined by a set of dense space-image points. The velocity model above the reflector to be imaged is assumed to be known. In the multi-layer case, the program can be run iteratively and at each step, the velocity model can be improved by entering the updated spatial coordinates of the reflector previously imaged. A fan of rays are shot from the image points to the source and to the receiver, and the Green's functions are calculated. Any ray path can be chosen in this approach and it provides the capability of migrating any water-multiple path. Once done, an

interpolation routine is used to calculate the Green's functions at each image point. The primary or multiple data are then extrapolated along the receiver path and imaged at the source path travel-time.

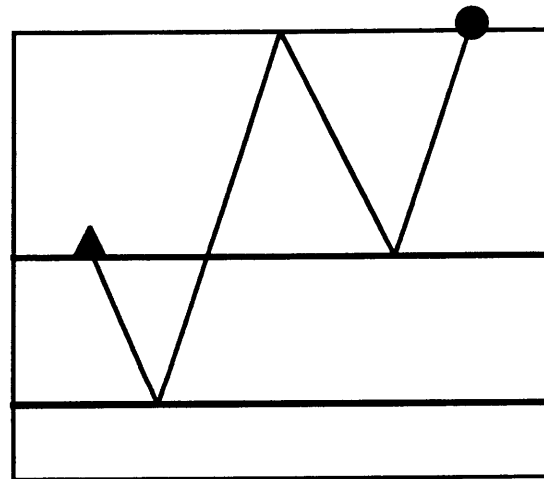
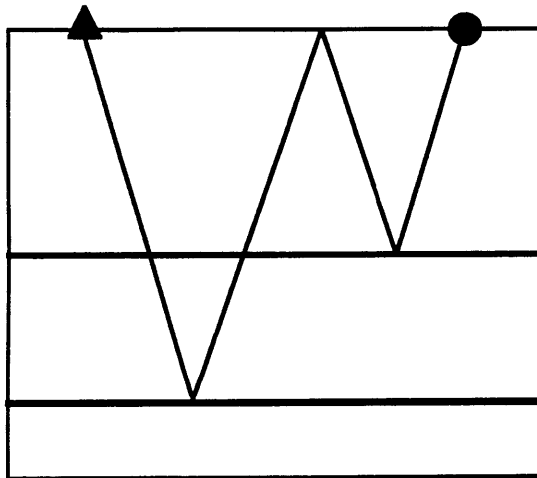
1.4.2 Synthetic seismogram modeling program

Ray tracing and computation of the synthetic seismogram have been performed by the 2D code SEIS3 developed by Cerveny et al. (1977), including a 3D geometric spreading and absorption factor. A cubic-spline interpolation routine is used to define the interfaces. Discontinuities are allowed. P and S layer velocities and densities allow a true plane wave computation of the reflection coefficient. Synthetic seismograms are generated from the convolution of the reflection serie with a zero-phase wavelet defined by a harmonic function modulated by a Gaussian envelope. Vertical or horizontal components can be plotted. In our O.B.H and multiple source configuration, receiver and source are reciprocally inverted. It turns out that the cosine-like directivity pattern of a vertical receiver in the synthetic time section is similar to the directivity pattern of the transmitter in the ultrasonic time section and further comparison between amplitudes is possible (cf figure 2-11 and chapter 3).

Receiver Multiple Ray



Source Multiple Ray



Surface Receiver

Water bottom Receiver

Figure 1-1: Kinematics of the first water multiple rays.

Surface hydrophone case

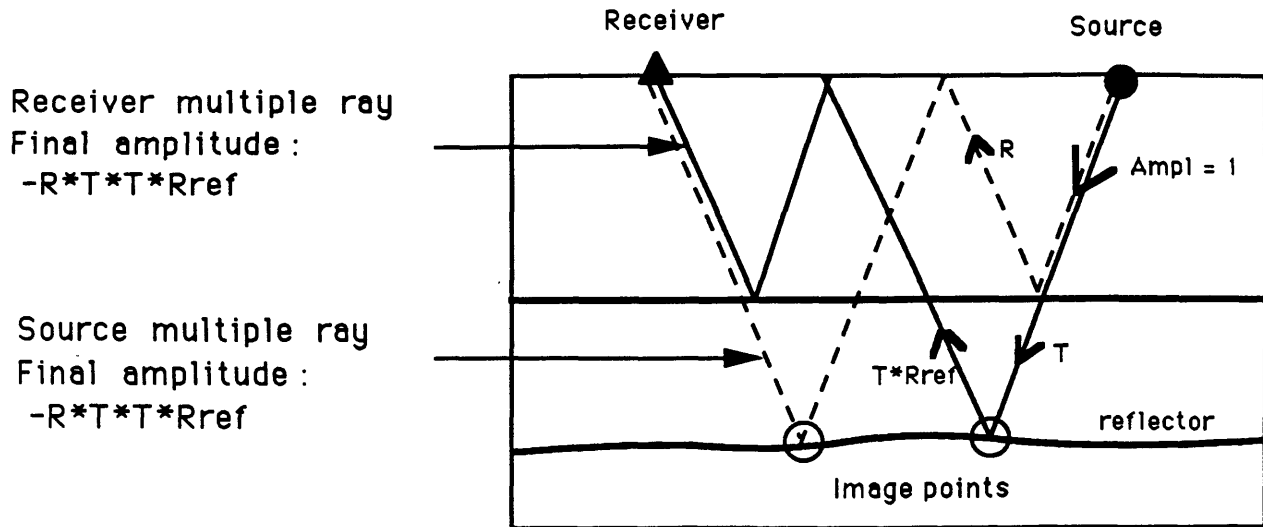


Figure 1-2: Multiple ray amplitudes in the surface receiver case.

Ocean bottom hydrophone case

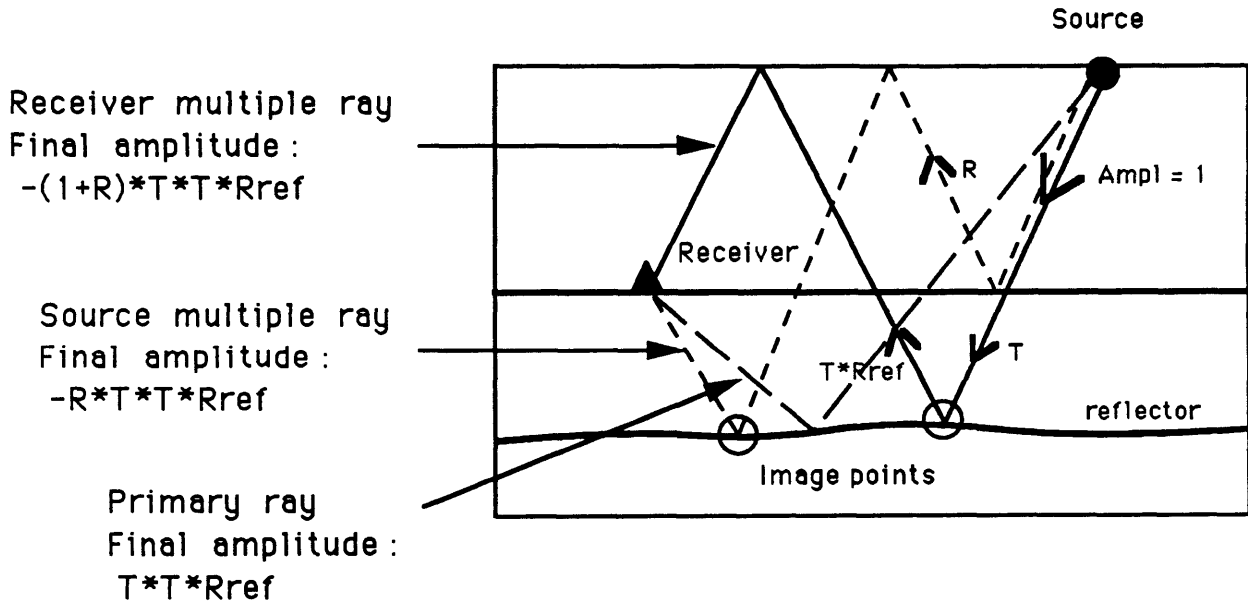
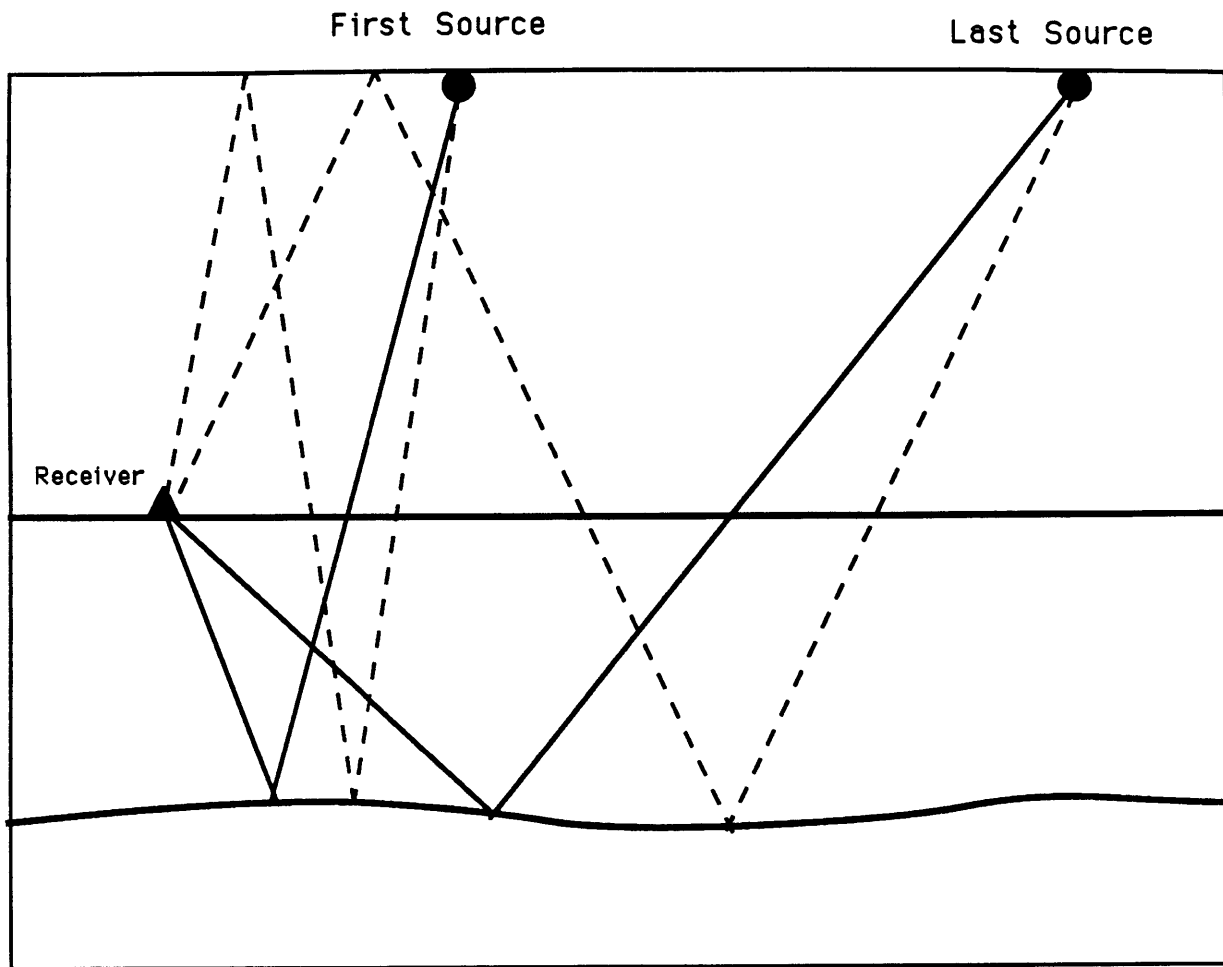



Figure 1-3: Multiple ray amplitudes plus primary ray amplitude in the bottom receiver case.




 Primary rays coverage



 Receiver multiple rays coverage

Figure 1-4: Coverage of primary and receiver multiple rays.

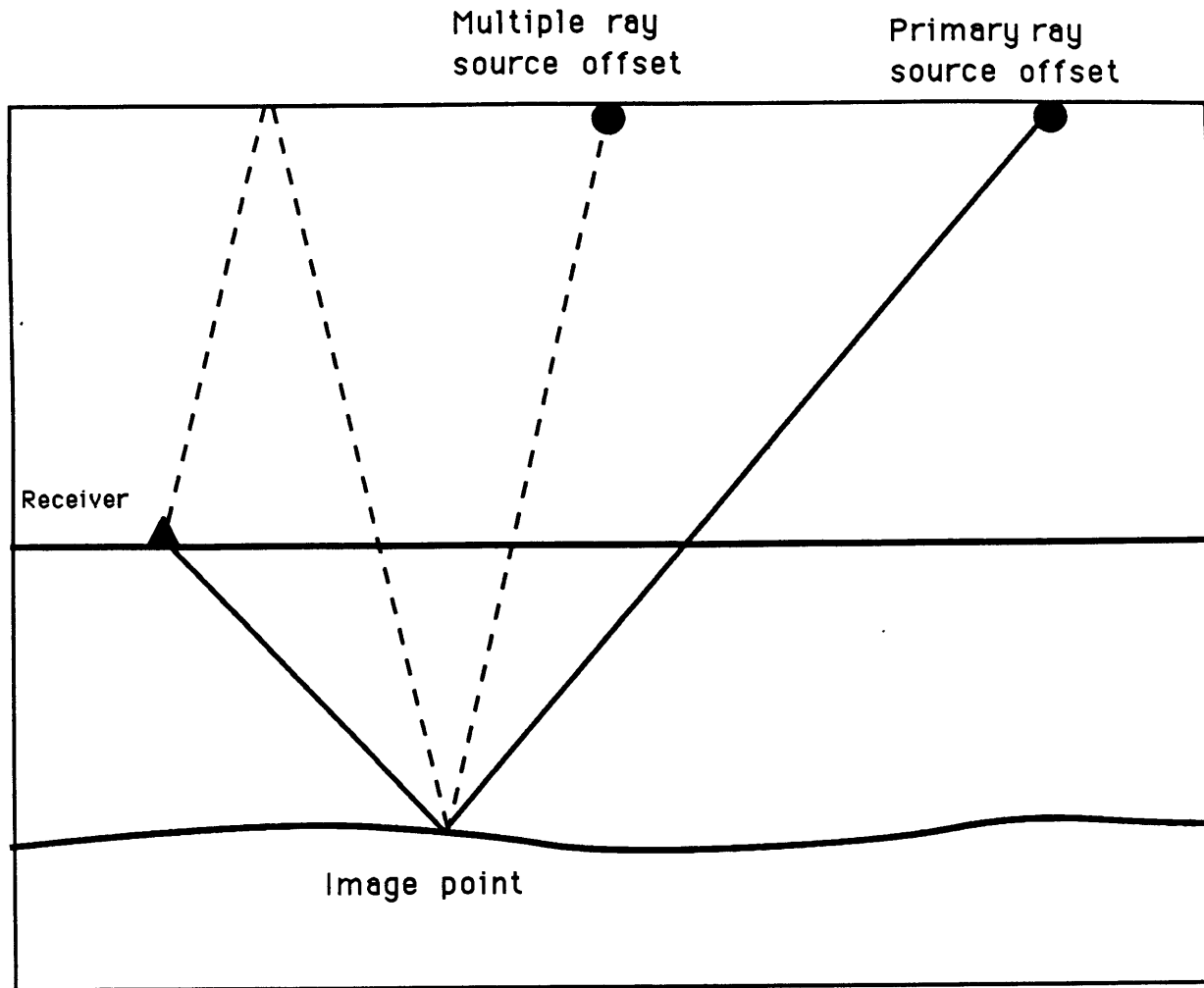
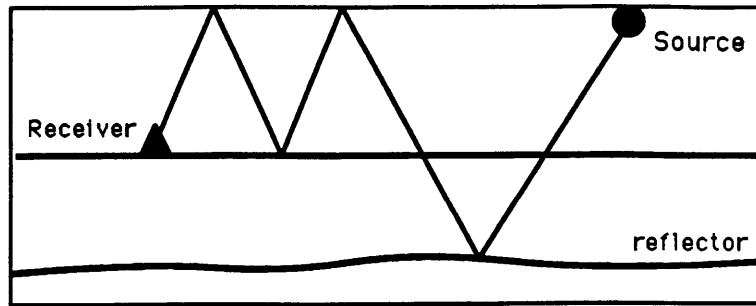


Figure 1-5: Angle of incidence for primary and receiver multiple rays.

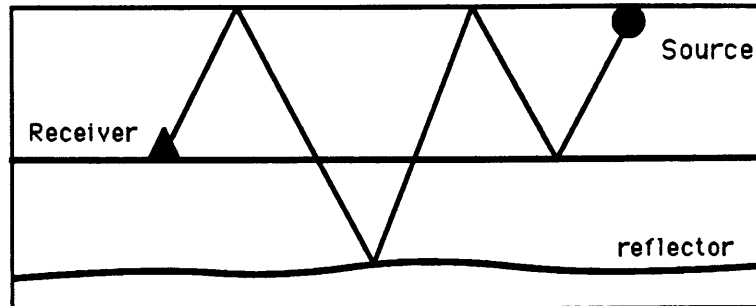
Receiver - Receiver
Multiple ray

Final Amplitude :
 $(1+R)*R*T*T*R_{ref}$



Source - Receiver
Multiple ray

Final Amplitude :
 $(1+R)*R*T*T*R_{ref}$



Source - Source
Multiple ray

Final Amplitude :
 $R*R*T*T*R_{ref}$

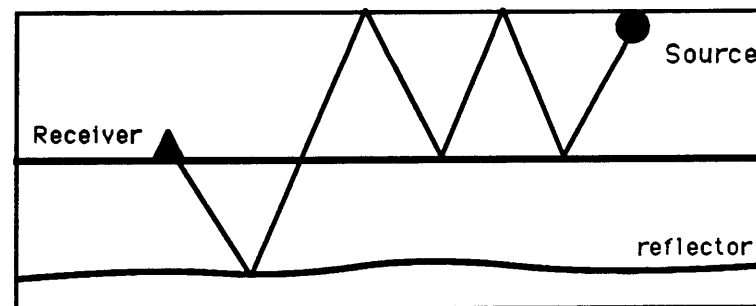


Figure 1-6: Second water multiple ray amplitudes in the bottom receiver case.

Chapter 2

Ultrasonic modeling

2.1 Introduction

This chapter describes the main characteristics of the three-dimensional (3D) water-tank ultrasonic facility. The parameters chosen for our experiments are optimum for scaling earth structures and are more generally discussed for setting up different types of experiments. Additional comments, figures, tables, details of computations and new ideas are including in the appendices.

In general, values between 100Khz and 1Mhz are a reasonable maximum frequency for the frequency range used in 3D ultrasonic modeling. This corresponds to wavelengths from 3mm to 30mm in materials whose velocity is 3000m/s. Below 100Khz, costly large tank and large models are needed. Beyond 1Mhz, source and receiver characteristics are difficult to scale correctly, and the required resolution increases the difficulties of setting up the experiment. In addition, acoustic properties and homogeneity of materials may vary from the values at the scaled frequency. Consequently, the scaling factor defined as ratio of field dimensions to laboratory dimensions typically ranges from 1000 to 10000 for the usual seismic frequency range of about 100Hz.

This range can be kept for 3D solid modeling but is divided by a factor 4 in the

2D solid modeling.

2.2 Water tank

The water-tank (figure 2-1) is made of stainless steel and measures 40" long by 24" wide by 20" high and equipped with two bridges. Transducers are attached to these bridges and can move along the three axes. The resolution in x, y is 0.0025" and 0.001" in z . Motion is provided by six step motors controlled by a step-motor SLO-SYN indexer whose output current can be switched by a switch-control unit HP3488, which is controlled by a PC computer.

Proper leveling and stability of the tank are important. In particular, the sharp step motion of the bridges produces vibrations which may cause either improper positioning of transducers or slight movement of the model in the tank. It is recommended to rigidly anchor the tank. Although not implemented in the E.R.L water tank, the other recommended tank devices include the ability to rotate around the z axis, a water-level controlled unit to prevent level changes due to evaporation during long runs, and a water filtering unit whose parameters must be optimized to reduce air bubbles.

2.3 Acquisition devices

The block diagram in figure 2-1 shows the acquisition devices:

- A Panametrics ultrasonic pulser excites the transmitter with a voltage pulse of typically 200Volts RMS and $1\mu s$ pulse width. Ultrasonic excitation is discussed in appendix C for resolution wavelet improvement purpose. The pulse repetition must be chosen to be compatible with the averaging-speed capability of the oscilloscope and taking into account the noise. The experimentalist must choose the repetition rate as a function of the time it takes for the signal-generated noise

to die down and the water-tank to return to its normal background condition. We have used a pulse repetition of 8Hz.

- A low noise (typically $0.8\mu\text{V}$ pp equivalent-input), AC, high impedance ($5\text{ M}\Omega$) preamplifier manufactured by S.E.A. It amplifies the receiver signal 17db gain and has a 40Khz-30Mhz bandwidth (3db points).
- A Panametrics 5660B preamplifier with a switchable 40 or 60db gain is used as an amplifier. It has an equivalent input noise of $5.0\mu\text{V}$ pp and a 20Khz-2Mhz 3db bandwidth.
- An adjustable DATA1000 DC amplifier from -26db to +26db gain by 6db or 8db steps with a 0-22Mhz 3db bandwidth.
- A Krohn-Hite 3202R band-pass filter whose low-pass and high-pass frequencies are adjustable from 10Hz to 2Mhz with a 120db/decade roll-off slope either with a max-flat or RC filtering setting.
- An oscilloscope DATA6000 12 bits resolution and 10Mhz maximum sampling rate. Averaging speed is limited to around 20 Hz (depending on the configuration), which can be small in some cases.
- A signal generator HP3314 which triggers the pulser and the oscilloscope and fixes the pulse rate.
- A PC computer controls the oscilloscope, the data acquisition and the transducer motions via a GPIB interface. It stores the data and plots them on a HP7550 plotter. This last feature allows a preliminary display of the recorded wavefield for changing of acquisition parameters, if necessary.

This acquisition system allows for faithful recording of low-level (on the order of $2\mu\text{V}$ pp) ultrasonic signals with 72db dynamic range and a 40Khz-2Mhz 3db bandwidth.

2.4 Transducers

This section deals with essential features of ultrasonic transducers regarding adequate scaling and wavelet quality. Those topics are discussed for piezoelectric transducers, although they can also be applied to other types of ultrasonic transducers. Once transducers properties are understood, a choice is made and the best available transducer is described.

2.4.1 General comments

The "diameter" of a seismic volume source (e.g air-gun) is of the order of 1m and that of the hydrophone about 5cm. When correctly scaled (by about a factor of 1000), the ultrasonic transmitter and receiver diameters would be 1mm and $50\mu\text{m}$, respectively. None of the ultrasonic wave generation devices are able to meet these size requirements. For piezoelectric transducers, a basic computation is done (appendix B) to link the minimum source transmitting power and the minimum receiving sensitivity to fulfill the desired signal-to-noise ratio. The frequency response, the directivity pattern, and the scattering target strength of the transducer are the other essential parameters.

2.4.2 Frequency response

It is clearly dependent of the principle to generate or record ultrasonic waves. In order to understand the frequency characteristics of piezoelectric transducers, it is necessary to review briefly the piezoelectric effect (appendix A), vibration modes and transducer construction.

Vibration modes

The type of wave (shear or compressional, S or P transducer) depends on the piezoelectric properties of the ceramic, the polarization direction, and the natural mechan-

ical modes of vibration. All these modes contribute to the mechanical response of an applied voltage, heaviside-like function and consist of the ultrasonic impulse response of the ceramic itself with free boundary conditions. In reality, the boundary conditions are determined by the mechanical impedance contrast between the ceramic and environmental materials. Assigning these impedance contrasts determine the mode of vibration, usually the first one of the type chosen and the damping. Indeed, extensive theoretical computations are performed by transducer designers to make one single mode dominant and to increase the damping coefficient in order to create a broad-band frequency response.

All the piezoelectrically-generated ultrasonic wavelets are not minimum phase. This fact might involve relaxation processes, but I have not analyzed it in any details.

Four ceramic piezoelectric types are usually built :

Thin disk : The thickness is much smaller than the diameter. If compressional or shear modes occur along the disk axis z , then high frequency P or S waves are generated and recorded. If flexural modes is chosen, low frequency P waves result (e.g bimorph disk).

Thick disk : The thickness is of the same order as the diameter. Compressional and shear modes along z , as well as radial modes, can occur. Focusing the design on one broad-band natural frequency is harder but has the advantage of generating intermediate frequencies for the same diameter as a thin disk.

Cylinder : Radial modes mainly occur and give relatively low frequency P waves.

Sphere : Radial modes occur and give relatively low frequency P waves.

Backing

Assigning adequate boundary conditions for the disk geometry is quite easy since the vibration occurs only along one axis. The technique of backing consists of choosing a high absorbing material whose acoustic impedance is close to that of the ceramic.

Using the classic mechanical analogy, backing is a way of adding a dash-pot (the backing material) to a spring (the ceramic). Backing materials are usually made of a high density metal powder and epoxy composites, and the high absorption is due to the "heavy" particles of metal scatterers. Adequate proportioning gives the best results. The backing material may also be the same unpoled piezoelectric material, provided that it has a low Q.

For cylindrical or spherical vibration, the backing idea is not easy to implement and nothing is usually done. The resolution quality of the signature depends mainly on the value of Q for the piezoelectric material.

Design

Figure 2-2 sketches two design types of transducer capable of water immersion:

- A thin disk ceramic transducer, commonly called an immersion transducer, is mainly composed of a thick backing layer, ceramic, and a matching layer in contact with the medium (water), whose thickness is optimized to one-quarter medium wavelength.
- A spherical ceramic transducer, commonly called a hydrophone, whose contact with the medium is realized by a rubber enclosure whose acoustic impedance is equivalent to that of water.

Pulse shapes

Centered around their chosen natural mode, ceramic disk-type transducers have a broad-band response, and the smaller the ratio of thickness-to-diameter, the better the response. Cylindrical and spherical ceramic types have a narrow band response. The response of the two transducers described above are compared in figure 2-3. The signal and the amplitude spectrum of an immersion transducer (Panametrics V301 with a natural frequency of 500Khz) are more broad-band than those of a hydrophone

(ITC 1089 with a natural frequency of 350Khz). In both cases, the transmitter and the receiver are of the same type and the recording is done in the far-field on the main axis of the directivity pattern.

2.4.3 Directivity pattern

Two zones, commonly called far-field (Fraunhofer diffraction) and near-field (Fresnel diffraction), come out from directivity pattern analysis. When considering the contribution of all the elementary diffracting point sources or receivers of the transducer, the far field analysis takes only the first order difference in path in the phase term and assumes equal amplitude. In water for example, a transducer of volume V gives a pressure wave at a distance r_0 from its center equal to:

$$p = \int_V \frac{A}{r} \exp(ikr) = \int_V \frac{A}{r_0} \exp(ik(r_0 + \delta r)) \quad (2.1)$$

On the other hand, the near-field incorporates high-order terms in the phase and eventually in the amplitude and the appropriate order to be included depends on the distance to the point considered.

It is easier to understand directivity as a radiation pattern. However, the far-field wave can be assimilated as a plane wave, and the reciprocity theorem suggests that the directivity pattern is the same for both receiver and transmitter. On the other hand, near-field features are more specific to the wave emission.

We are interested in the far-field features as seismic signals are usually recorded in the far-field. However, the experimentalist should know the near-field size or transition zone to avoid any surprises in his experiment.

The directivity pattern of three types of transducers are discussed:

Thin and thick disk : They act in a piston-like fashion and the far-field wavefield is evaluated by the contribution of all infinitesimal source points of the disk.

The resulting well-known theoretical directivity pattern is a first-order Bessel

function of the wavenumber k and the radius of the disk a (see e.g Hueter, 1955):

$$D(\theta) = 2 \frac{J_1(ka \sin \theta)}{ka \sin \theta} \quad (2.2)$$

This function is plotted at two frequencies in figure 2-4 for the immersion transducer Panametrics V301 (500 Khz natural frequency and 1" diameter) and indicates the directivity feature and the strong frequency dependence. These results were tested experimentally (figure 2-5). The side lobes were not resolved in the experimental curve because we used a pair of V301 as source and as receiver.

The near-field/far-field transition is given by

$$Y_0^+ = \frac{1}{4} \frac{d^2}{\lambda} \left[1 - \left(\frac{\lambda}{d} \right)^2 \right] \approx \frac{1}{4} \frac{d^2}{\lambda} \quad (2.3)$$

where $\lambda = \frac{2\pi}{k}$ is the wavelength and d the diameter of the disk.

For the V301 transducer, this transition is about 0.5" at 125Khz and 2" at 500Khz.

Cylinder : It consists of four lobes (hydrophone B&K 8103 in figure 2-6) whose angle nodes depend on the length-to-diameter ratio of the cylinder and whose values on the wavelength-to-diameter ratio.

Sphere : It is theoretically omnidirectional, although transducer design induces a frequency-dependent node at the cable output (hydrophone ITC 1089 of figure 2-7)

2.4.4 Transducer applications

Thin disk immersion transducers provide a high frequency, high resolution wavelet and directivity. They are extensively used in non-destructive testing as transmitters and receivers because of those features. Omnidirectional hydrophones are mainly used as receivers in underwater acoustic applications.

2.4.5 Backscattering

In laboratory studies where wavelengths are comparable to ultrasonic transducer dimensions, scattering from the transducer need to be considered. The backscattering effect is illustrated in figure 2-8 for a source, and a similar phenomenon occurs for a receiver. For example, figure 2-9 shows the multiple reflections from a face-to-face V301 transmitter V301 receiver configuration. The backscattered energy depends on the size, shape, and acoustic impedance of the scatterer, the angle of incidence and the frequency of the incoming wave. A large number of cases can be found in the seismic acquisition scheme, and we will not develop any rule or formulae. We can simply say that the effect can be significant when the source or the receiver is a large disk type immersion transducer and the rays are nearly perpendicular to transducer surface. In the case of hydrophones, the scattering effect is omnidirectional but it is weak because of the shape and that the acoustic impedance of the rubber around the transducer is close to the water impedance.

2.4.6 Choice of transducers

The choice of transducers depends on the type of ultrasonic experiment. In classical marine seismic acquisition modeling, a reasonable size and directivity pattern have to be evaluated, taking into account the acoustic power requirement and the frequency response of the source. A small size, omnidirectional hydrophone is desirable as the receiver. We find that a tiny hydrophone fulfills the sensitivity requirement (appendix B). The small piezoelectric receiver operates below its resonant frequency and therefore the receiving frequency response in a subresonant mode is quite good.

2.4.7 Transmitter

The transmitter used in these experiments is a thin disk type immersion transducer (Panametrics V323) built from a ceramic disk of 1/4" diameter. We use a frequency

range 0-400 Khz. In spite of its high natural frequency (2.25Mhz), its transmitting power at 250Khz has been evaluated to be about 115db re $1\mu\text{Pa}/\text{V}$, i.e., slightly under the threshold computed in appendix B. It has a broad-band signature and when used in the subresonant mode, its signature (figure 2-11), evaluated by the receiver hydrophone, is quite good (the slight ringing is produced by the receiver).

The theoretical directivity pattern is plotted in figure 2-10 for a frequency of 250 Khz, which is the medium frequency in our experiment. The figure shows that amplitudes do not vary by more than a factor of 2 between 0 and 45 degrees.

At 250 Khz, the near-field/far-field transition zone is equal to 1.7 mm, and its small size prevents any strong backscattering energy. Because this transducer is backed, it radiates in one single half-space, and the ghost reflection is not produced when the transmitter is set at the surface.

2.4.8 Receiver

The receiver used is a tiny hydrophone manufactured by S.E.A whose active element is a 0.4mm diameter PZT44 ceramic. Its sensitivity has been evaluated to be about -240db re $1\text{V}/\mu\text{Pa}$, making it sensitive enough to keep the equivalent electronic noise of its matching preamplifier below the natural ultrasonic noise (appendix B). Its directivity pattern is quite omnidirectional and its tiny size makes any backscattering and near-field effects negligible from the ceramic itself. This last feature is quite important when using it as an O.B.H very close to the water bottom, as it could be set within 1mm. However some backscattering energy can show up from the 1" long conical shape of the hydrophone body. Its frequency response has been evaluated to be quite flat with a slow slope in the low frequency range. However, low-level scattering energy coming from the close environment of the ceramic remains a shortcoming (figure 2-11) but it is not critical in our experiments because of its level.

2.4.9 Signal to noise optimization

It was found that the natural ultrasonic noise in the water tank is nearly white, with an increase in the low frequency range and at some particular frequencies, which may be caused by internal resonance of the tank and the bridges (appendix B). Although this is a weak contribution, this last coherent noise may be annoying because it does not weaken easily when stacking. The global ultrasonic noise in the tank is high, compared to the level we could have expected. For example, it is about 50 db greater than the molecular agitation level at 1 Mhz (which dominates at that frequency in the ocean). The coating of an absorbing material (like wax whose $Q \simeq 1$) may reduce the noise in the tank.

In appendix B, the receiving sensitivity computation shows that the SEA hydrophone with -240db re $1V/\mu Pa$ fulfills the requirement. Taking advantage of the 72db dynamic range of the oscilloscope, we can rely on two parameters : transmitting power of the source and averaging. Keeping the advantages of the source mentioned above leads to optimize the averaging value. Hence, when we want high quality data and see weak signals, 1000 stacking may be necessary, but in most acquisition schemes, such a 72db signal-to-noise ratio is not required, and more practical values (32-128) are adequate for averaging.

2.5 Models

3D models have to represent what is to be modeled with materials whose acoustic properties are close to the real rocks. It is desirable that the welded contact assumption be fulfilled for layered models, and the effect of the bonding agent layer (as pointed out by Toksöz (1964) and Schwab (1968) for 2D layers) be evaluated. On the other hand, a simple assembly of individual materials is a more flexible solution (the water acts as the coupling agent), which may, in some cases, be sufficient when the transmission of shear waves has no interest and when the reflection of P and S waves

are similar to the welded-layer model.

2.5.1 Modeling materials

A table of acoustic properties of the suitable and easily available materials is provided in appendix E. They can be classified according to:

Metals : Their high velocities make them ideal for simulating rock basement.

Aluminum is the most appropriate, because it is close to high velocity rock such as granite, dolomite or limestone and has density (2.7 g/cc) similar to those rocks. Lead may be interesting to simulate a semi-infinite medium because of its low acoustic velocities, its high density and its low hardness (for shaping purposes).

Plastics : Their P velocity of the order of 2500m/s and density around 1.5 make them close to those of some rocks such as shale or highly porous sandstones. They can be machined easily within 0.1 to 1 milles flatness and polished up to number 16.

Epoxies : Their acoustics properties fall in a narrow range. They are useful as bonding agents provided that their viscosity is low (typically 100 cps) and that their curing time at room temperature is long. They can be also used for making layers.

Composites : They have a larger range of acoustical properties. Specifically, materials such as aluminum and other powdered metals and ceramics can be cast into an adhesive to develop the composite. By varying the relative amounts of adhesive (resin) and additives, it is possible to control the properties of the model. Furthermore, the adhesive composite can be cast. The distribution of dense inclusions in an epoxy matrix influences not only the density and seismic waves velocities, but also the attenuation. The particles act as scatterers in the composite. The larger the particle size, the greater the attenuation.

Rubber : Neoprene and polyurethane have good acoustic properties to model sediments. The values of Q are around 50. They can be machined to produce a smooth surface (within the 0.5mm range). Other rubbers, like silicone rubber are only suitable in specific applications due to their low P velocity (of the order of 1000m/s).

2.5.2 Multi-layer models

Epoxies and composites described above are quite suitable for making multi-layer models. However, a major inconvenience when preparing epoxies and composites is the formation of small air bubbles, which develop during the mixing of the compound. Indeed, a small amount of air bubbles in the material decreases velocities significantly. To avoid this problem, low-viscosity epoxies, a care in the mixing and curing processes and the use of a vacuum pump are recommended. Because of the difference in thermal expansion coefficient between the material to be assembled, it is also recommended to choose epoxies which slowly cure at room temperature. Gravitational separation provides the potential for developing two layers in a low-viscosity epoxy powdered-metal compound. The metal particles homogeneously settle at the bottom developing an interface between the composite material and the epoxy. Except for the edges of the model, where surface tension acts due to the mold, the interface is relatively plane and smooth. Gravitational effect can be also used when making layers with composites materials already prepared. If these materials do not have too low a viscosity, the composites, which have a different density, cure and do not mix together, forming a natural welded interface.

For example, a typical four-layer model can be made using:

- 1) Aluminum to represent the basement
- 2) A thin epoxy bonding layer (e.g EPO-TEK)
- 3) A high density composite material

- 4) A low density composite material that will bond with the previous layer during the curing process
- 5) A thin epoxy bonding layer
- 6) A neoprene block.

The shape of the modeling block (multi-layer or single-layer) can be studied to take advantage of the spreading of the rays and limit the edge effects. Tatham *et al* (1983) provide an excellent example of such model formation.

2.6 Scale factor

To scale sampling intervals from the model tank to field data acquisition, practical factors are multiples of 6000. In our water tank, the stepping motor increments are given in fraction of inches. In field systems, the hydrophone or geophone separations are given in feet. For a scale factor of 6000, the resolution is then 1.25 ft in x, y and 0.5 ft in z in field recording. For example, one can choose 25 or 50 ft for the spatial sampling.

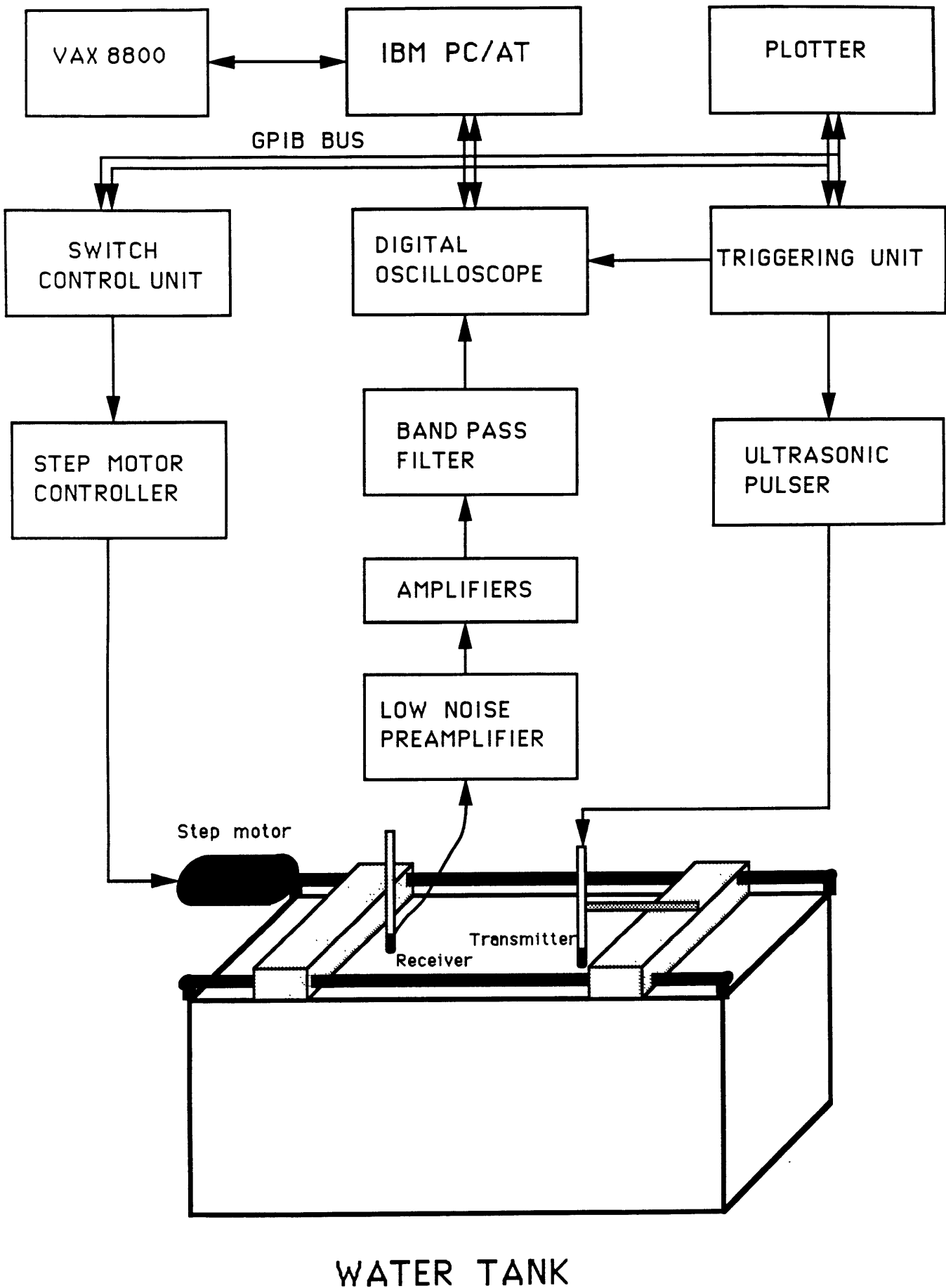
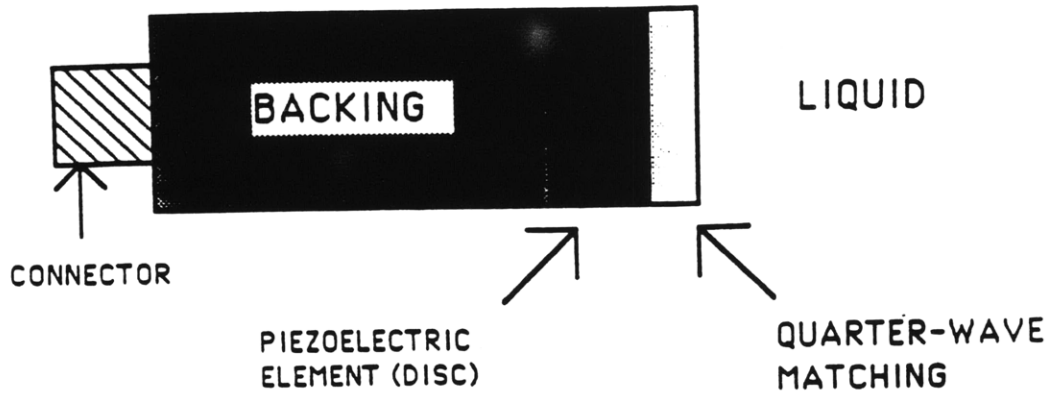


Figure 2-1: 3D water-tank ultrasonic facility block diagram.

IMMERSION TRANSDUCERS



HYDROPHONE

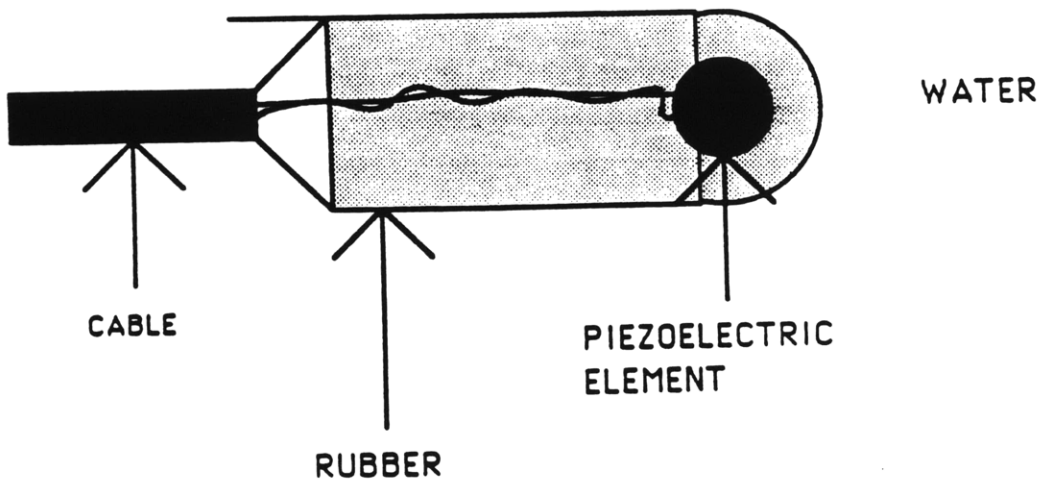
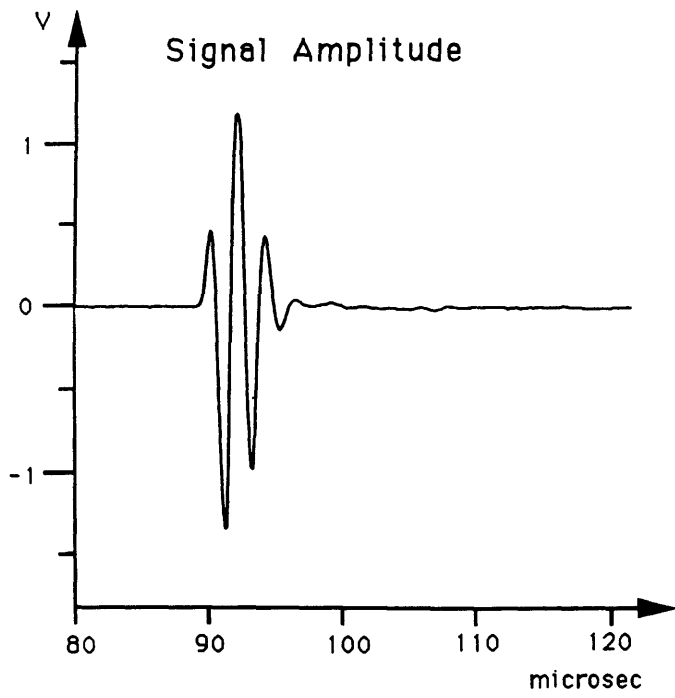
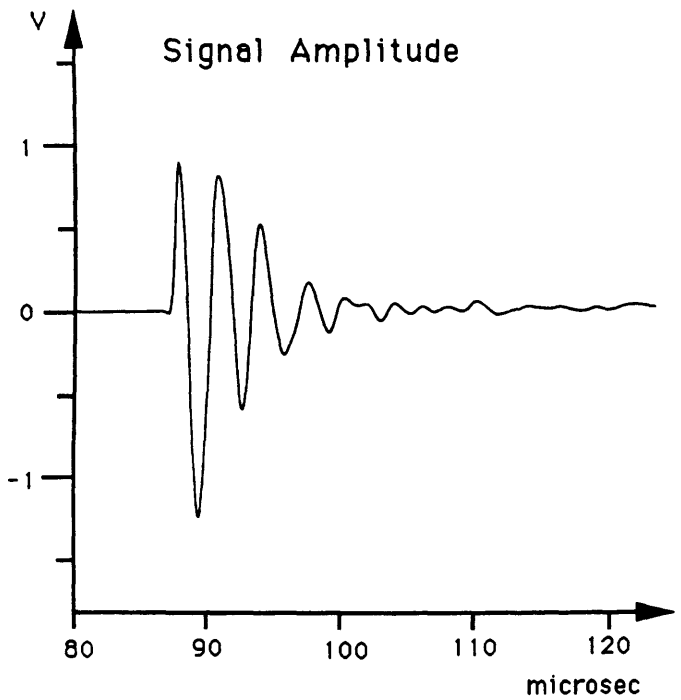
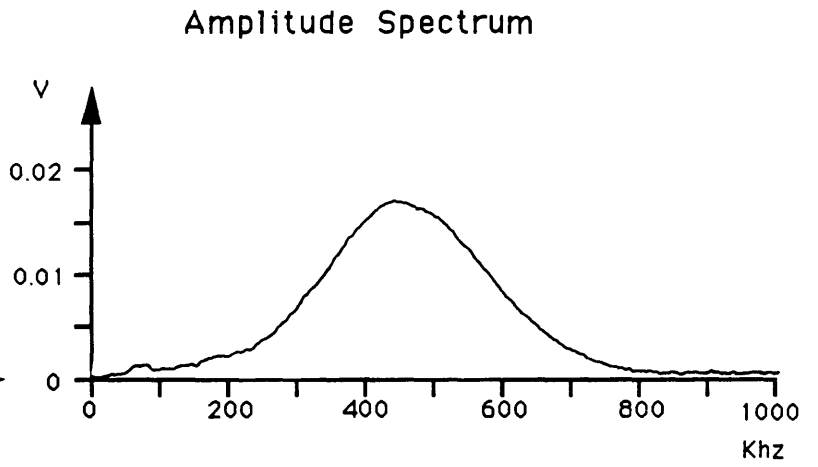


Figure 2-2: Sketch of an immersion transducer and of an hydrophone design.



Panametrics V301



ITC 1089

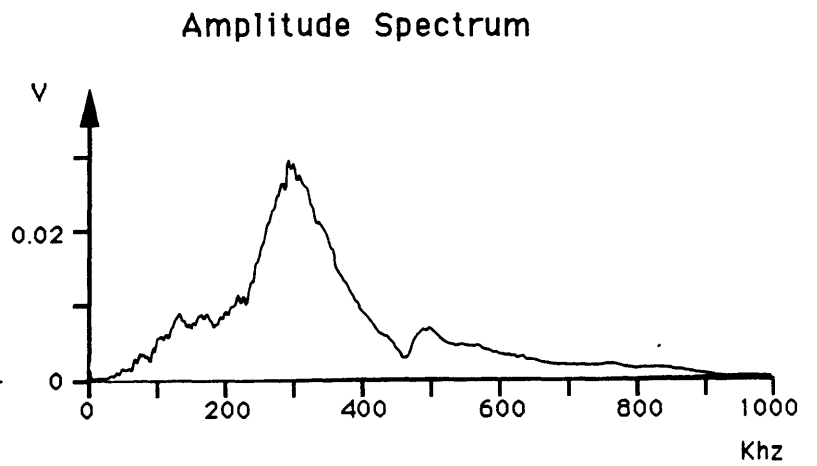


Figure 2-3: Signal and amplitude spectrum comparison between the immersion transducer Panametrics V301 and the hydrophone ITC 1089.

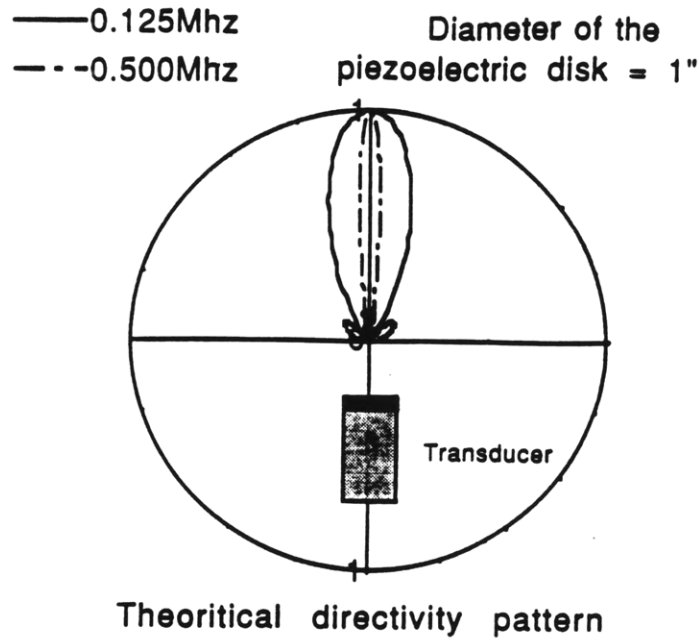


Figure 2-4: Theoretical vertical directivity pattern of the immersion transducer Panametrics V301 at frequencies 500Khz and 125Khz. Each curve is normalized.

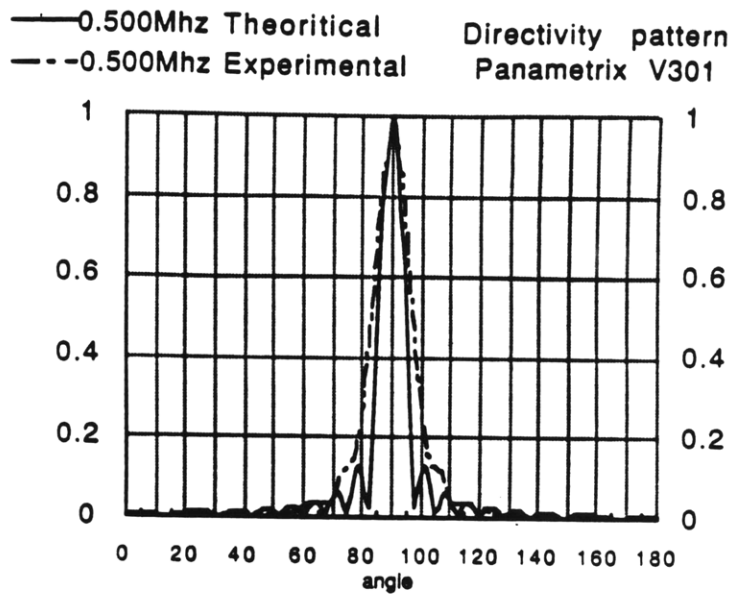


Figure 2-5: Comparison between the experimental and the theoretical vertical directivity pattern for the Panametrics V301 at 500 KHz.

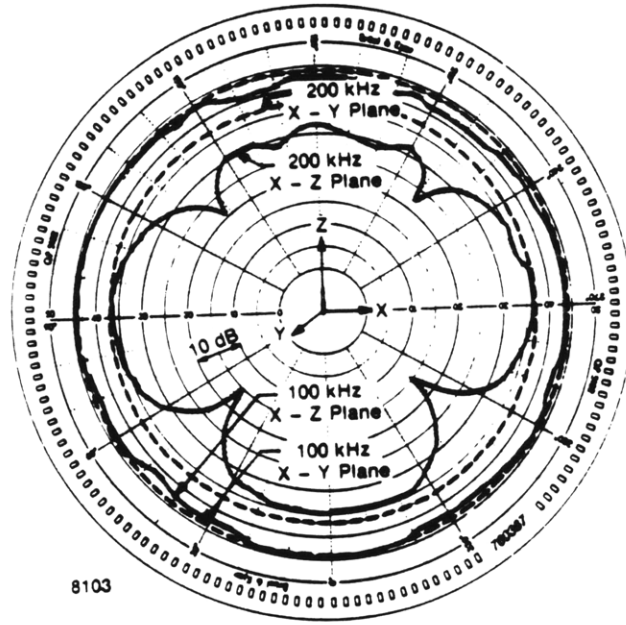


Figure 2-6: Vertical directivity pattern of the cylindrical ceramic type hydrophone B&K 8103.

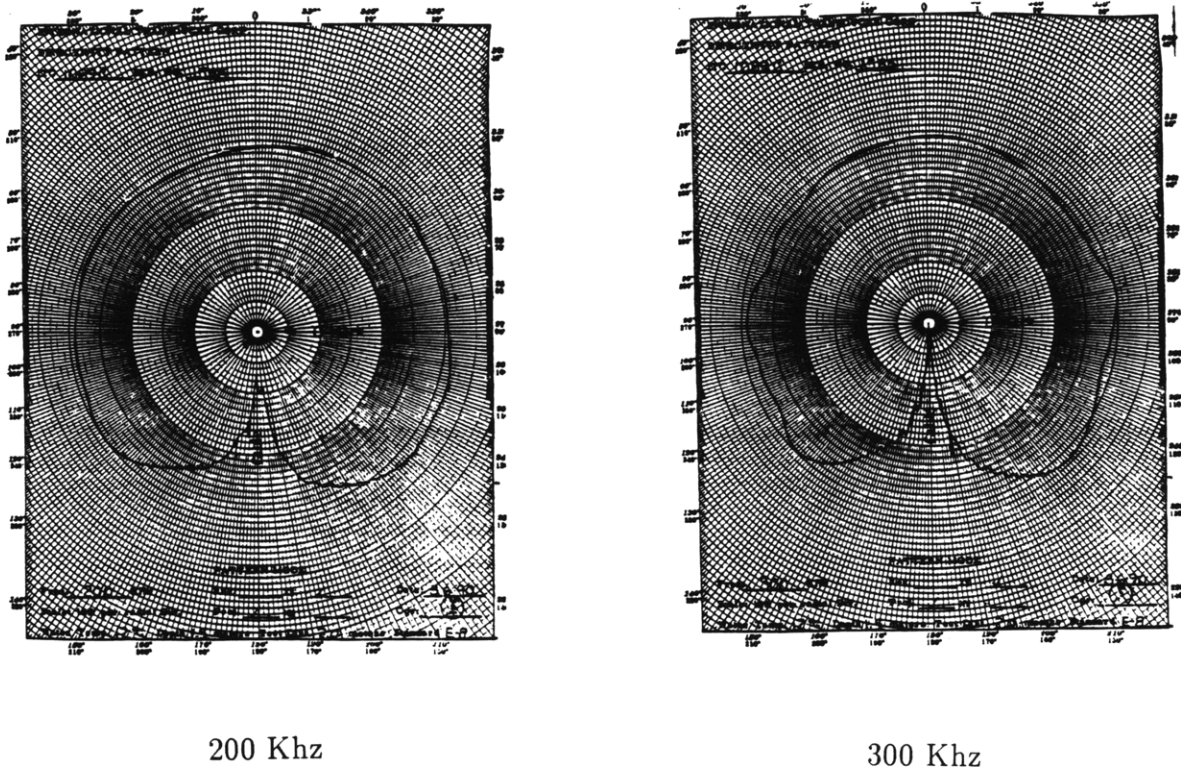


Figure 2-7: Vertical directivity pattern of the spherical ceramic type hydrophone ITC 1089

Backscattering effect

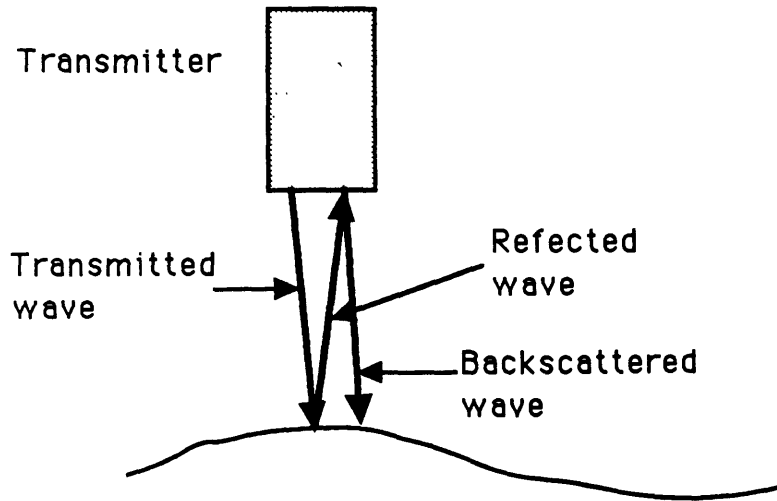


Figure 2-8: Backscattering effect.

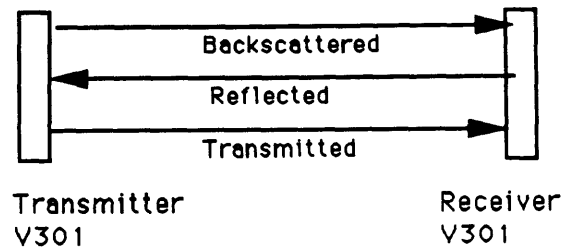
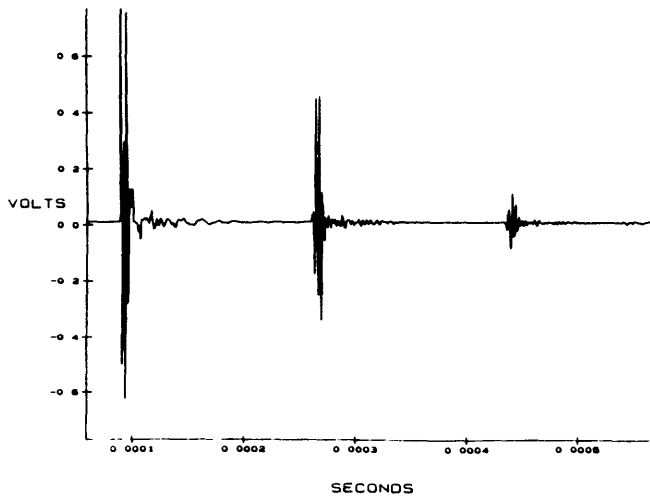


Figure 2-9: Illustration of the backscattering effect.

Immersion Transducer V323
Theoretical radiation pattern

Diameter 1/4 in - Frequency 250 KHz

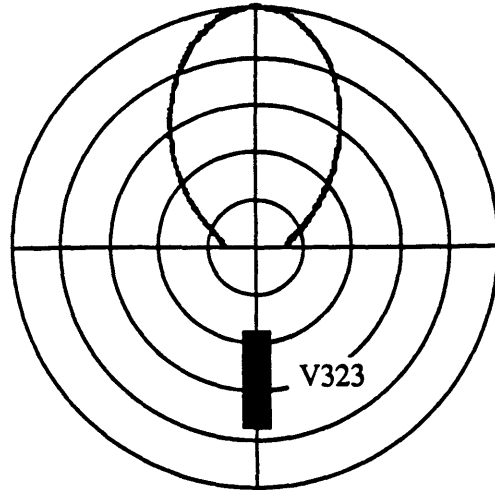


Figure 2-10: Theoretical directivity pattern of the V323 transmitter at the middle value 250KHz of the frequency range of interest.

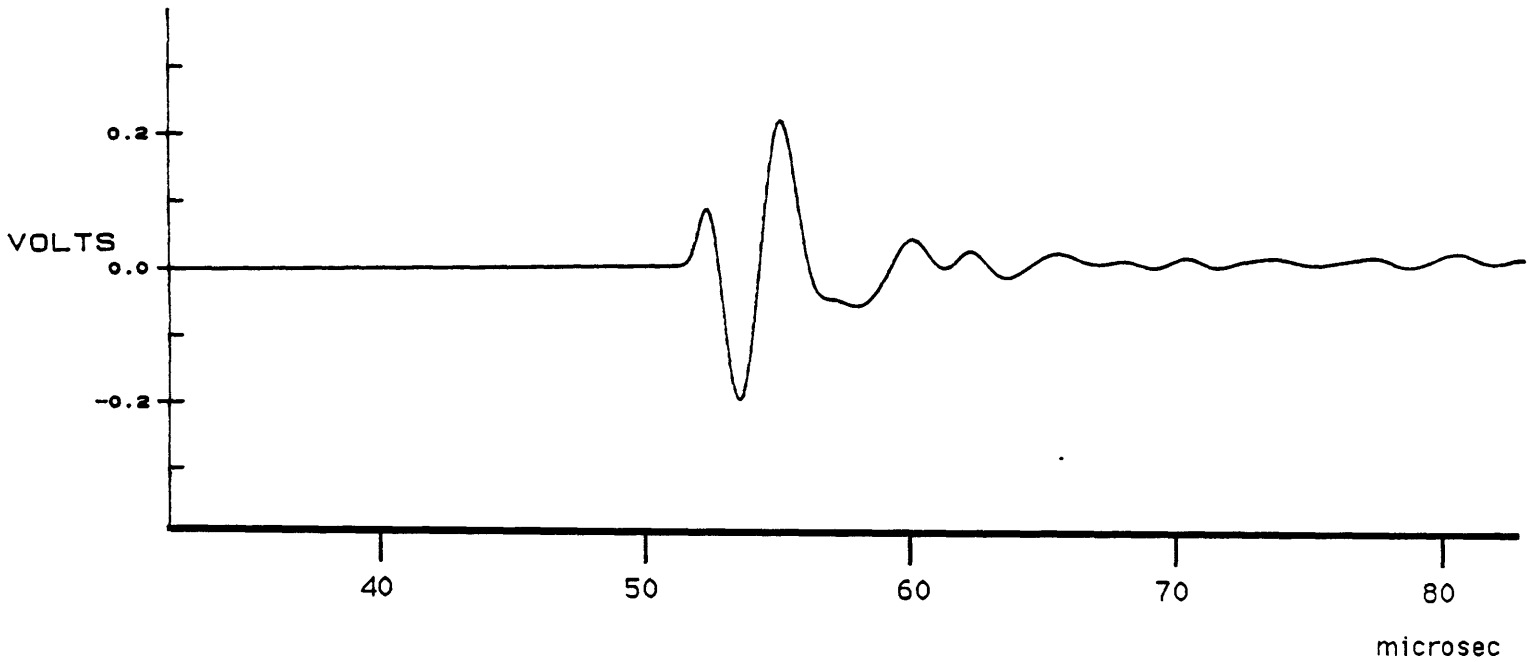


Figure 2-11: Wavelet from the transmitter Panametrics V323 recorded with the receiver hydrophone SEA with a 50KHz low-pass filter and a 400KHz high pass filter. The receiver is in the transmitter axis at 2". These are the experimental parameters.

Chapter 3

Dip interface imaging of a two-layer model

3.1 Introduction

This ultrasonic model is designed to test the concept of using receiver multiples explained in chapter 1 along with the primary reflections to image a dipping interface. Such a test with complete wavefield ultrasonic data provide a more realistic evaluation of the method than the ray-based synthetic seismograms generated on comparison purpose.

3.2 Description of the set-up

The modeling set-up is shown in figure 3-1. This shows source and receiver geometries and the model in the tank. The solid model consists of an aluminum block with a 70 shore neoprene layer. The aluminum-neoprene interface has a dip of 10 degrees. The machining of the neoprene was good enough to match the perfectly flat aluminum surface within 0.2mm. No bonding agent has been used but water acts as the coupling agent between the aluminum and the neoprene. Because the P velocity of neoprene

(1600 m/s) and the water velocity (found to be here 1520 m/s) are close, the main difference, relative to a perfect bonding may be the transmission of shear waves into the aluminum and the polarity of the converted waves inside the neoprene. In such a case, these differences do not affect our purpose, since we are mainly interested in P reflections. The S.E.A hydrophone was less than 1mm from the water bottom. All dimensions given in the model have a 1% to 2% tolerance.

The synthetic model is shown in figure 3-2. P-wave velocities are estimated with 1% accuracy and S-wave velocities with 3% accuracy. Q estimates are correct within a factor of two (Selfridge, 1985). We did not measure the attenuation independently. The scale factor of 20000 (figure 3-3) is chosen to convert physical dimensions from water tank model to real deep-water case. According to this, scaled frequencies are in the low range of the usual seismic band. It is obvious that decreasing the scaling factor (e.g four times) scales the frequencies in the usual seismic band and put the water depth at 400 meters.

The fact that the real model was 10 degrees inclined for the modeling convenience (figure 3-1), and that the synthetics were calculated according to the model shown in figure 3-2, does not deteriorate the comparison between the ultrasonic and the synthetic seismograms, since the waves of interest are far from the edges and the directivity pattern of the source makes the edge reflections small.

The modulus and the phase of the complex reflection coefficients are plotted in figure 3-4 and 3-5 for the two interfaces. They are real for precritical reflection and transmission $P_1 - P_2$ and indicate the true relative displacement for all the body waves. Beyond the first critical angle, their complex values incorporate evanescent waves and do not help in the seismogram analysis. The phase is defined at π , which means that a phase shift of $+\pi$ at the critical angle does not appear explicitly in the phase curve.

The reflection and transmission coefficients show the following results:

- For the water-neoprene interface, the reflection coefficient R at normal incidence

is 0.156 and decreases slightly with an increase in angle. At 40 degrees, it goes through a zero and after that, becomes negative. The critical angle of 70 degrees is too large enough to appear in our synthetic seismograms which are calculated for a limited source-receiver separation. Notice that 40 degrees is the angle where transmitted P and S waves have the same transmission coefficients. In particular, the transmitted shear waves become of interest beyond 15 degree.

- For the neoprene-aluminum interface, the reflection coefficient R at normal incidence is 0.78 and the critical angle is about 15 degrees.

3.3 Raw data

3.3.1 Ultrasonic data

The transducers chosen for modeling were described in the previous chapter. The main parameters are indicated in figure 3-6 and some comments are given below:

- The gain to get 1.4V pp full scale is about 90db (77db + Y scale amplification=4). This corresponds to an output SEA hydrophone voltage of about $50\mu\text{V}$ full scale, i.e., about 60 times the value of the noise. To obtain this, averaging is necessary and we used a 1024-fold stack to get high quality data. According to a \sqrt{N} law, the signal-to-noise ratio full scale becomes 1920, i.e., 66db, which is close to the 72db dynamic range of the oscilloscope. Hence, we can affirm that the time section is nearly noise free. The sensitivity of the SEA hydrophone is about -240db re $1\text{V}/\mu\text{Pa}$ and the $50\mu\text{V}$ represents about 50Pa full scale pressure. The time required to record 72 source positions with 1024-fold averaging is 4 hours with 1 hour dedicated to the real-time HP plot (figure 3-7). This may appear long but it is due to the limitation of the DATA 6000 oscilloscope (cf chapter 2), the optional HP plot, and the exaggerated averaging requirement for this particular case.

- The 50 khz low cut-off frequency is intended to remove most of the low frequency noise, particularly the surface wave noise (appendix B).
- The spatial anti-aliasing condition is:

$$\Delta x \leq \frac{c}{2F_m(\sin\alpha_{max})} \quad (3.1)$$

where:

- Δx is the spatial sampling of 1/8".
- F_m is the high cut off frequency of 400Khz.
- α_{max} is the maximum take-off angle from the source.
- c the velocity of the water.

This condition is fulfilled for $\alpha_{max} \leq 37^\circ$. In that experiment, it is fulfilled for the primary and multiple rays, but not for the direct arrival.

The acquisition delay time of $96\mu s$ is scaled to $1.92s$. In the time section of figure 3-8 (a), for the first left-viewed offset, the primaries start at $T = 2.6$ sec and multiple reflections occurs at $T = 4.6$ sec. The section shows the reflected waves (hyperbola) and clearly show the head waves, after the critical angle. Note that at the critical angle, the $+\pi$ phase shifted post-critical reflection cancels the head wave. This destructive interference produces a well-resolved node. In the case of water-surface multiple, the head wave appears at a greater source offset, which illustrates the characteristic described in figure 1-5. The multiple reflection is the receiver multiple and the small source multiple is not obvious. It may be hidden by the waves closely following the receiver multiple, and this feature will be elucidated in the next section. The first water multiple, further labeled WWW at 3.2 sec, and the second at 5.2 sec, separate enough from the reflections to portray the deep-water case.

A number of waves traveling at the water velocity, mainly after the direct water arrival, are due to the diffraction model edge and the hydrophone body backscattering

of the receiver, and they are more energetic when we use the omnidirectional source ITC1089 (appendix G). The FK filtered data section of figure 3-9 (a) uses a fan filter rejection 0-1550m/s and a low-pass filter of the scaled high cut-off frequency of 20Hz, because the FK plot indicates that the direct arrival is aliased (The reflections are not aliased). That filtered section improves the picture without changing its main aspect. Hence, the unfiltered raw data have been migrated.

The first arrival has been used to determine the true water velocity of 1520 m/s and the accurate water depth of 1540 meters. Those values have been entered in the synthetic model. The water depth is particularly important for superposing primary and multiple images correctly because a depth inaccuracy produce only a shift in the primary depth section, whereas it produces a threefold shift in the multiple image.

Deconvolved data

In order to deal with a zero-phase wavelet, the ultrasonic data have been deconvolved according to the procedure explained in appendix F. In spite of the good resolving power of the ultrasonic wavelet, we obtain higher resolution with a suitable shorter deconvolved wavelet and the deconvolution operator-generated noise keeps a weak value. The high frequencies in figure 3-8 (b) of the deconvolved raw data section are due to deconvolution noise. The filtered section is shown in figure 3-9 (b).

3.3.2 Synthetic data

The synthetic rays, calculated using the model and parameters given in figure 3-2, are shown in figure 3-10. The rays corresponding to the three main waves involved in the imaging scheme are plotted, and clearly demonstrate the lateral extension of the receiver multiple image as previously mentioned in chapter 1. Their amplitudes are plotted on a partial synthetic section (figure 3-11), and show the dominance of the receiver multiple over the source multiple. The wavelet is a 10Hz zero-phase Gaussian envelope-modulated cosine function. The wave labels indicate the layers where they

have traveled, coming from the source first. W means water and N neoprene.

At the critical angle of the neoprene-aluminum interface, the $+\pi$ phase shift make a sharp change in the reflection hyperbola as compared to the ultrasonic data because the head waves are not generated by the synthetic program. A nearly complete synthetic section in figure 3-12 explain why the source multiple does not appear clearly, except for small offsets: It is overwhelmed by the receiver multiple converted wave. Indeed, the source multiple is also distinguishable at low offsets on the ultrasonic section of figures 3-8 (a) and 3-8 (b).

As previously explained in section 1.4.2, the synthetic seismograms feature a vertical component recording whose directivity pattern looks like the ultrasonic transmitter directivity pattern, and do not make further amplitude comparison out of interest. The amplitude comparison indicates a fairly good agreement, even if the wavelet characteristics are different. In particular, this means that the specific absorption value $1/Q$ was chosen adequately.

A synthetic model, featuring a very thin water layer between the neoprene and the aluminum, produce the section shown in figure 3-13. Comparison with the previous welded-contact model synthetic section indicates that the phase shift of the converted waves is the only significant difference. Despite the care in designing the synthetic model, one cannot distinguish clearly which one best compares with the ultrasonic section. The difficulty in matching them is due to the small uncertainties in the velocities, as well as the accuracy for measuring the true model dimensions.

A large difference occurs in the primary converted waves at large offset, but figure 3-14 clearly shows the limitation of the ray-based synthetic program for that O.B.H configuration: the converted-wave rays do not behave correctly near the receiver.

3.4 Images

The imaging zone in figure 3-15 was chosen according to the ray coverage. In order to image the neoprene-aluminum interface, the velocity model consists of the water layer and a semi-infinite neoprene layer.

3.4.1 Dip filter

The migration program features an optional dip filter. So far we know a range of dip for the reflectors to be imaged, this filter is intended to remove artifacts and smooths the impulse response of the Kirchhoff operator. In particular, the source multiple artifact in the receiver multiple imaging may be completely or partially removed. In the fan ray shot, the incident angle of the receiver and the source rays is calculated at a defined image point. The dip angle of the reflector is figured out and a cosine tapered function weights the contribution of the image point in the migration scheme. For example, a $+10 \pm 10$ degree filter means that a calculated dip angle of $+5$ degree has a weighting of $\cos(\pi/4)$. This filter will then select the reflectors between a 0 and 20 degree slope. It has been used to improve the images.

3.4.2 Ultrasonic data

The superposition of both coverage rays and dip reflector true position on the depth section (with a threefold vertical exaggeration through figures 3-16 to 3-18), shows perfect matching with the primary and receiver multiple images and the poor match with the source multiple image. The primary image is plotted with a positive polarity, whereas multiple images are plotted with an inverse polarity in order to account for the phase shift due to the water-surface reflection. The post-critical information results in a progressive wavelet phase shift along the reflector. The primary, the receiver multiple, and the total image are plotted without vertical exaggeration at the same amplitude scale:

- In figure 3-19 (a), the primary image is added to the receiver multiple image: One can distinguish a very tiny upward curvature in the total image at the distance of the post-critical primary information.
- In figure 3-20 (a), only the precritical information from the primary image is used and the total image features a flatter reflector.

Figure 3-19 (b) and figure 3-20 (b) show the images obtained by migrating the deconvolved time section of figure 3-8 (b).

3.4.3 Synthetic data

The imaging of the complete synthetic data section of figure 3-12 does not look as good in figure 3-21. The sharp phase shift at the critical angle, which was discussed above, similarly shows up on each individual image. Because that phase shift occurs at two different points of the reflectors on the primary and receiver multiple image, the addition does not give a good image of the reflector.

It is obvious that the interpretation of the images obtained by the migration of the ultrasonic data is much more valuable than those obtained with the ray-based synthetics seismograms.

Synthetic model 1

2D profile

Scale factor used : 20000

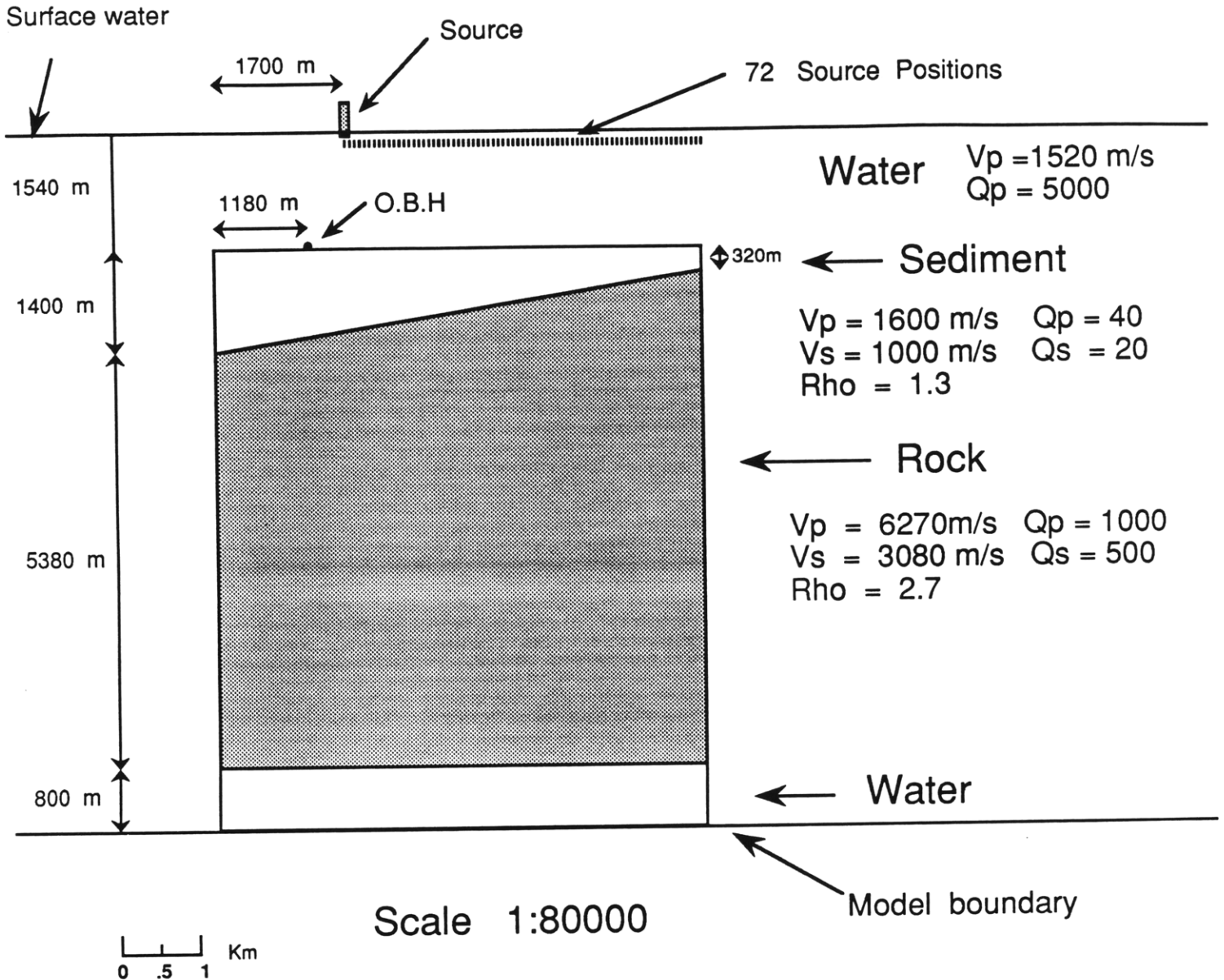


Figure 3-2: Synthetic model used to compute synthetic seismograms.

Model No 1

10 degree dip Neoprene-Aluminium interface

Parameters	Ultrasonic experiment	Marine acquisition
Dimension of the model	12*14*6 inches	6200*7600*3100 meters
Spatial sampling	1/8 inch	63.5 meters
Time sampling	400 nanosec	8 millisec
High cut-off frequency	400 Khz	20 Hz
Low cut-off frequency	50 Khz	2.5 Hz
Record length	200 microsec	4 sec

Scaling factor 20000

Figure 3-3: Scaled parameters.

Water - Neoprene Reflection Coefficients

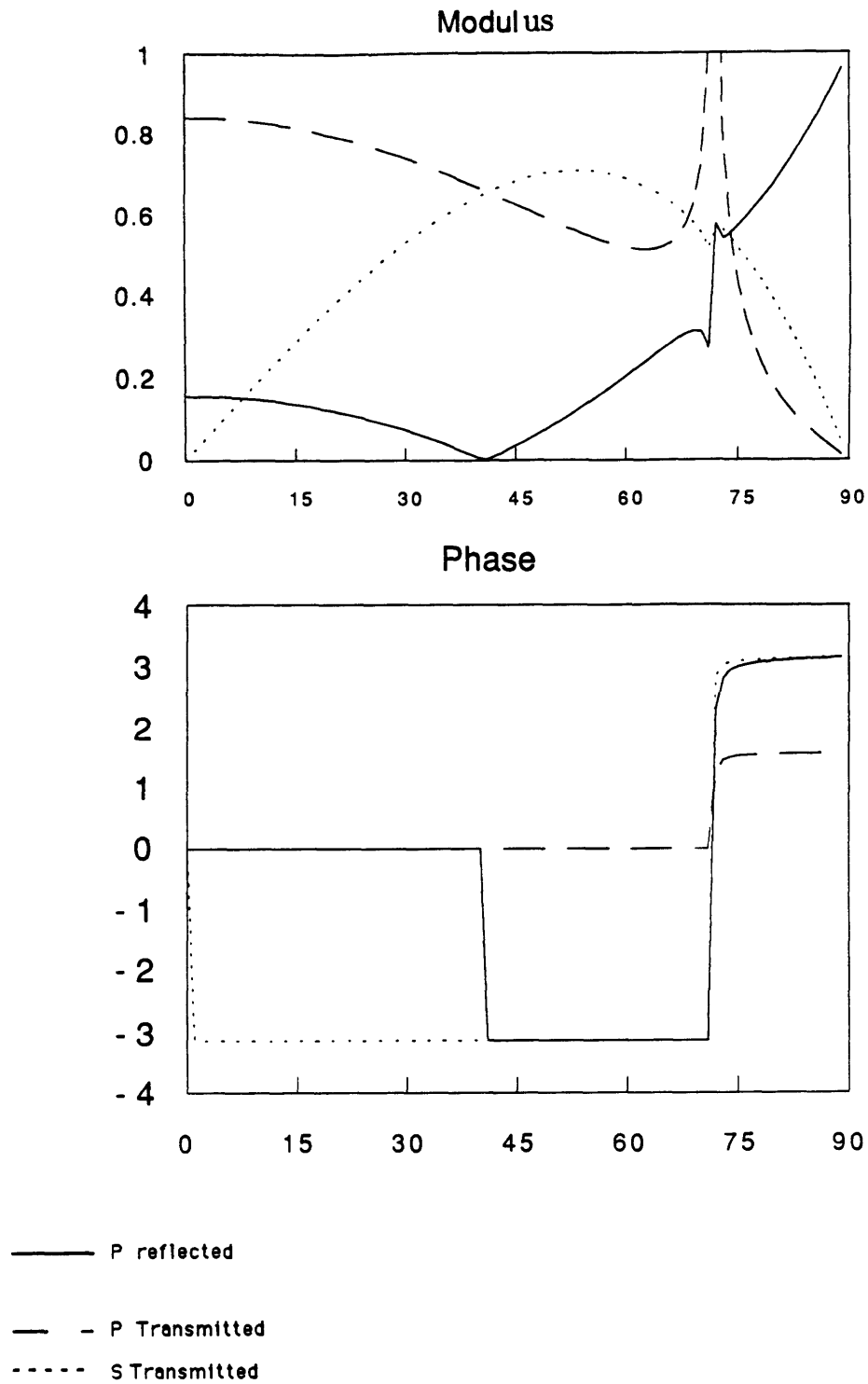


Figure 3-4: Modulus and phase of the Water-Neoprene complex value reflection and transmission coefficients versus angle.

Neoprene - Aluminium Reflection Coefficients

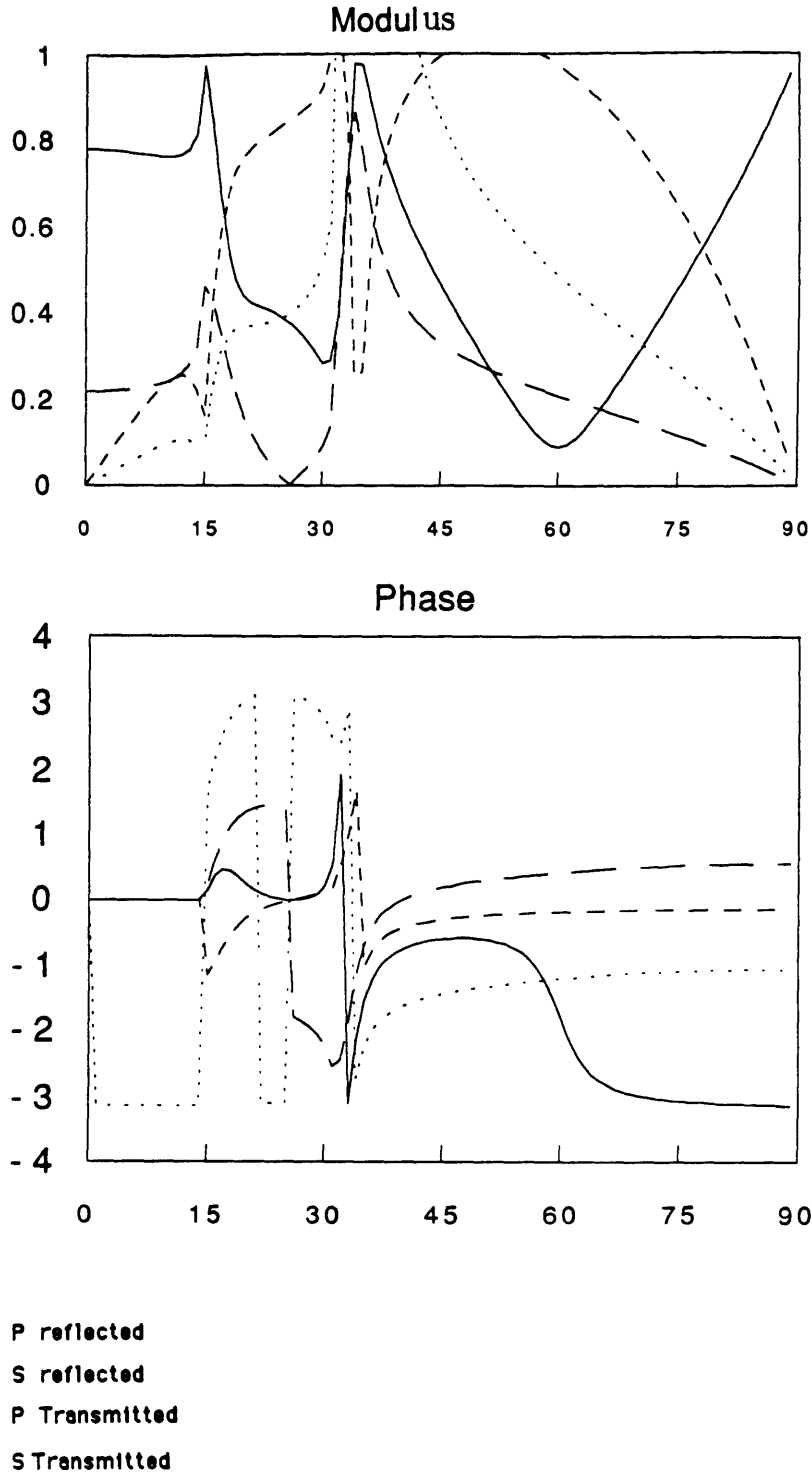


Figure 3-5: Modulus and phase of the Neoprene-Aluminium complex value reflection and transmission coefficients versus angle.

Neoprene-Aluminium Model No 1

3D model experiment No 1

- **Geometry :**

Source line : X

Source intertrace : 1/8"

Nb of source points : 72

Receiver line : O.B.H

Receiver intertrace :

Nb of receiver points : 1

- **Source parameters :**

Transmitter : Panamatrix V323

Pulser : Panamatrix 5052PR

Energy setting : 4

Damping setting : 2

- **Receiver parameters :**

Receiver transducer : Miniature Hydrophone SEA

Preamplifier(s) : SEA + Panamatrix 5660B

Total gain in db : 77 db

Bandpass filter : Krohn-Hite 3202R

Low cut-off frequency : 50 Khz + AC on acquisition

High cut-off frequency : 400 Khz - Max flat -

- **Acquisition parameters :**

Acquisition unit : Ampli D1000 + Oscillo D6000

Time sampling : 400 nanosec

Time delay : 96 microsec

Number of points acquired : 512

Resolution : 12 bits companded

Y full-scale : 1.4 Volts

Y scale amplification : 4

Averaging : 1024

Figure 3-6: Acquisition parameters.

HP7550 HARDCOPY ACQUISITION RAW DATA

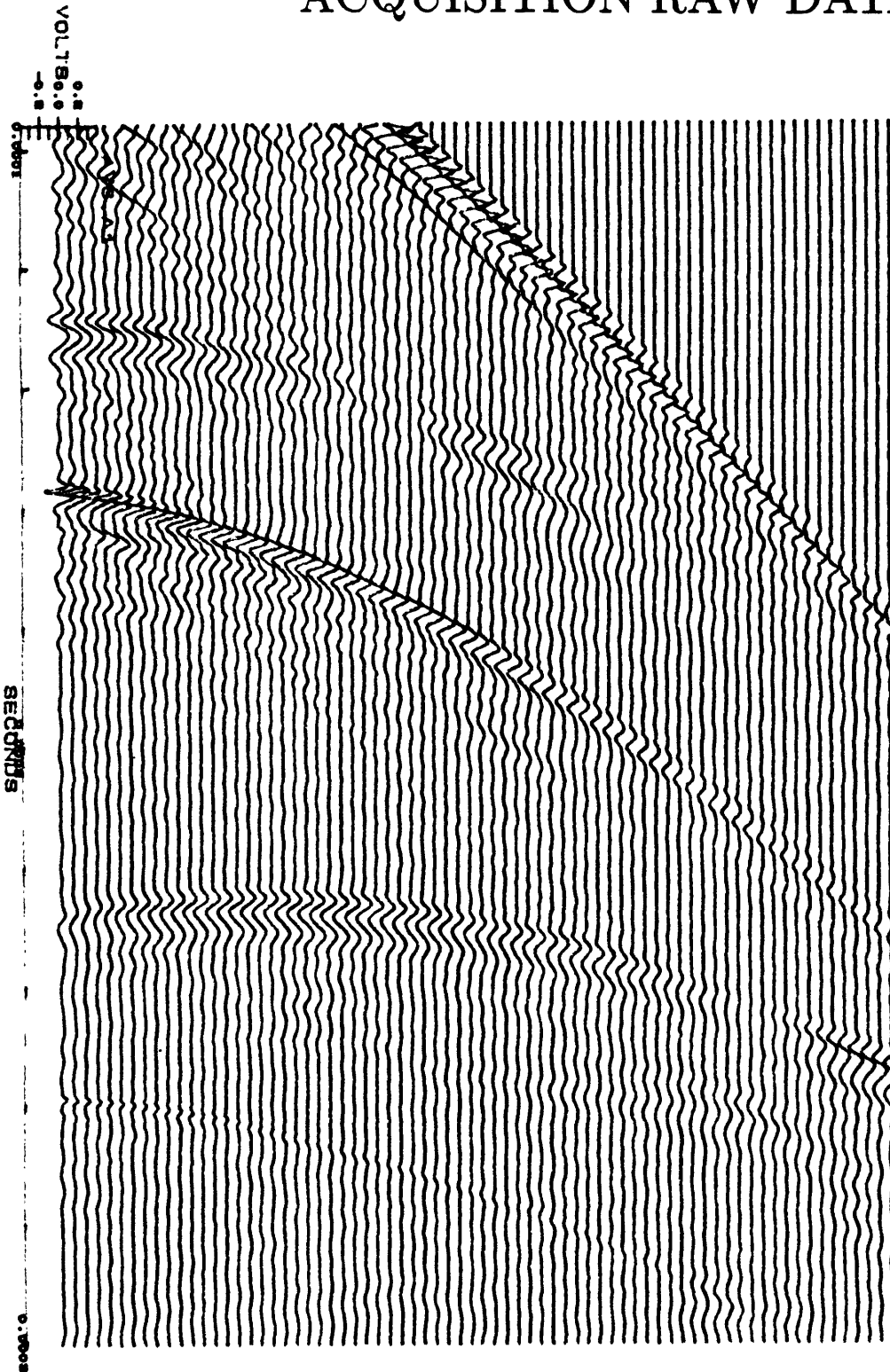
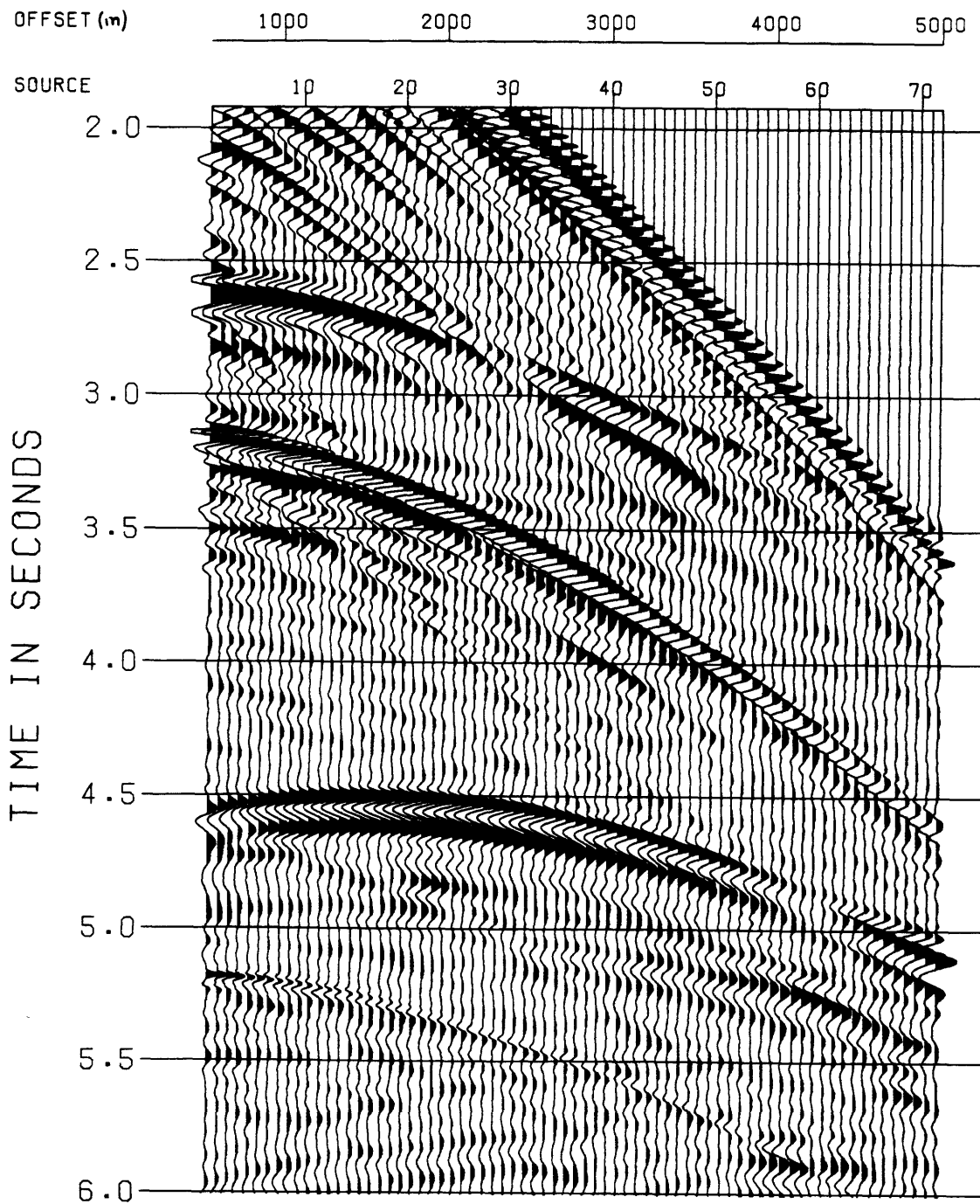


Figure 3-7: HP7550 "real time" plot.

RAW DATA TIME SECTION



Scale factor = 20.000

Figure 3-8: (a) Ultrasonic raw data time section.

DECONVOLVED RAW DATA TIME SECTION

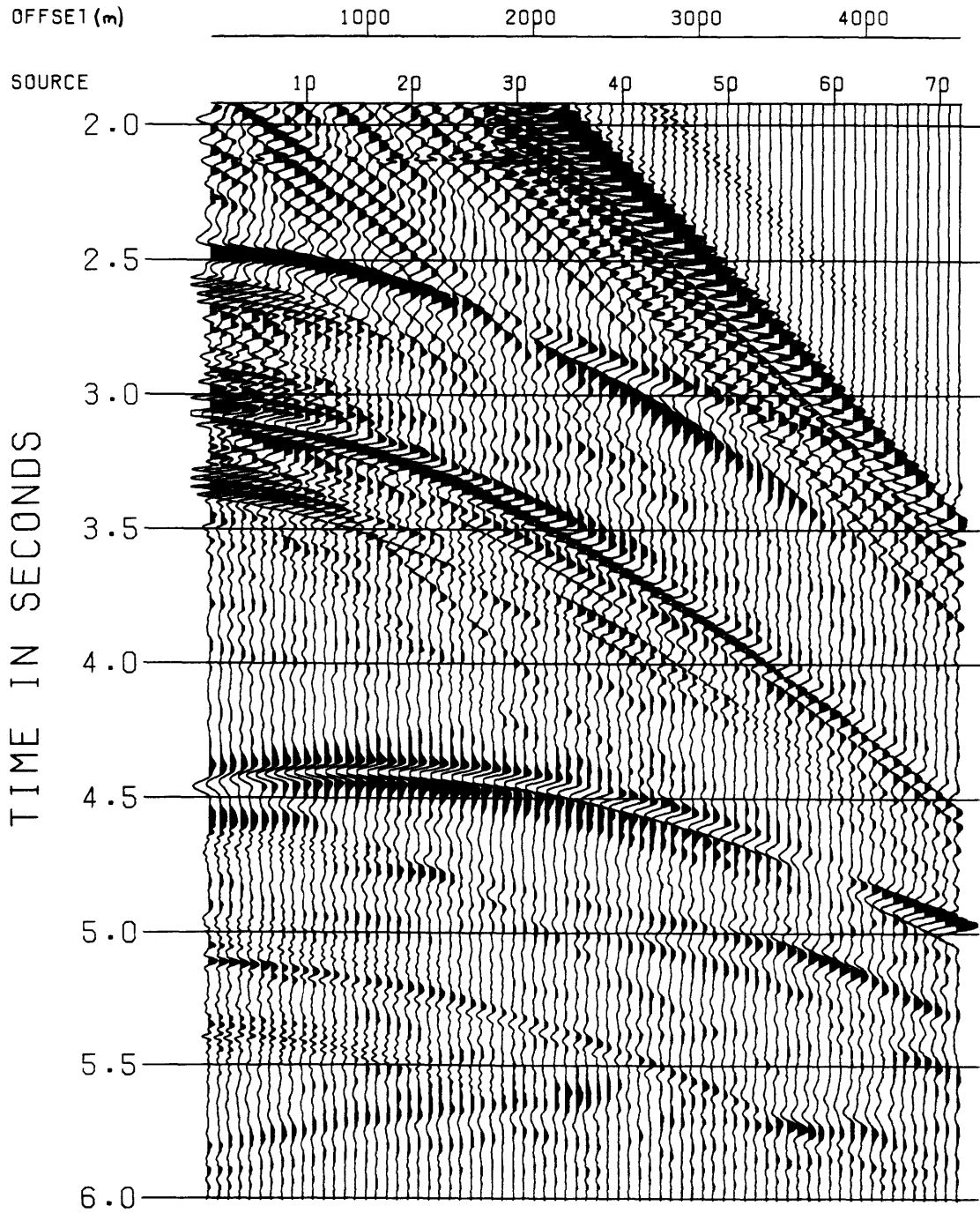
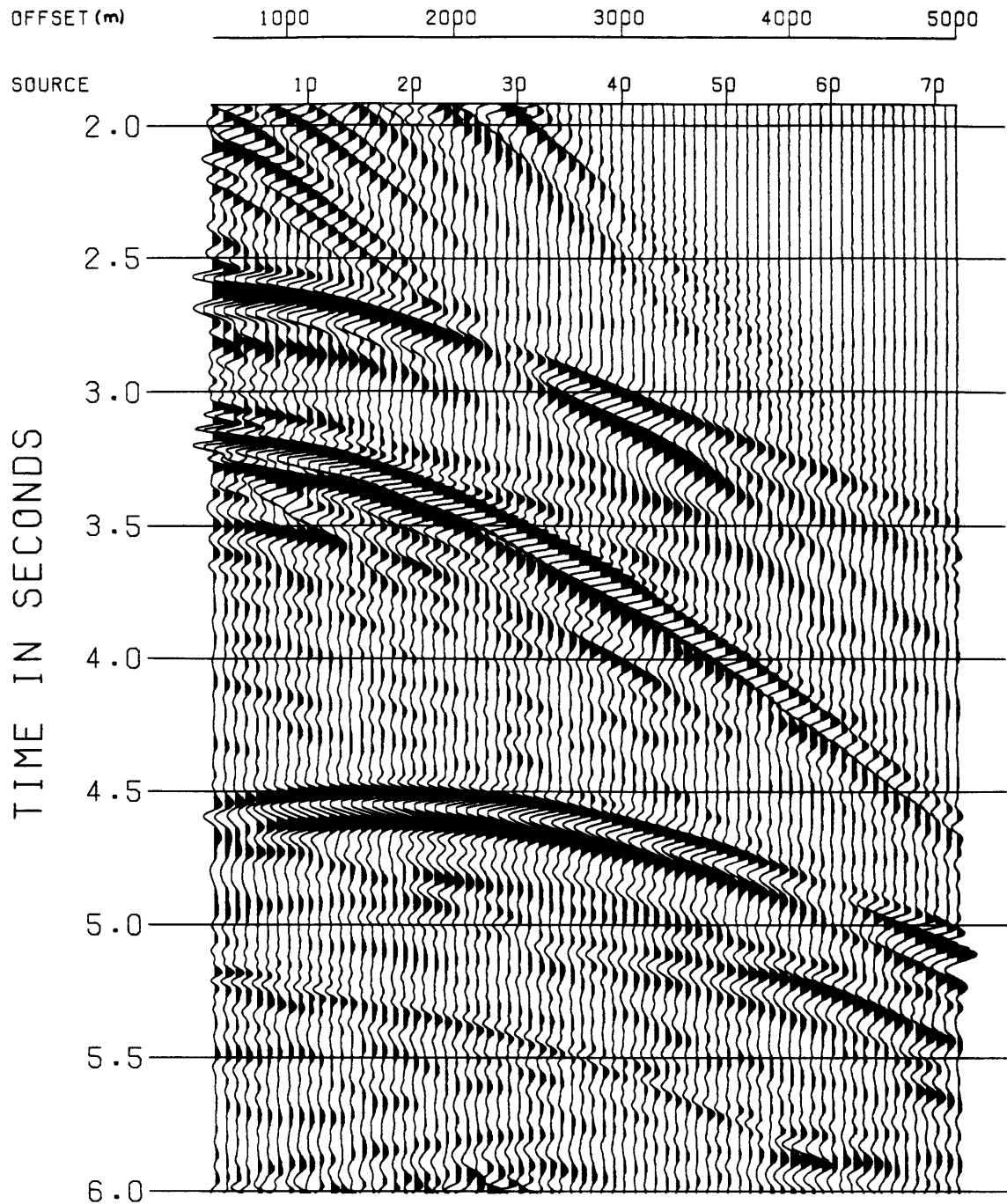


Figure 3-8: (b) Deconvolved ultrasonic raw data time section.

FK Filtered TIME SECTION

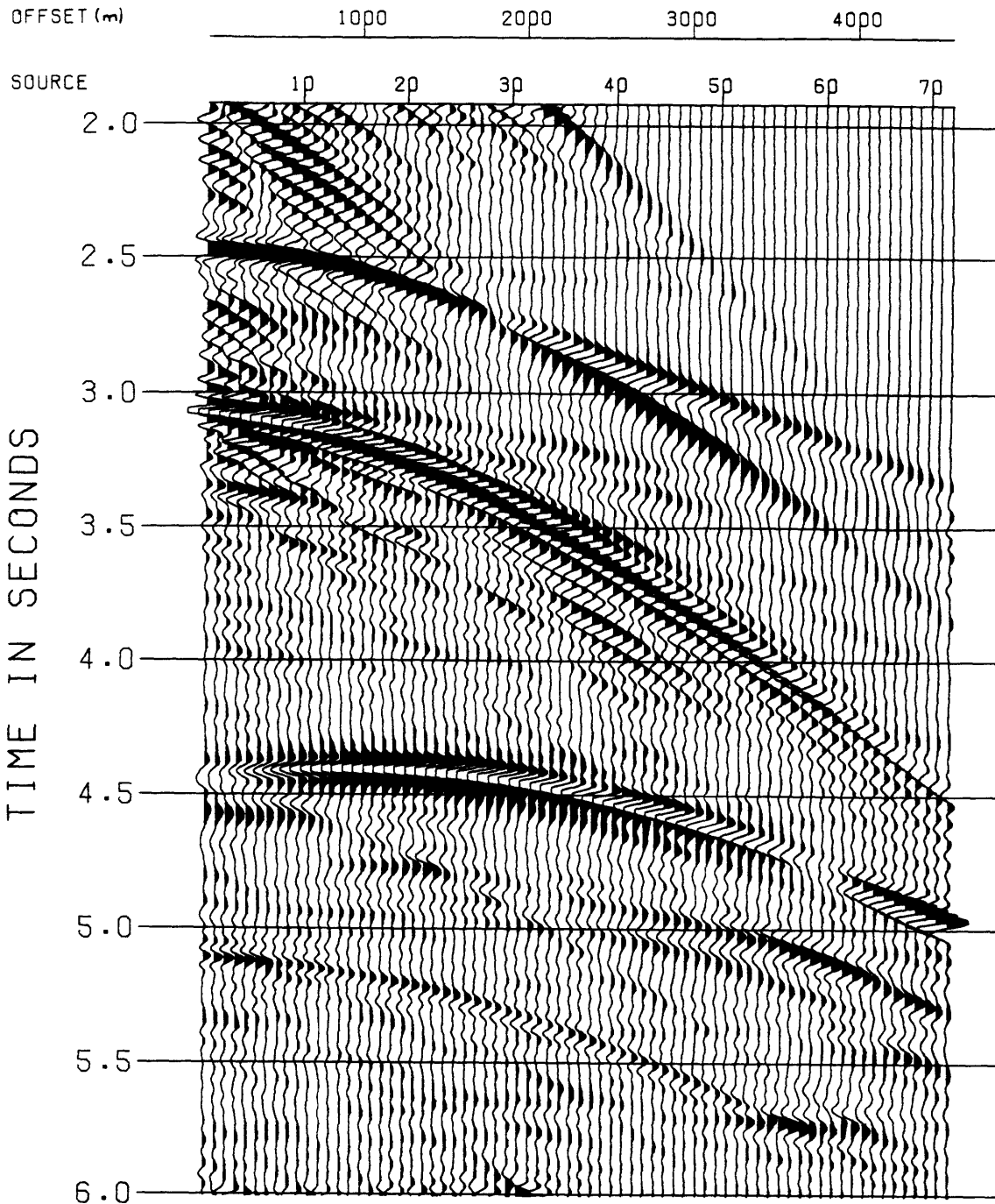


Scale Factor = 20.000

FK filtering : LP Boxcar 20 Hz
+ Fan filter rejection
0 - 1550 m/s

Figure 3-9: (a) FK filtered ultrasonic raw data time section.

DECONVOLVED FK Filtered TIME SECTION



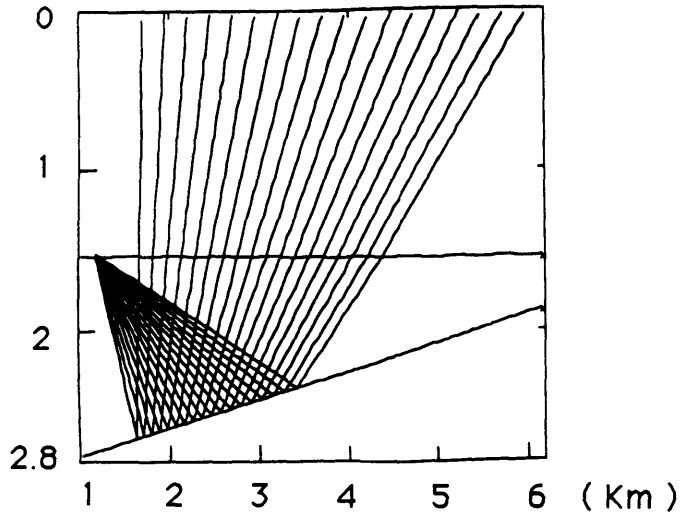
Scale Factor = 20,000

FK filtering : LP Boxcar 20 Hz
+ Fan filter rejection 0 - 1550 m/s

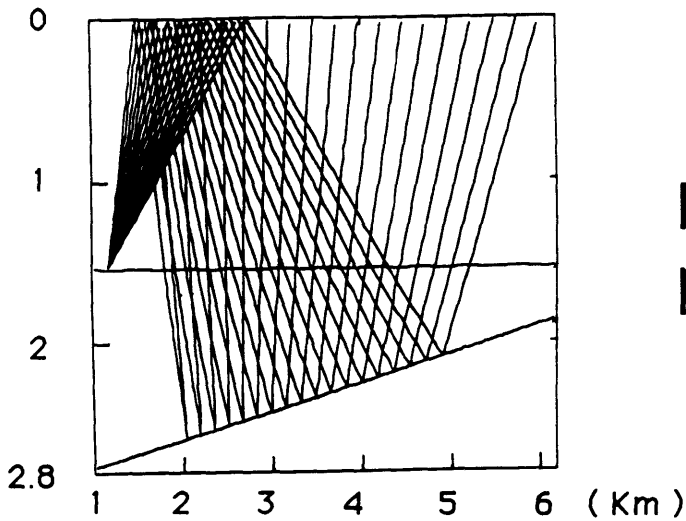
Figure 3-9: (b) FK filtered ultrasonic deconvolved time section.

ILLUMINATION OF THE INTERFACE

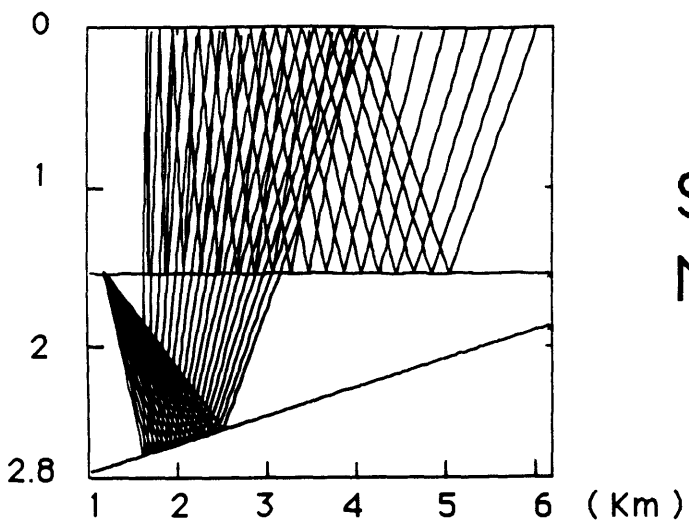
VERTICAL
EXAGGERATION = 2



PRIMARY RAYS



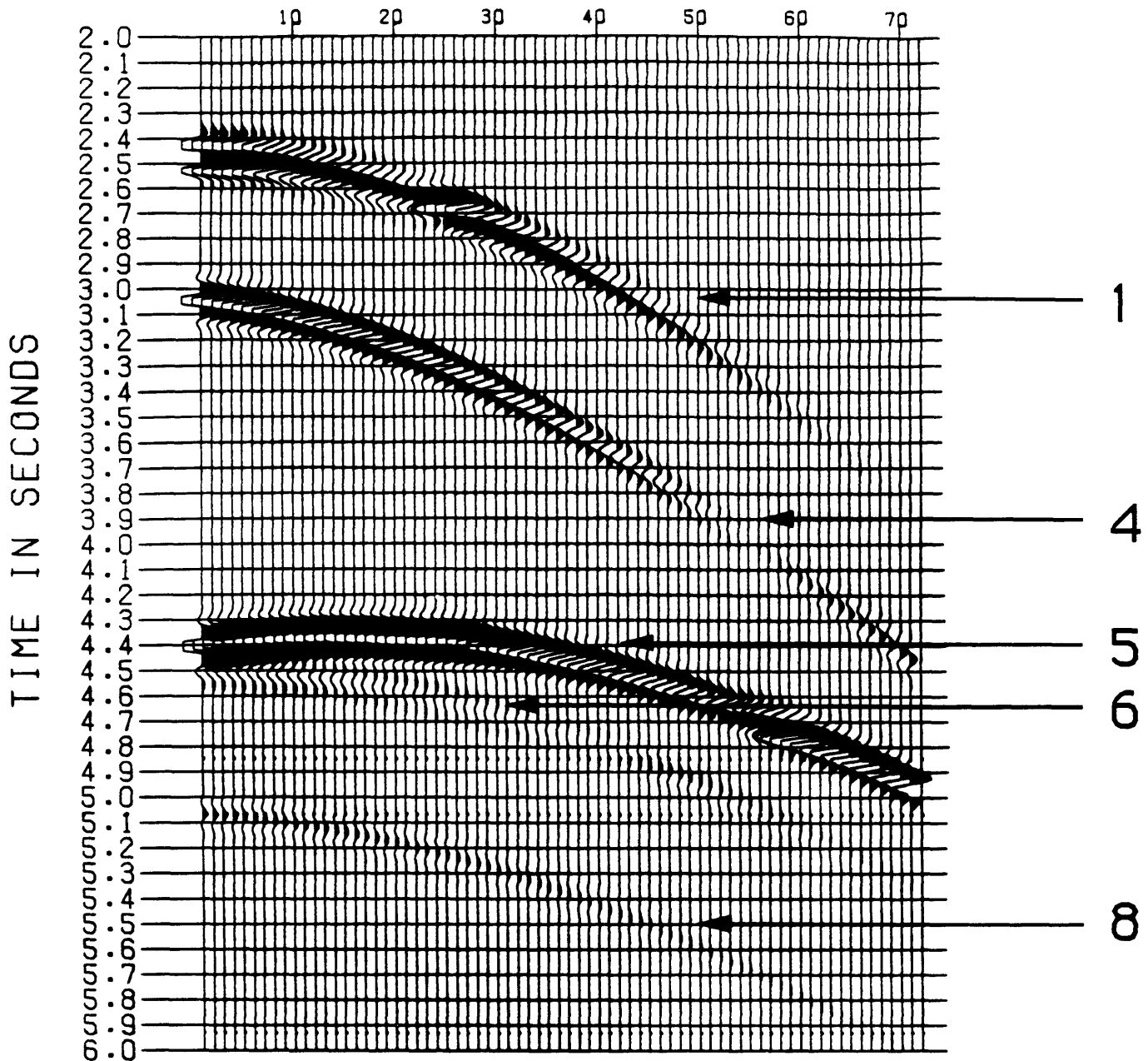
RECEIVER
MULTIPLE RAYS



SOURCE
MULTIPLE RAYS

Figure 3-10: Coverage of the dip interface by the three main P waves of interest.

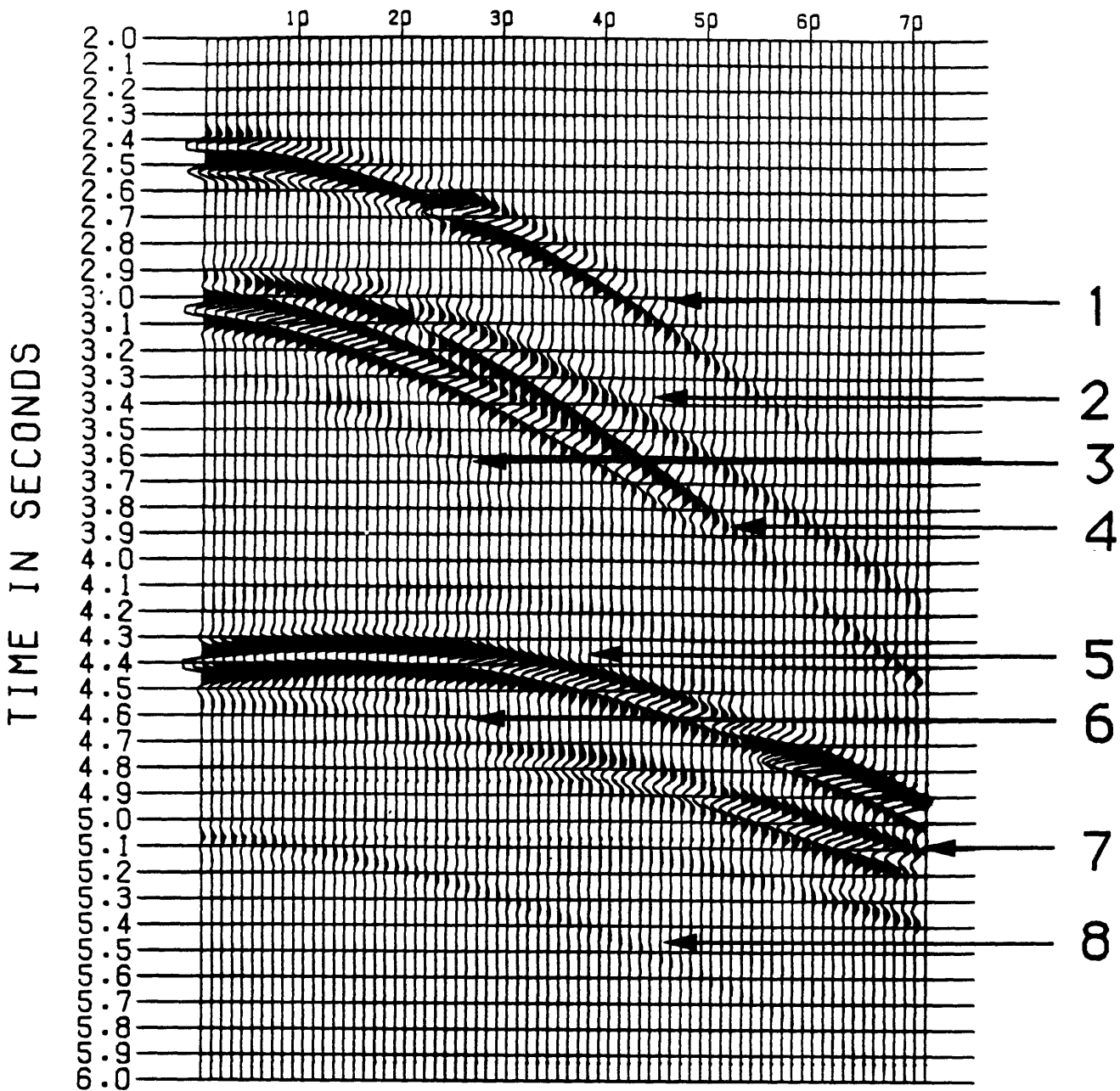
PARTIAL SYNTHETIC TIME SECTION



	1 - PRIMARY	WNNW
	4 - FIRST WATER MULTIPLE	WWW
Major Waves of Interest	5 - RECEIVER MULTIPLE	WNNWW
	6 - SOURCE MULTIPLE	WWWNNW
	8 - SECOND WATER MULTIPLE	WWWWW

Figure 3-11: Partial synthetic time section showing the five waves of interest involved. W means a travel in water and N a travel in neoprene.

COMPLETE SYNTHETIC TIME SECTION

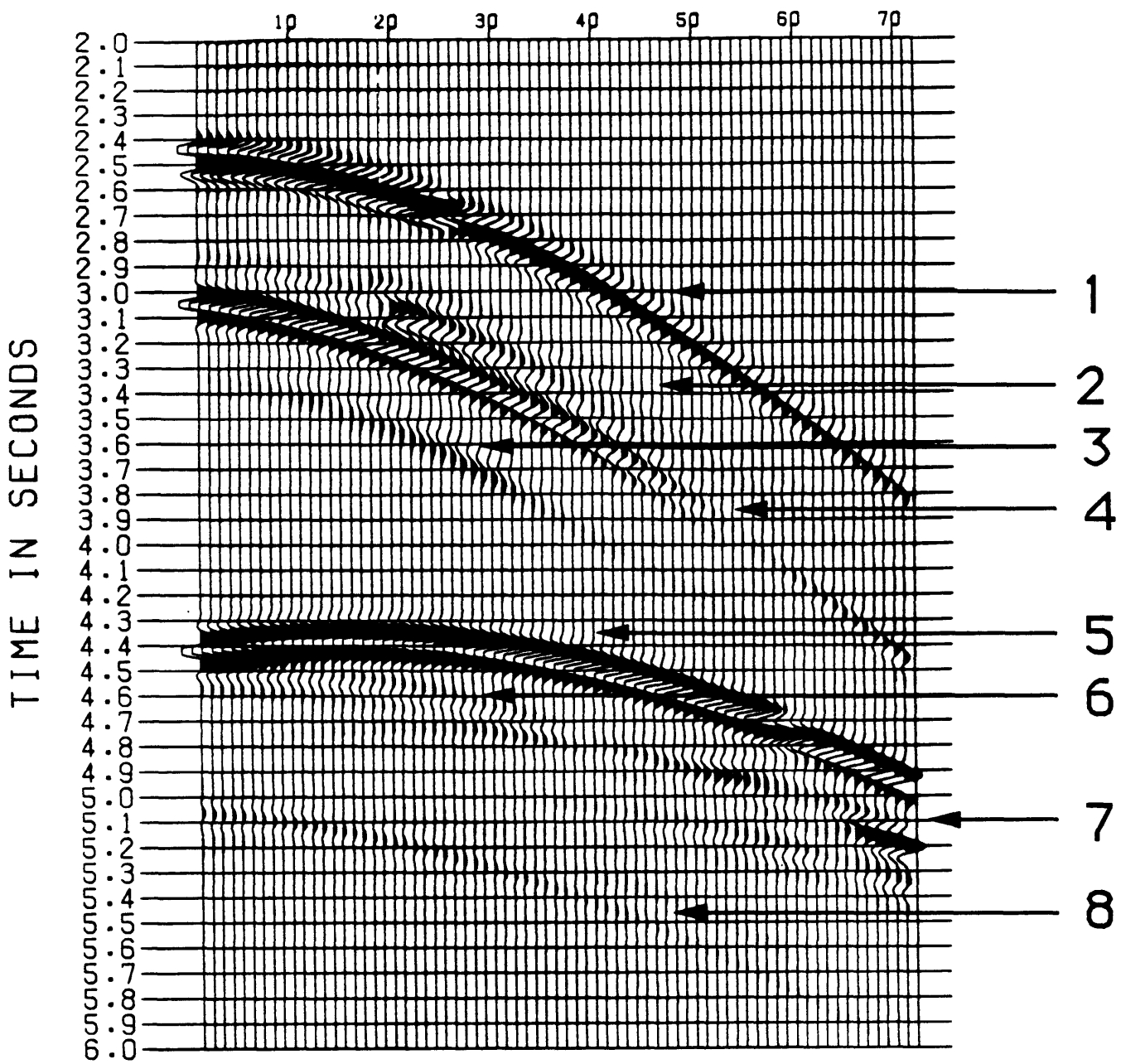


Major Waves of Interest

- | | |
|---|--------|
| 1 - PRIMARY | WNNW |
| 2 - PRIMARY - CONVERTED WAVES | WNNW |
| 3 - PRIMARY - MULTIPLES IN NEOPRENE | WNNNNW |
| 4 - FIRST WATER MULTIPLE | WWW |
| 5 - RECEIVER MULTIPLE | WNNWW |
| 6 - SOURCE MULTIPLE | WWNNW |
| 7 - RECEIVER/SOURCE MULTIPLE- CONVERTED | |
| 8 - SECOND WATER MULTIPLE | WWWWW |

Figure 3-12: Complete synthetic time section including first and multiple waves in neoprene including converted waves and simple converted waves in neoprene issued from the receiver or source water multiple. Waves traveling inside the aluminum layer are not included.

SYNTHETIC TIME SECTION WITH A THIN WATER LAYER BETWEEN NEOPRENE AND ALUMINIUM



Major Waves
of Interest

- | | |
|---|--------|
| 1 - PRIMARY | WNNW |
| 2 - PRIMARY - CONVERTED WAVES | WNNW |
| 3 - PRIMARY - MULTIPLES IN NEOPRENE | WNNNNW |
| 4 - FIRST WATER MULTIPLE | WWW |
| 5 - RECEIVER MULTIPLE | WNNWW |
| 6 - SOURCE MULTIPLE | WWWNNW |
| 7 - RECEIVER/SOURCE MULTIPLE- CONVERTED | |
| 8 - SECOND WATER MULTIPLE | WWWWW |

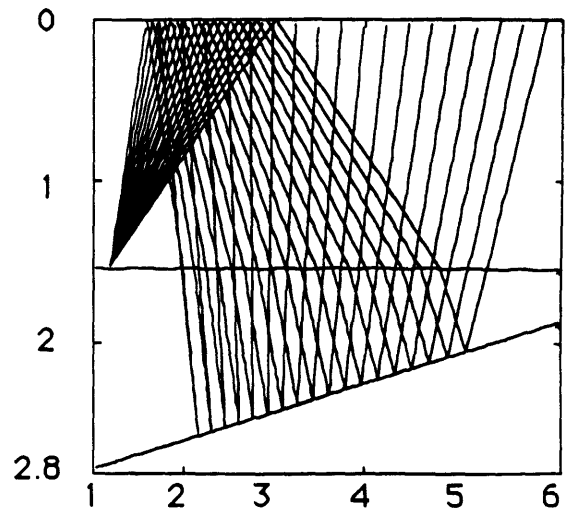
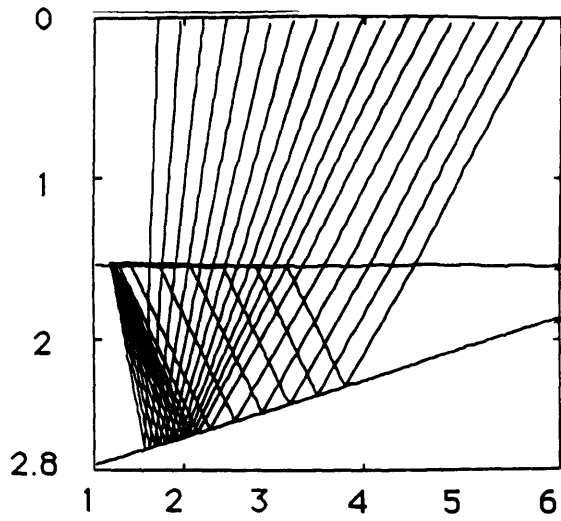
Figure 3-13: Complete synthetic time section with a very thin water layer between the aluminum and the neoprene.

CONVERTED WAVES COVERAGE

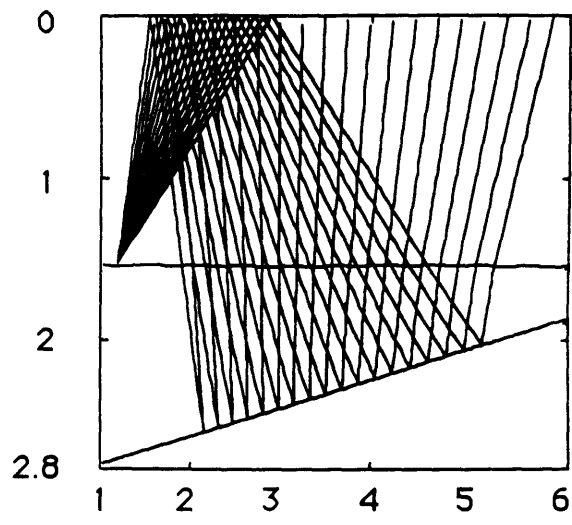
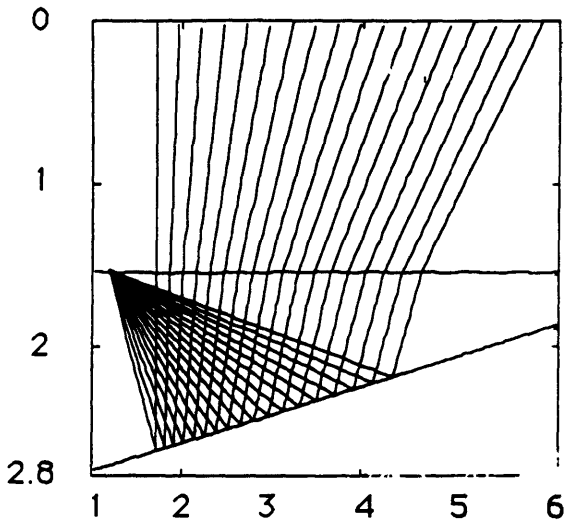
VERTICAL EXAGGERATION = 2

PRIMARY RAYS

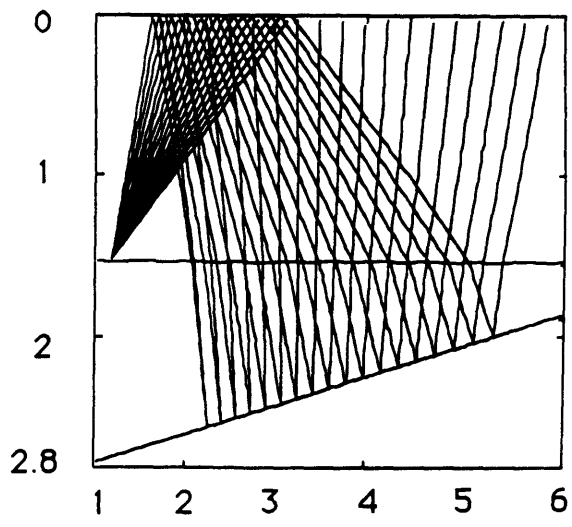
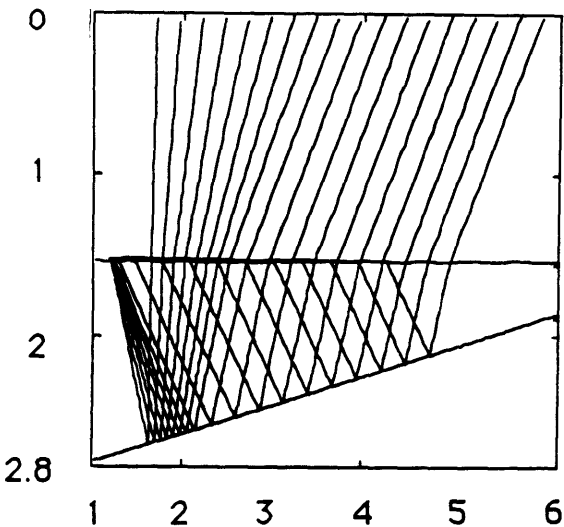
RECEIVER
MULTIPLE RAYS



PS



SP



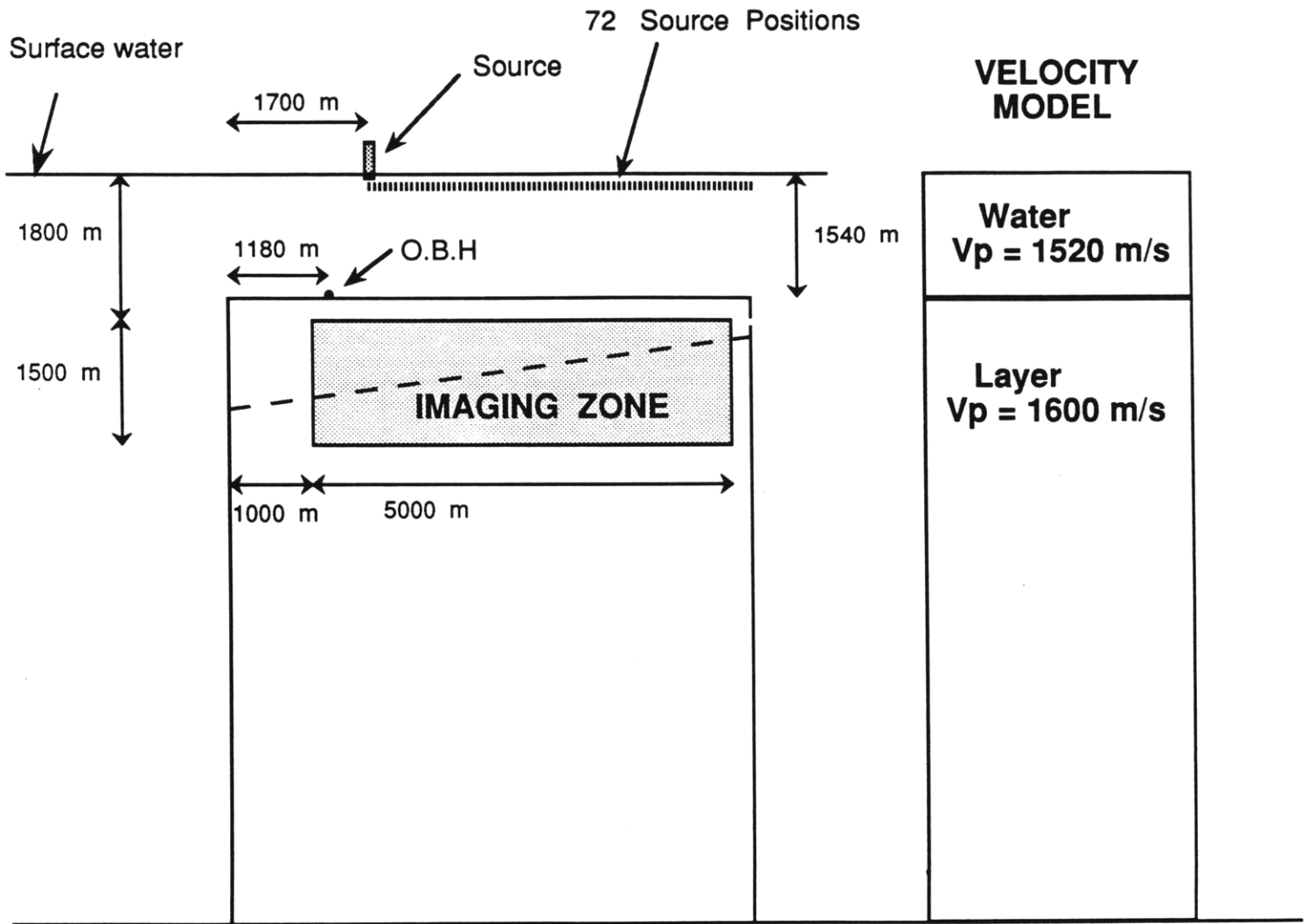
SS

Figure 3-14: Ray tracing for the converted waves.

Imaging zone - model 1

2D profile

Scale factor used : 20000



Scale 1:80000

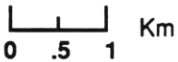


Figure 3-15: Dimension and position of the imaging zone, velocity model entered in the migration program.

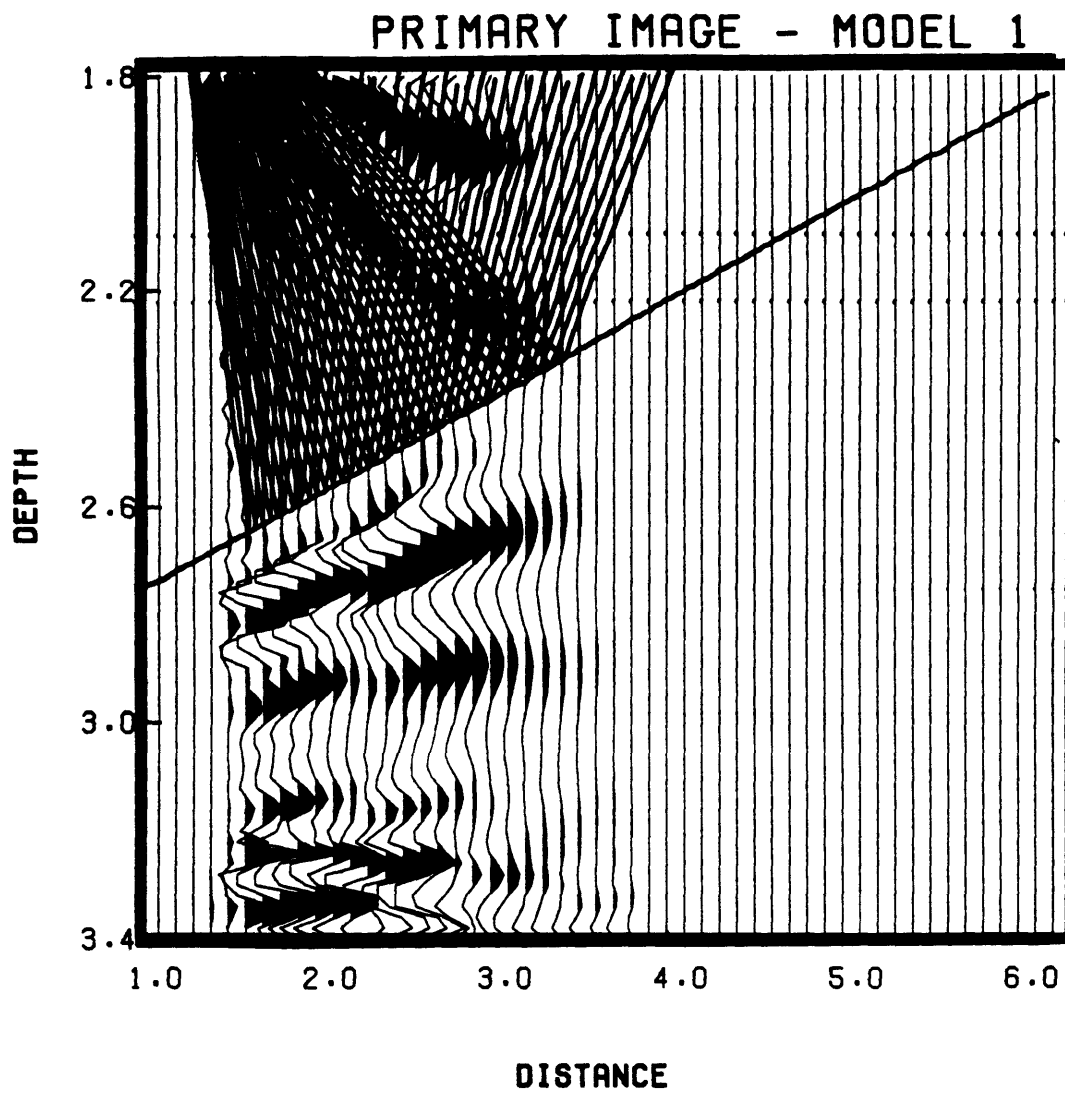
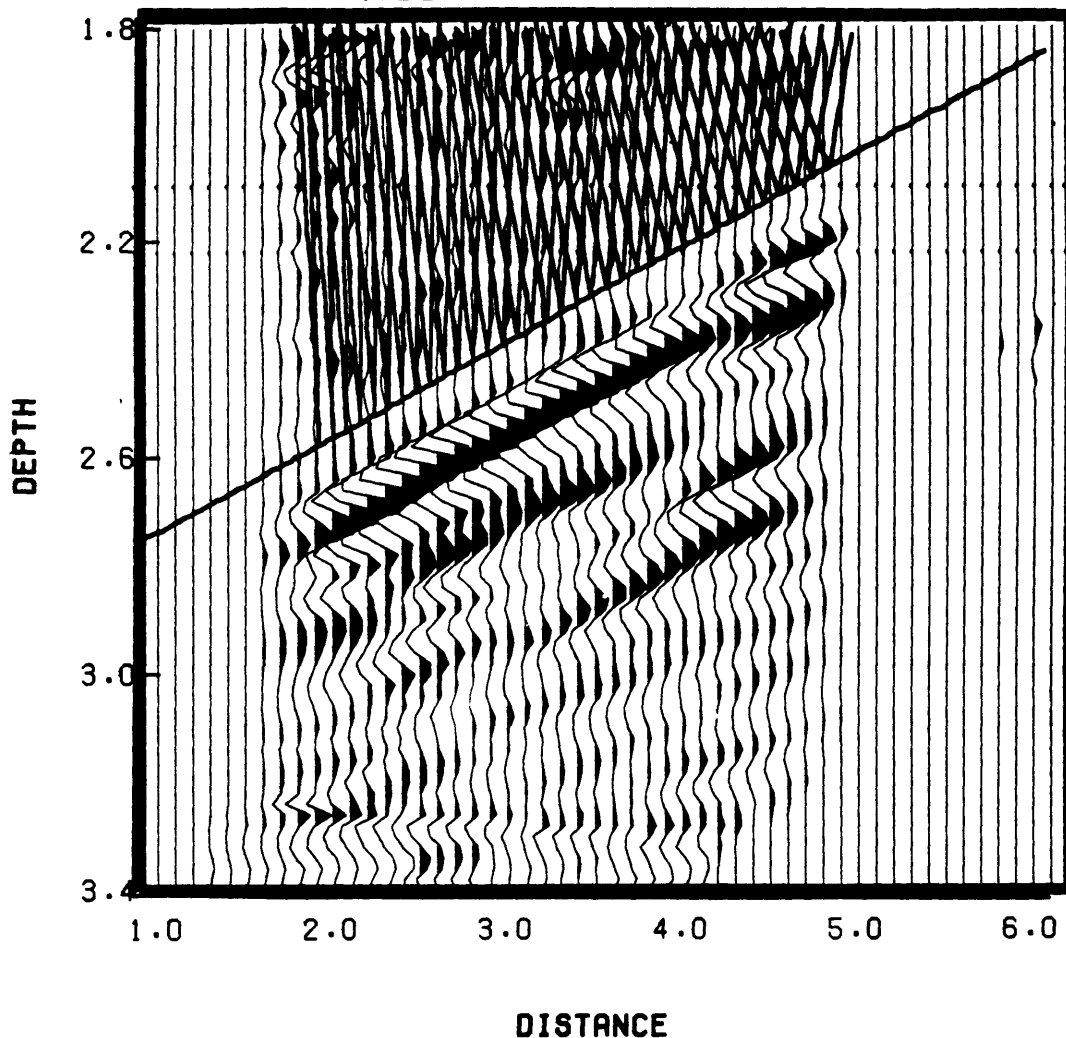


Figure 3-16: Primary image from the ultrasonic experiment. The true position of the layer and the ray coverage are superposed to the depth section plotted in RMS scale with normal polarity.

MULTIPLE IMAGE - MODEL 1



-10 +/-10 DIP FILTER

POLARITY -1

Figure 3-17: Receiver multiple image plotted in RMS scale with inverse polarity.

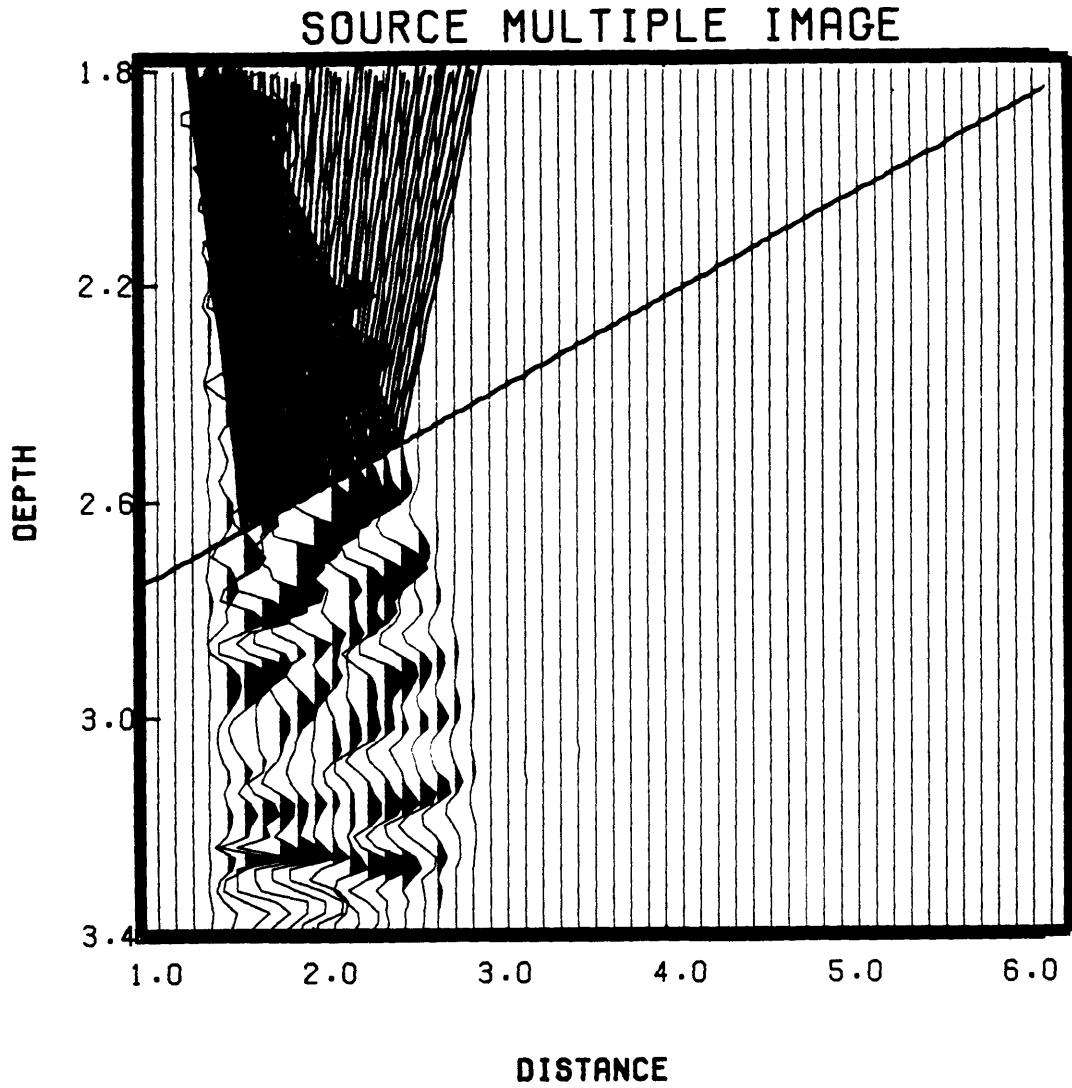
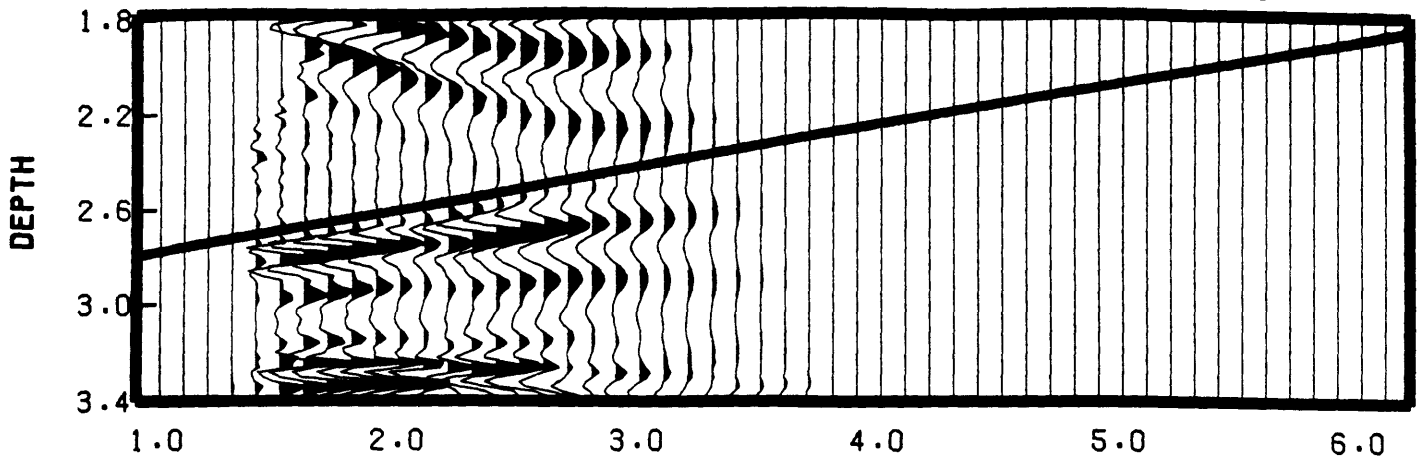
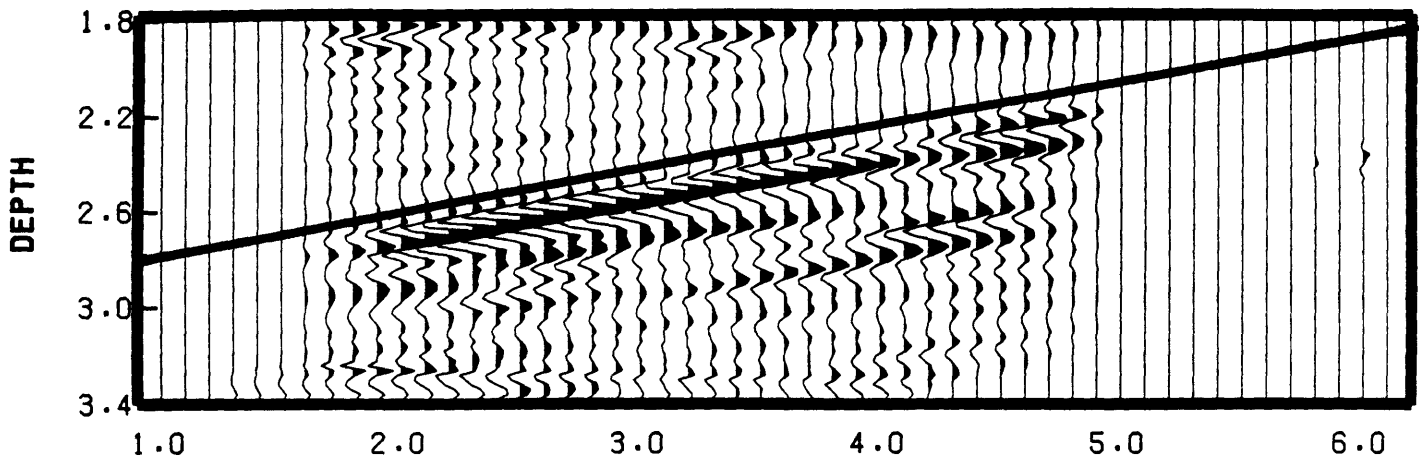


Figure 3-18: Source multiple image plotted in RMS scale with inverse polarity.

PRIMARY IMAGE - POLARITY +1



MULTIPLE IMAGE - POLARITY -1



PRIMARY + MULTIPLE IMAGE

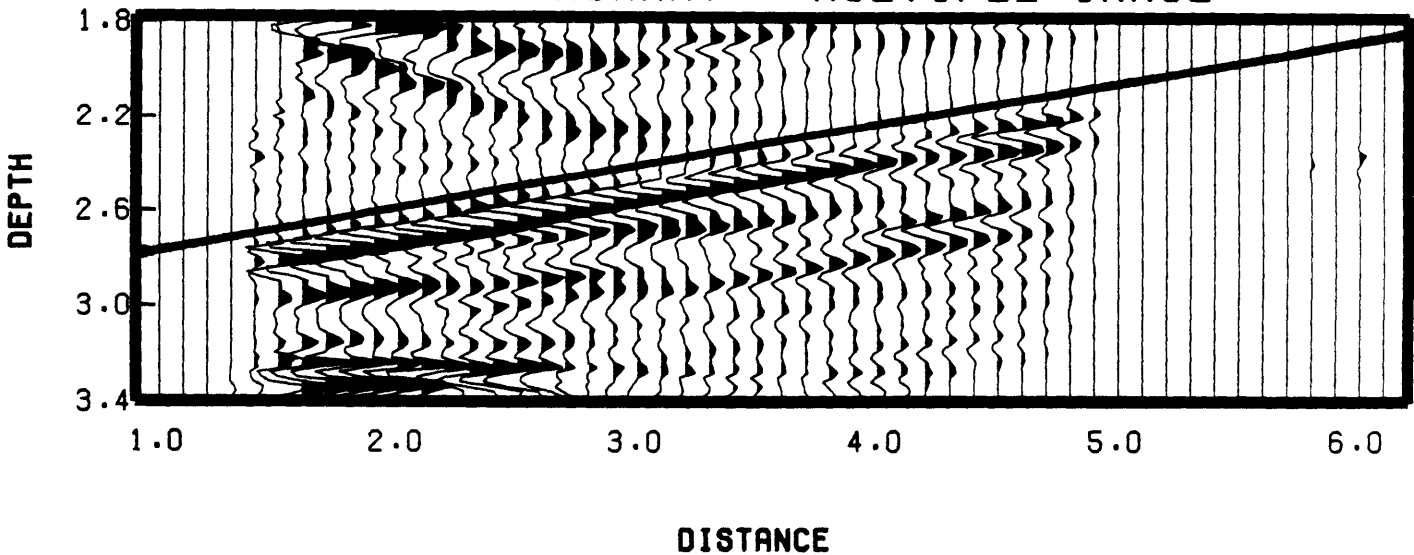


Figure 3-19: (a) Migration of the raw data time section. Plot of the primary, the receiver multiple and the total images with the same scale. The whole primary image is included in the total image.

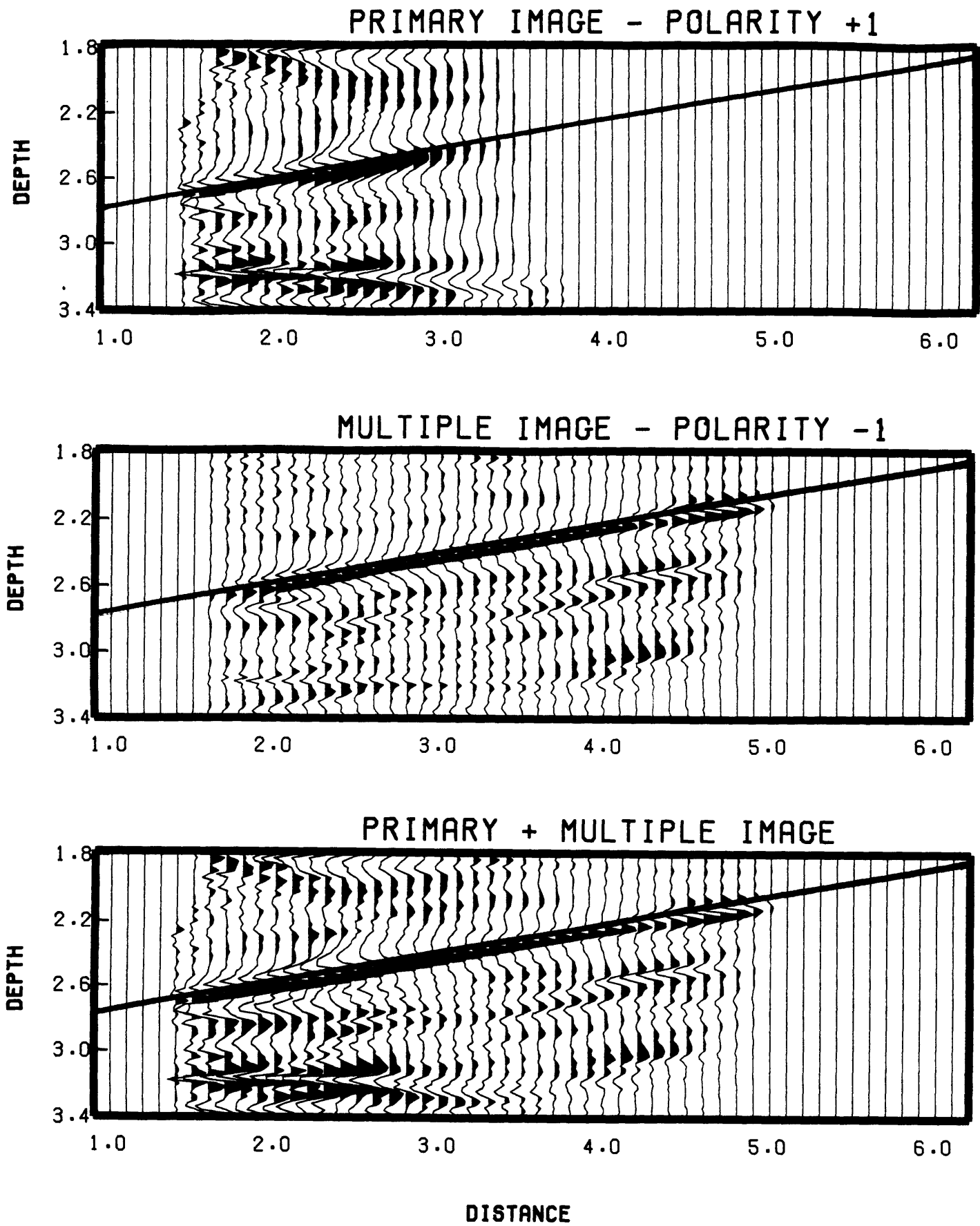
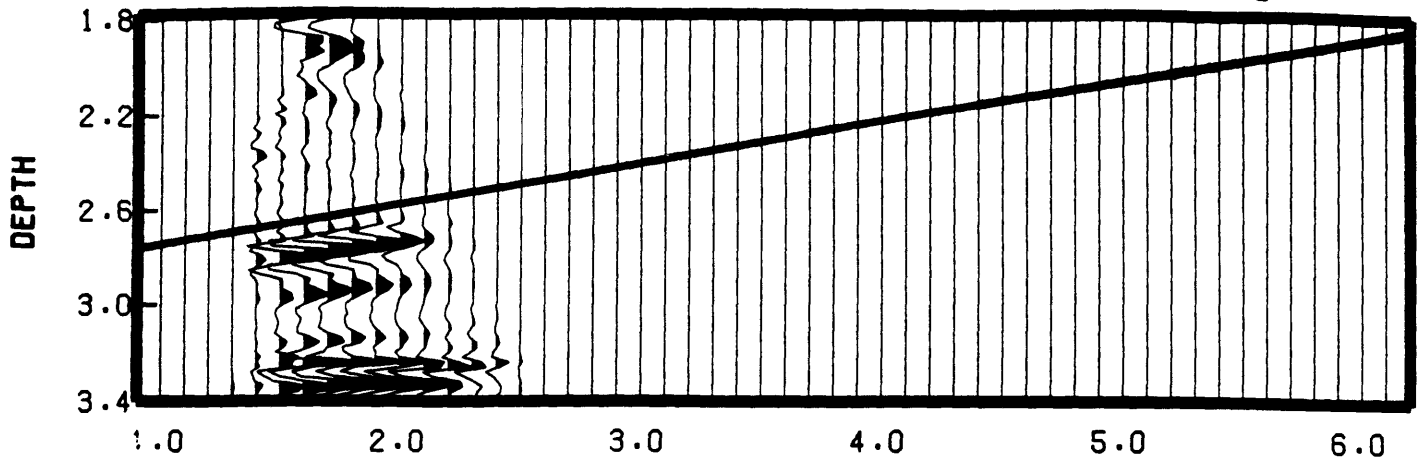
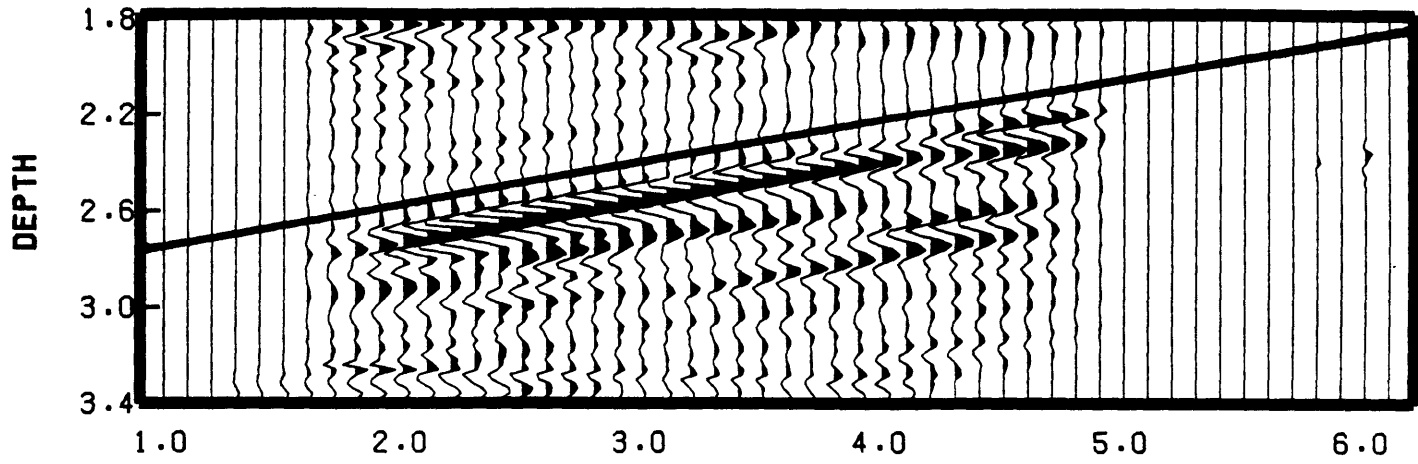


Figure 3-19: (b) Migration of the deconvolved time section. Plot of the primary, the receiver multiple and the total images with the same scale. The whole primary image is included in the total image.

PRIMARY IMAGE - POLARITY +1



MULTIPLE IMAGE - POLARITY -1



PRIMARY + MULTIPLE IMAGE

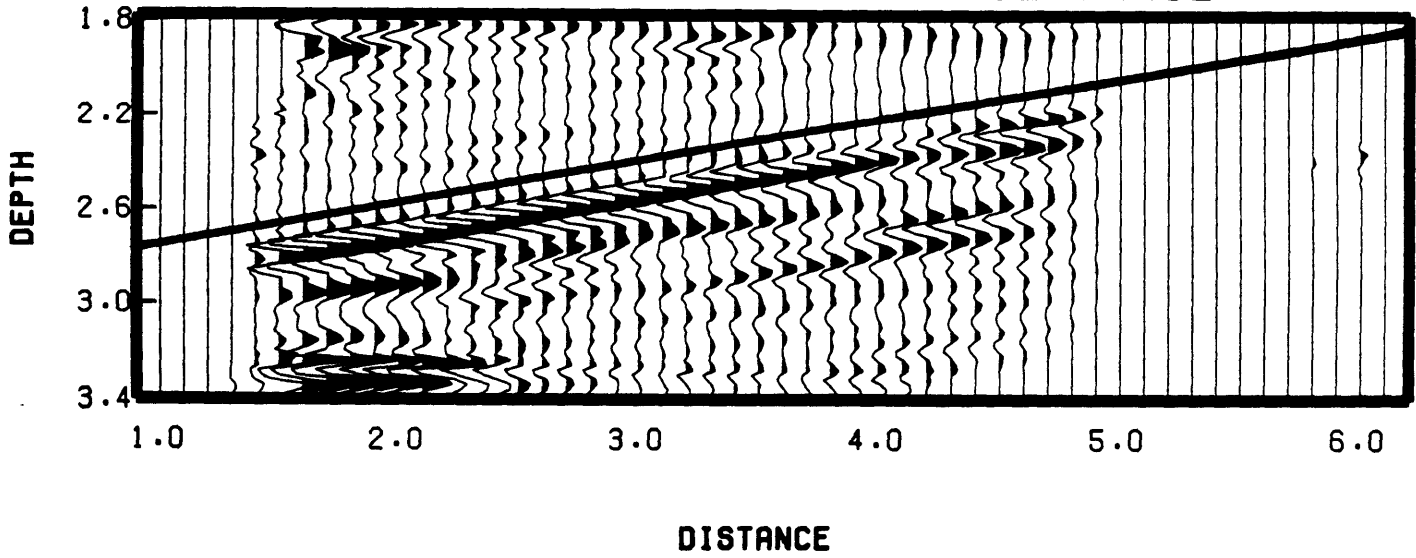
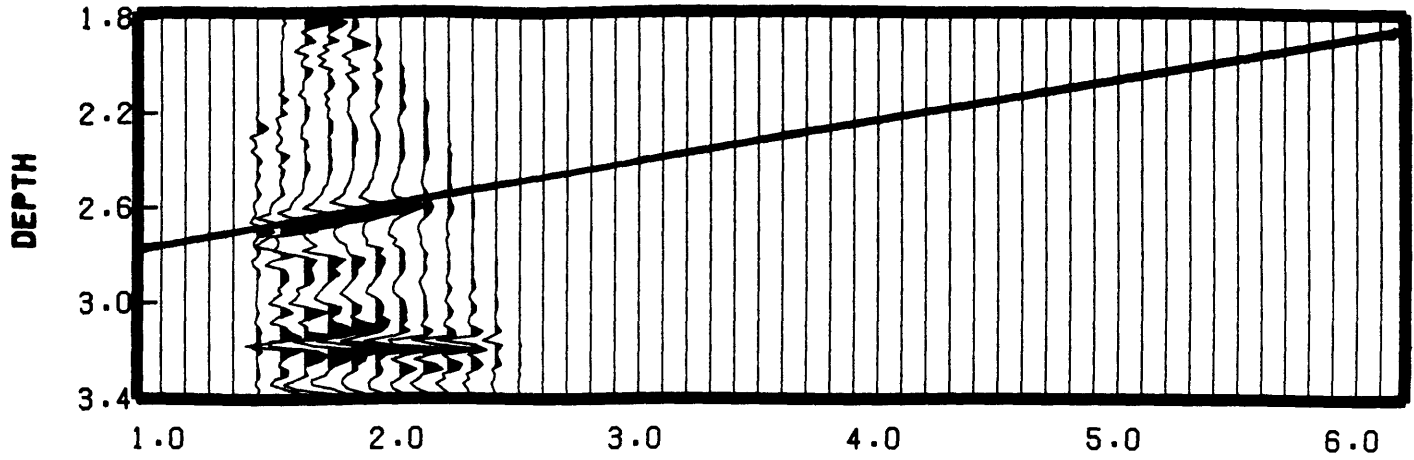
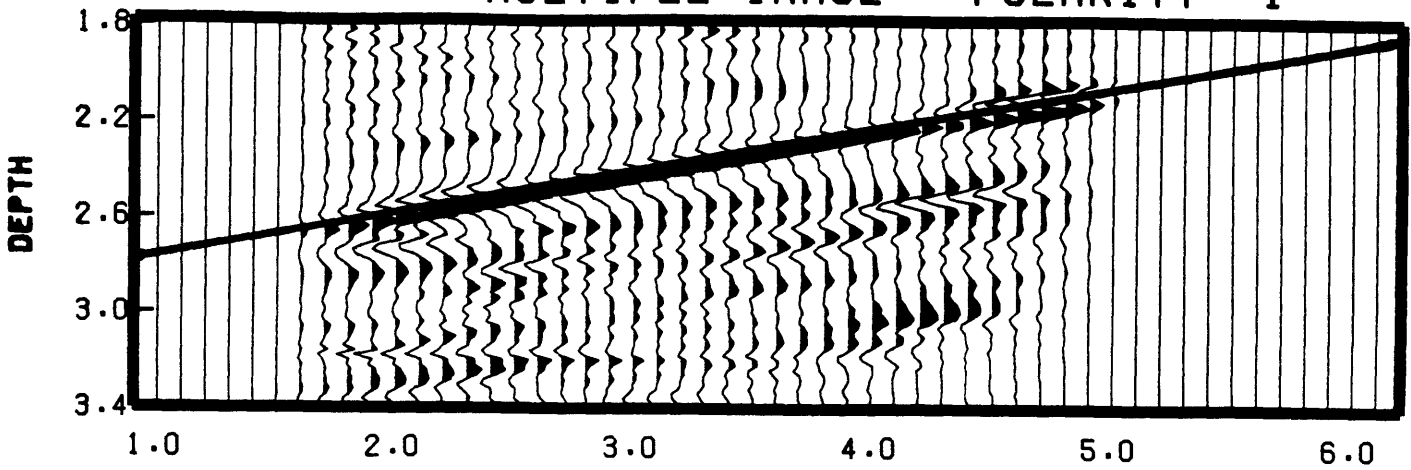


Figure 3-20: (a) Idem as figure 3-19 (a) except that only the precritical information of the primary image is plotted and included in the total image.

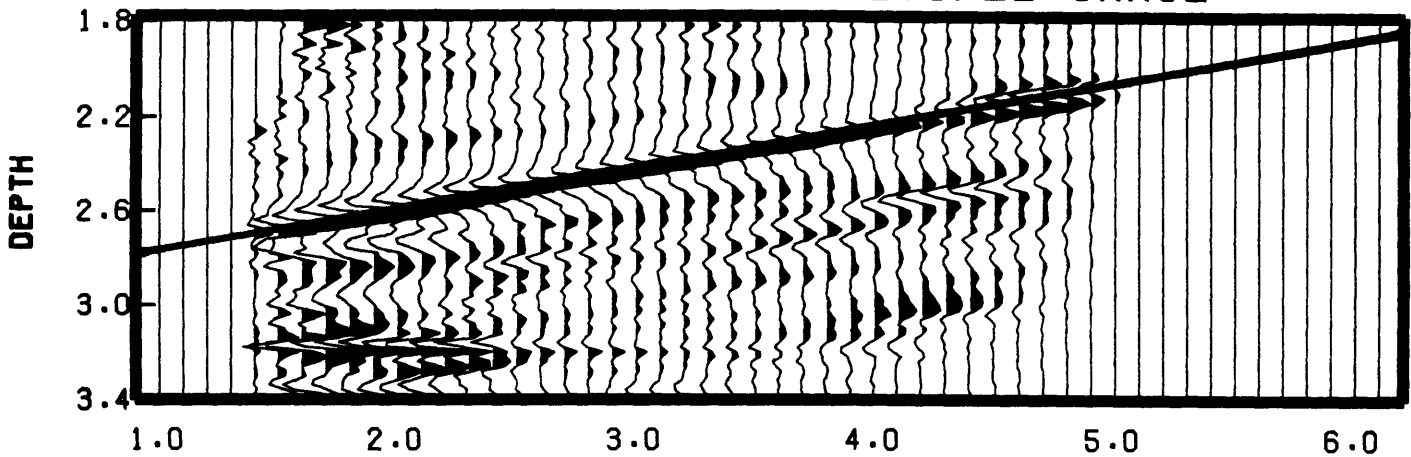
PRIMARY IMAGE - POLARITY +1



MULTIPLE IMAGE - POLARITY -1



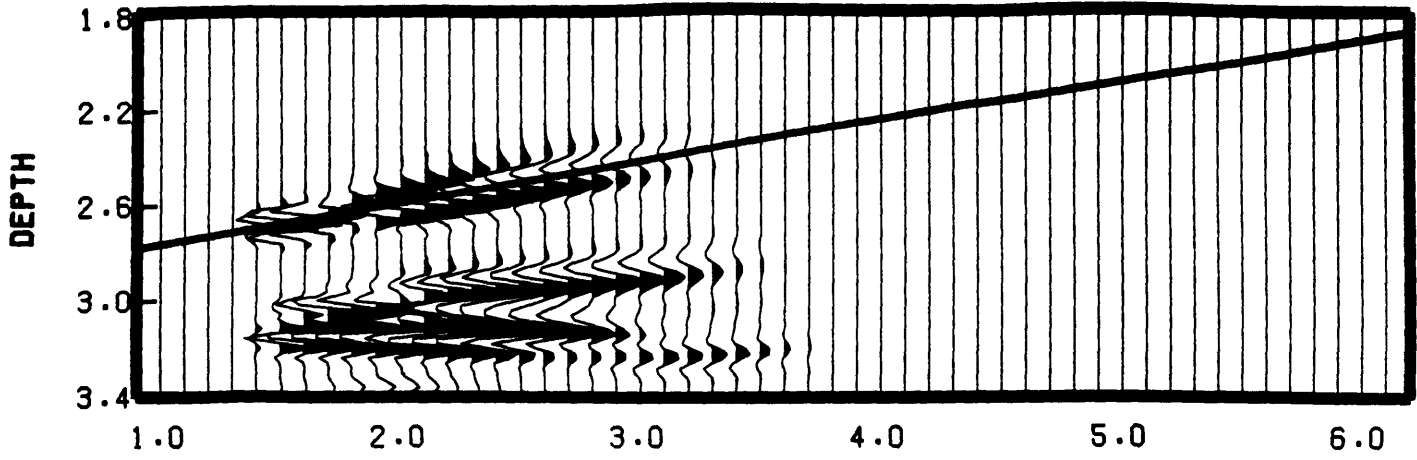
PRIMARY + MULTIPLE IMAGE



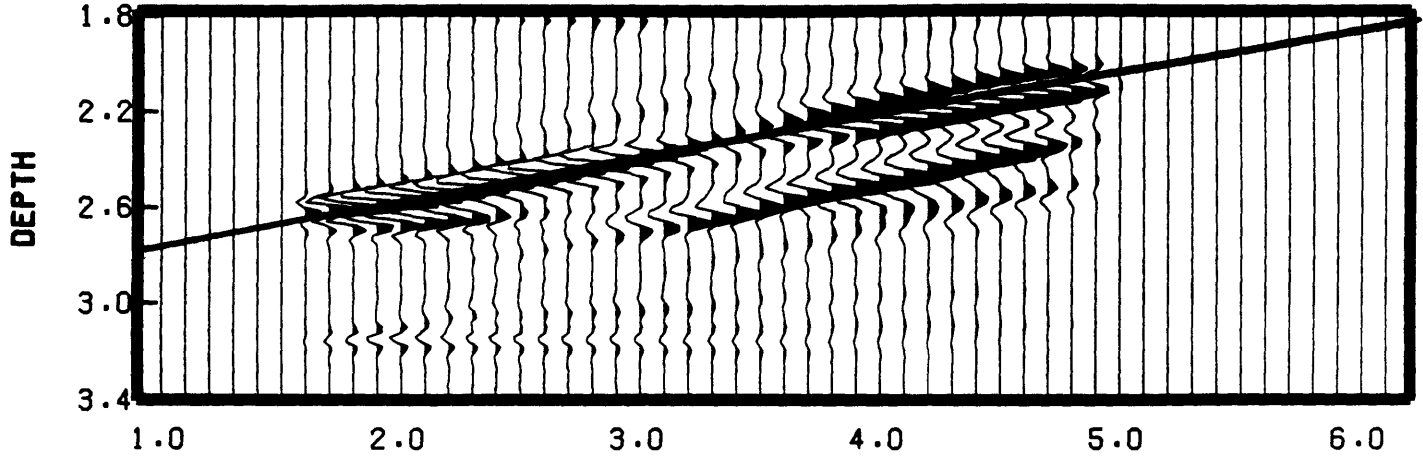
DISTANCE

Figure 3-20: (b) Idem as figure 3-19 (b) except that only the precritical information of the primary image is plotted and included in the total image.

PRIM SYNTHETIC IMAGE - POL +1



MULT SYNTHETIC IMAGE - POL -1



PRIM + MULT SYNTHETIC IMAGE

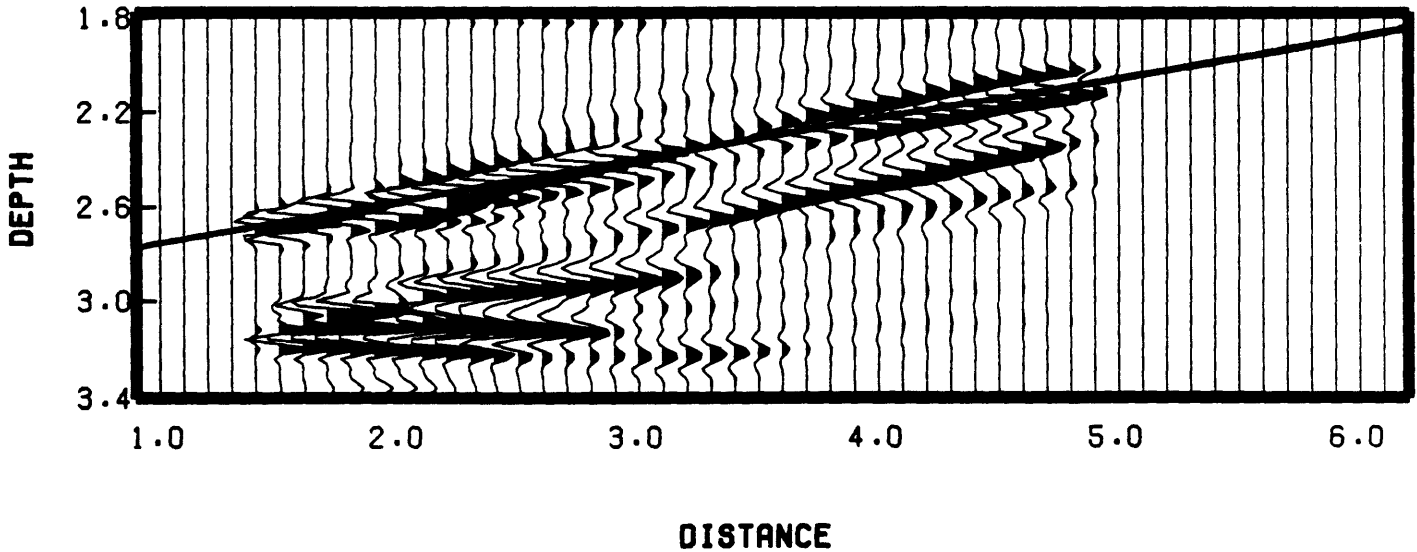


Figure 3-21: Images from the complete synthetic section. Complete primary, receiver multiple and total images.

Chapter 4

Fault unconformity model ; Conclusion

4.1 Description

The model shown in figure 4-1 consists of three layers. The neoprene block same as that of chapter 3 is used to simulate the first sedimentary layer and has a 10 degree dipping interface with the two other layers below. Again this layer was not bonded for the purpose of convenience. The intermediate layer is made of an epoxy-aluminum composite material and the half-space is aluminum.

The layer parameters (V_p, V_s, Q_p, Q_s) and the geometry designed to generate the synthetic time sections are given in figure 4-2. For the same reasons explained in chapter 3, the small difference between the laboratory set-up and the synthetic model does not affect the comparison between ultrasonic and synthetic models.

In this case, instead of a single O.B.H, a water bottom streamer with 24 channels is used. The scale factor of 12000 (figure 4-3) is chosen this time to scale laboratory model dimensions in inches to those corresponding to the real earth equivalent in feet.

4.2 Raw data

4.2.1 Ultrasonic data

The data acquisition parameters are given in figure 4-4. The experimental procedure is similar to that of the previous chapter and is not discussed again. A stacking value of 64 is chosen to keep the acquisition time (10 hours without any real-time HP plot) reasonable. Water level was precisely measured and no change due to evaporation during the experiment was detected. Because of limited averaging, the signal-to-noise ratio is 52db full scale, and lower than that of the case described in chapter 3.

The acquisition delay time of $50\mu\text{s}$ scales to 0.6 sec. Three raw data time sections are shown in figure 4-5 (a) and the deconvolved sections in figure 4-5 (b). Among the 24 receivers, numbers 1,13,24 are plotted. It can be seen that some traces are missing: over the 1152 traces recorded, the 9 missing are due to some temporary oscilloscope malfunctions. It is easier to identify the arrivals on the deconvolved sections. We label the events with the following convention:

- R1 is the primary reflection from the neoprene-composite interface.
- R2 is the primary reflection from the composite-aluminum interface.
- D1 is the primary diffraction from the upper corner of the fault.
- D2 is the primary diffraction from the lower corner of the fault.
- M1 is the receiver multiple reflection from the neoprene-composite interface.
- M2 is the receiver multiple reflection from the composite-aluminum interface.

Receiver 1

R1 and D1 start at 1.0 sec and overlap on the apex of the hyperbola; R2 at 1.15 sec; M1 at 1.95 sec; M2 at 2.2 sec.

Receiver 13

R1 starts at 0.9 sec; D1 at 1.0 sec; R2 at 1.1 sec; M1 at 1.9 sec; M2 at 2.15 sec.

Receiver 24

R1 starts at 0.8 sec; D1 at 1.05 sec; R2 at 1.05 sec; M1 at 1.85 sec; M2 at 2.1 sec.

Comments

D2 and the receiver multiple diffractions are difficult to identify. The reason is that they have smaller amplitudes and that there are lots of converted waves. In the raw data time sections shown in figure 4-5 (a), the diffraction, which occurs at the apex of the simple water multiple reflection (previously labelled WWW in chapter 3) at 1.6 sec, is a clear illustration of the hydrophone receiver backscattering. This causes the obvious anomaly in the deconvolved sections (figure 4-5 (b)) for this event at 1.5 sec.

4.2.2 Synthetic data

For the model shown in figure 4-2, the synthetic seismograms are calculated. The ray diagrams are shown in figure 4-6 and the synthetic section corresponding to the receivers 1,13,24 in figure 4-7. In calculated synthetic seismograms, only the primary, source and receiver multiples reflections and first and second water multiples are included. The wavelet is a 20Hz zero-phase Gaussian envelope modulated cosine function. We can identify the waves, characterized in the previous section, except that diffractions are absent. In particular, we can see the duplication of the primary and the receiver multiple reflections R2 and M2 due to the fault. The discontinuous behavior of these duplications is due to the ray computation near the sharp corners of the fault. However, these synthetic seismograms help us to identify properly the waves which will show up in the ultrasonic deconvolved time sections (figure 4-5 (b)).

4.3 Images

The imaging zone in figure 4-8 has been chosen according to the ray coverage. We want to image the composite-aluminum interface in one step. Therefore, the velocity model consists of the water layer, the true geometry and velocity of the neoprene layer and a semi-infinite composite material layer. No dip filter has been used.

4.3.1 Ultrasonic data

The model has been superposed to the images which are plotted at true scale (without any vertical exaggeration). We may expect some small differences due to the tolerances in the dimensions and velocities of the true physical model. All the figures show the primary and the multiple images on the same amplitude scale. The composite image, sum of the primary and the multiple images, is plotted on an amplitude scale twice smaller. The figures labelled (a) are the images obtained with the raw data time sections and those labelled (b) are the images obtained with the deconvolved sections.

Figures 4-9 show that a single receiver point (number 13) images correctly the zones covered by the rays arriving at that receiver (figure 4-6). In particular, the lower part of the fault is well resolved in the primary image. The low-frequency distortion of the wavelet at the second interface is a natural consequence of the higher velocity of the second composite layer. The addition of the 24 individual images is shown in figures 4-10. Although the "flat" part of the interface is clearly delineated, the fault is not fully imaged. The poor imaging of the fault is caused by the migration of the other converted waves which align fictitious images along the main slopes of the dipping neoprene-composite interface and blur the fault image. This clearly appears when we look at individual images (for one receiver) or at the following figures 4-11 and 4-12. Indeed, some individual images show the fault better than others do, i.e., the addition process does not always helps in this case. In particular, the zones

which have a low ray coverage for the 24 receivers tend to disappear in the total image. Three total images of 8 successive receiver points, given in figures 4.11 and 4.12 illustrate that fact. In particular, the fault is clearly delineated in the primary image corresponding to the sum of the receiver 9 to 16 (figures 4-11) and the upper part of the fault is successfully resolved in the receiver multiple image corresponding to the sum of the receivers 1 to 8 (figures 4-12).

The matching is not perfect between the theoretical boundaries of the interfaces and the images migrated from the deconvolved sections. This is due to the tolerances in the dimensions of the ultrasonic model. For example, the interface neoprene-composite is imaged 50 feet above, which corresponds to 1.25mm in the laboratory set-up.

Figure 4-13 shows again the failure of the imaging by source multiples.

4.3.2 Synthetic data

The 24 synthetic time sections successfully image the structure as shown in figure 4-14, which is the sum of the 24 individual images. A slight artifact appears at the sharp corner of the fault. Diffractions from the fault corners are missing in the synthetic seismograms. But since diffractions image a point, the images do not really suffer from this omission.

4.4 General conclusion

4.4.1 Ultrasonic modeling

An important part of this work was devoted toward improving the water-tank ultrasonic modeling. The selection of the transducers, with proper characteristics and good choice of modeling materials have helped in acquiring the high-quality laboratory data. Subsequent improvement can be achieved. Specifically:

- The construction or use of a small-diameter thick disk type source transducer (ceramics are commercially available) featuring a natural frequency of 500Khz.
- The improvement of the tiny receiver hydrophone. The new model, which will be received after the completion of this thesis, is built according to recommendations suggested to the manufacturer. In particular, a smaller hydrophone body built with a material whose acoustic impedance is close to the water will reduce the body backscattering, improve the frequency response and make it more suitable for laboratory V.S.P experiments. A ceramic with a diameter of 1mm will increase its sensitivity above the threshold (calculated in appendix B) without deteriorating the directivity pattern in the frequency range of interest.
- The possible use of a point source pulsed laser to generate broad band omnidirectional ultrasound (Hutchins, 1988).
- A more complete study of the modeling material acoustic properties and of the construction of multi-layer models.

4.4.2 Ultrasonic experiments

High resolution are shown in the ultrasonic time sections. We show that simple laboratory reliable models can be built. This proves that it is desirable to deal with a complete wavefield obtained at a low expense, specifically when 3D acquisition is performed. For example, the post-critical reflection character (with the head wave) in the first model (chapter 3) and the converted waves in the second model provide valuable features to interpret the seismograms. Some minor disadvantages, such as the transducer backscattering, are given evidence. There are only a few additional steps required before doing reliable 3D solid ultrasonic data acquisition.

4.4.3 Water-multiple imaging

The receiver multiple imaging technique has demonstrated its efficiency. It has clearly demonstrated the extension of the lateral image, either in the reflector of the first model (chapter 3) or in the upper corner of the fault in the second model. These show clearly how, on a O.B.H or a water-bottom streamer, the receiver multiple migration improves the image over the migration of primary reflections alone.

Experiment model 2 - Geometry

Front view

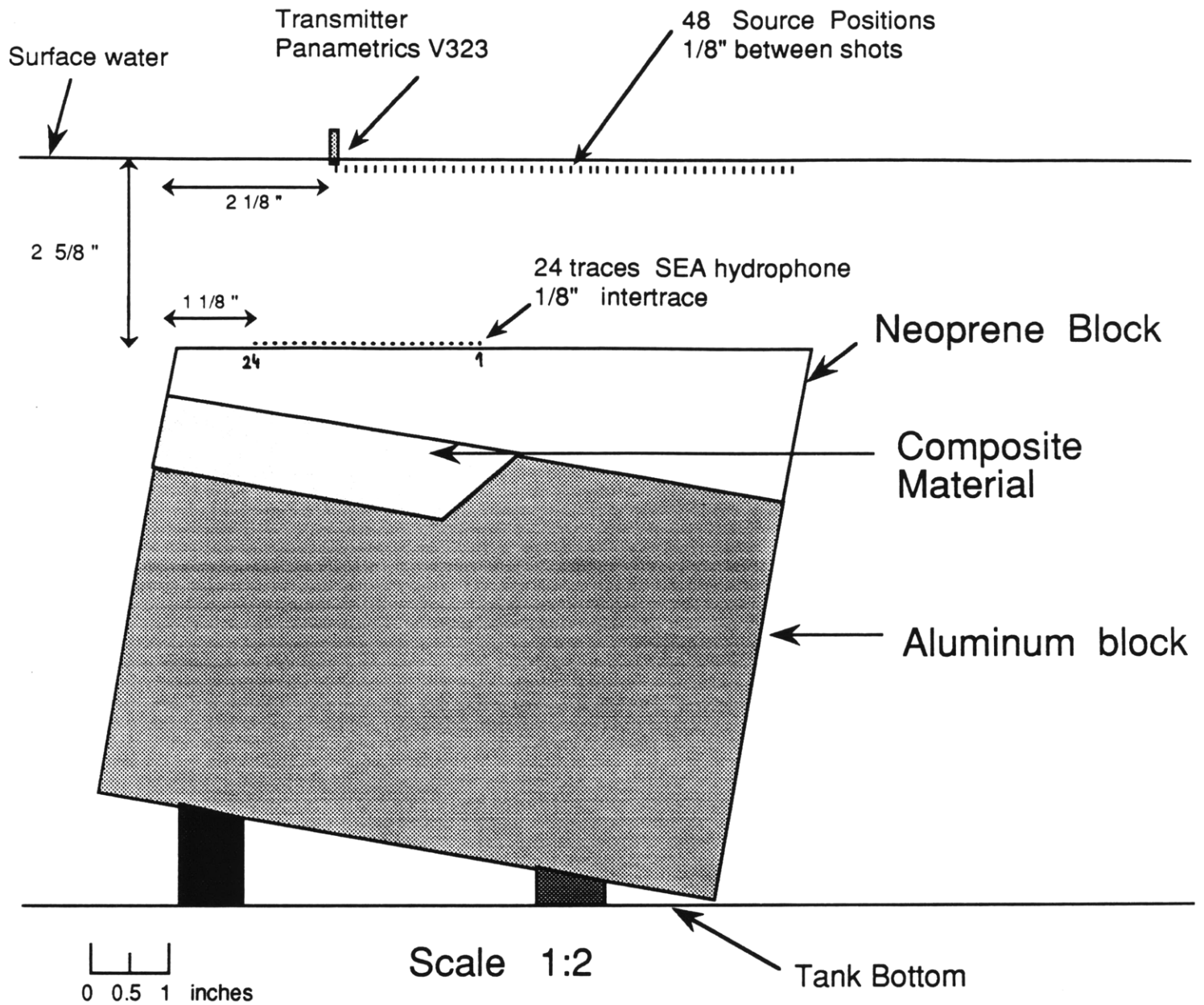


Figure 4-1: Model 2 used in the ultrasonic acquisition

Synthetic model 2

2D profile

Scale factor used : 12000

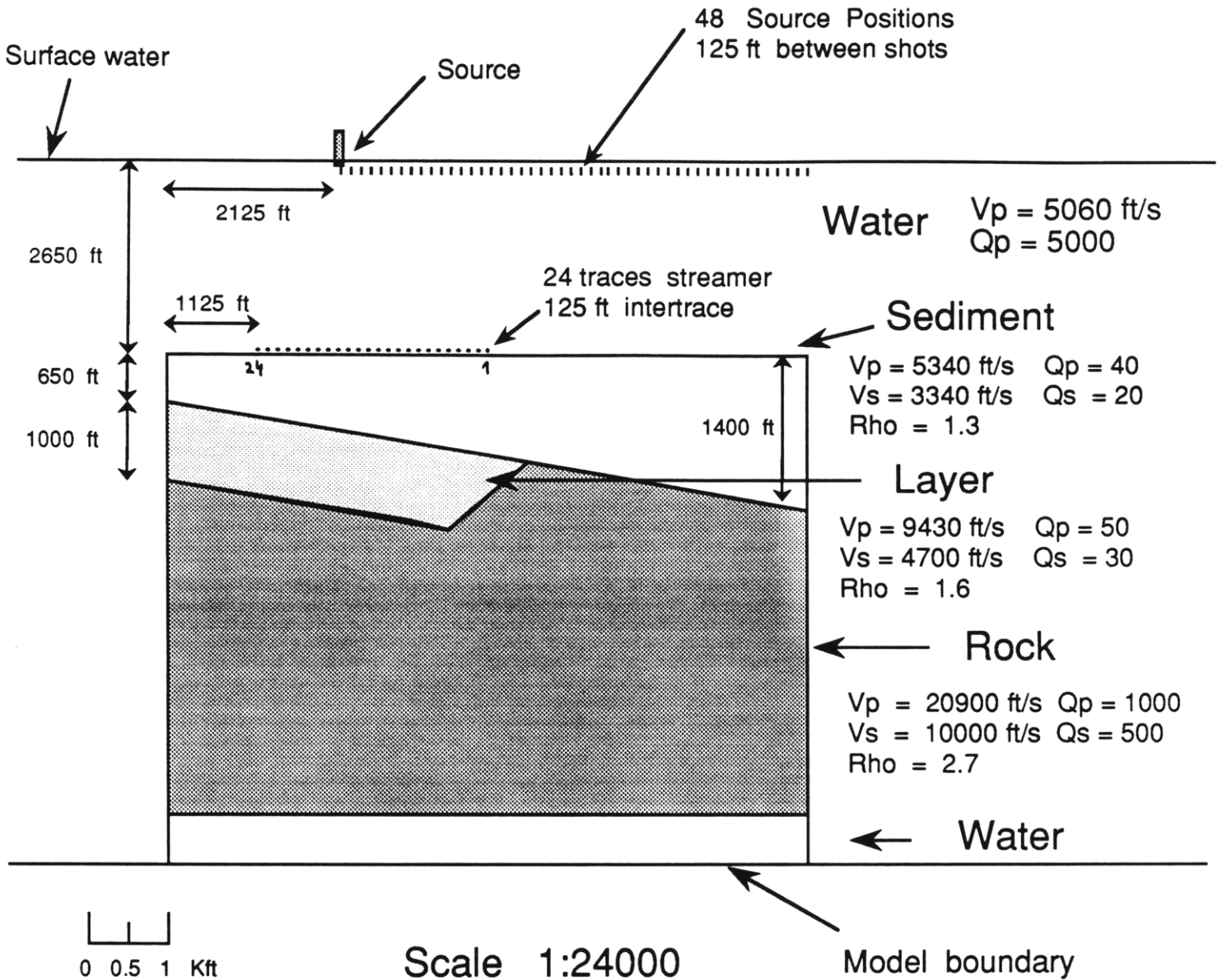


Figure 4-2: Synthetic model

Model No 2

Fault - Unconformity 3 layers model

Parameters	Ultrasonic experiment	Marine acquisition
Dimension of the model	8*8*5 inches	9600*9600*6000 feet
Spatial sampling	1/8 inch	125 feet
Time sampling	400 nanosec	4.8 millisec
High cut-off frequency	400 Khz	48 Hz
Low cut-off frequency	50 Khz	6 Hz
Record length	200 microsec	2.4 sec

Scaling factor 12000

Figure 4-3: Scaled parameters

Fault-unconformity Model No 1

3D model experiment No 2

- **Geometry :**

Source line : X

Source intertrace : 1/8"

Nb of source points : 48

Receiver line : X

Receiver intertrace :

Nb of receiver points : 24

- **Source parameters :**

Transmitter : Panamatrix V323

Pulser : Panamatrix 5052PR

Energy setting : 3

Damping setting : 0

- **Receiver parameters :**

Receiver transducer : Miniature Hydrophone SEA

Preamplifier(s) : SEA + Panamatrix 5660B

Total gain in db : 77 db

Bandpass filter : Krohn-Hite 3202R

Low cut-off frequency : 50 Khz + AC on acquisition

High cut-off frequency : 400 Khz - Max flat -

- **Acquisition parameters :**

Acquisition unit : Ampli D1000 + Oscillo D6000

Time sampling : 400 nanosec

Time delay : 50 microsec

Number of points acquired : 512

Resolution : 12 bits companded

Y full-scale : 1.4 Volts

Y scale amplification : 2

Averaging : 64

Figure 4-4: Acquisition parameters

RAW DATA TIME SECTIONS

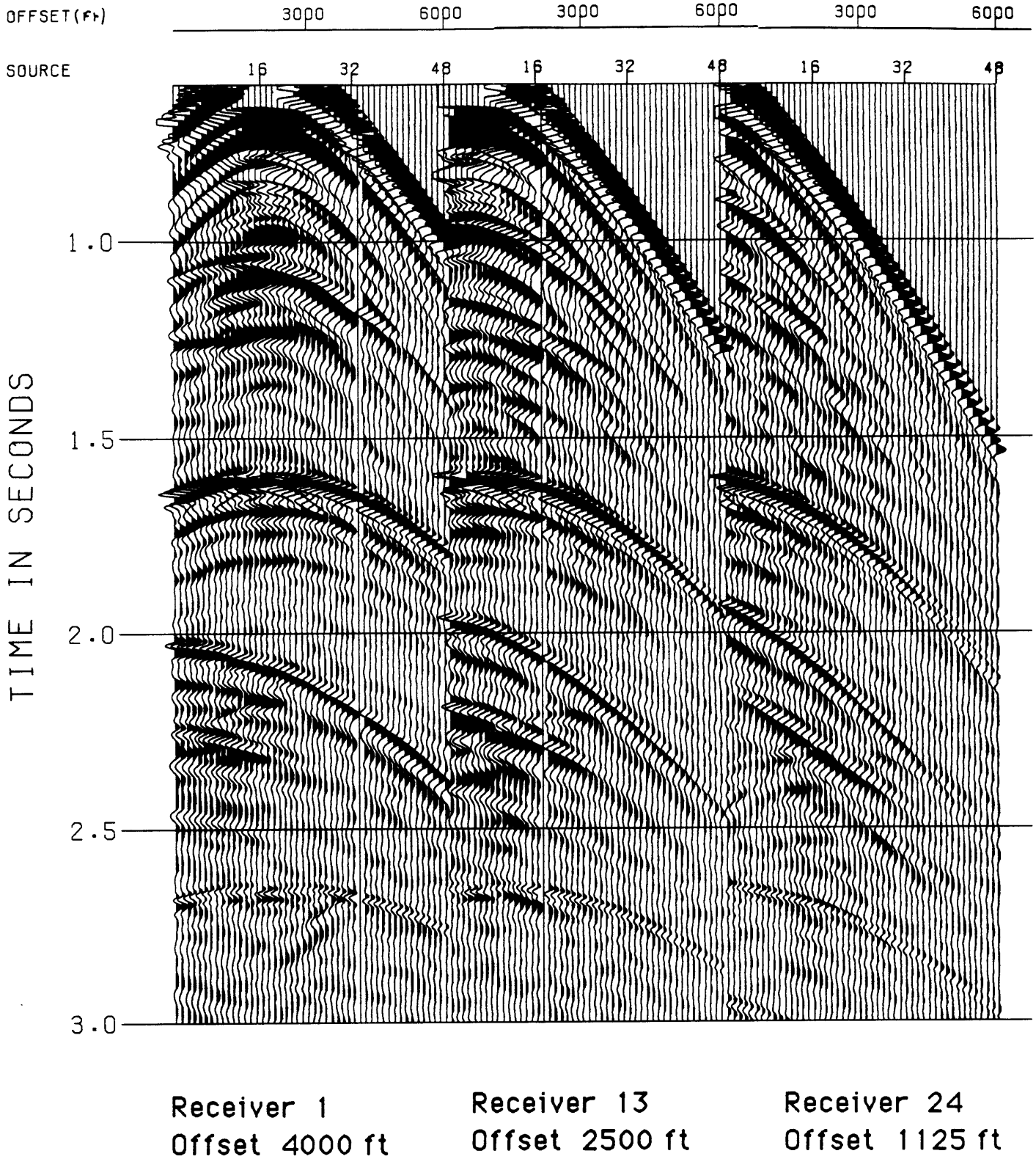


Figure 4-5: (a) Ultrasonic raw data time section. The receiver points 1,13 and 24 are plotted.

DECONVOLVED RAW DATA TIME SECTION

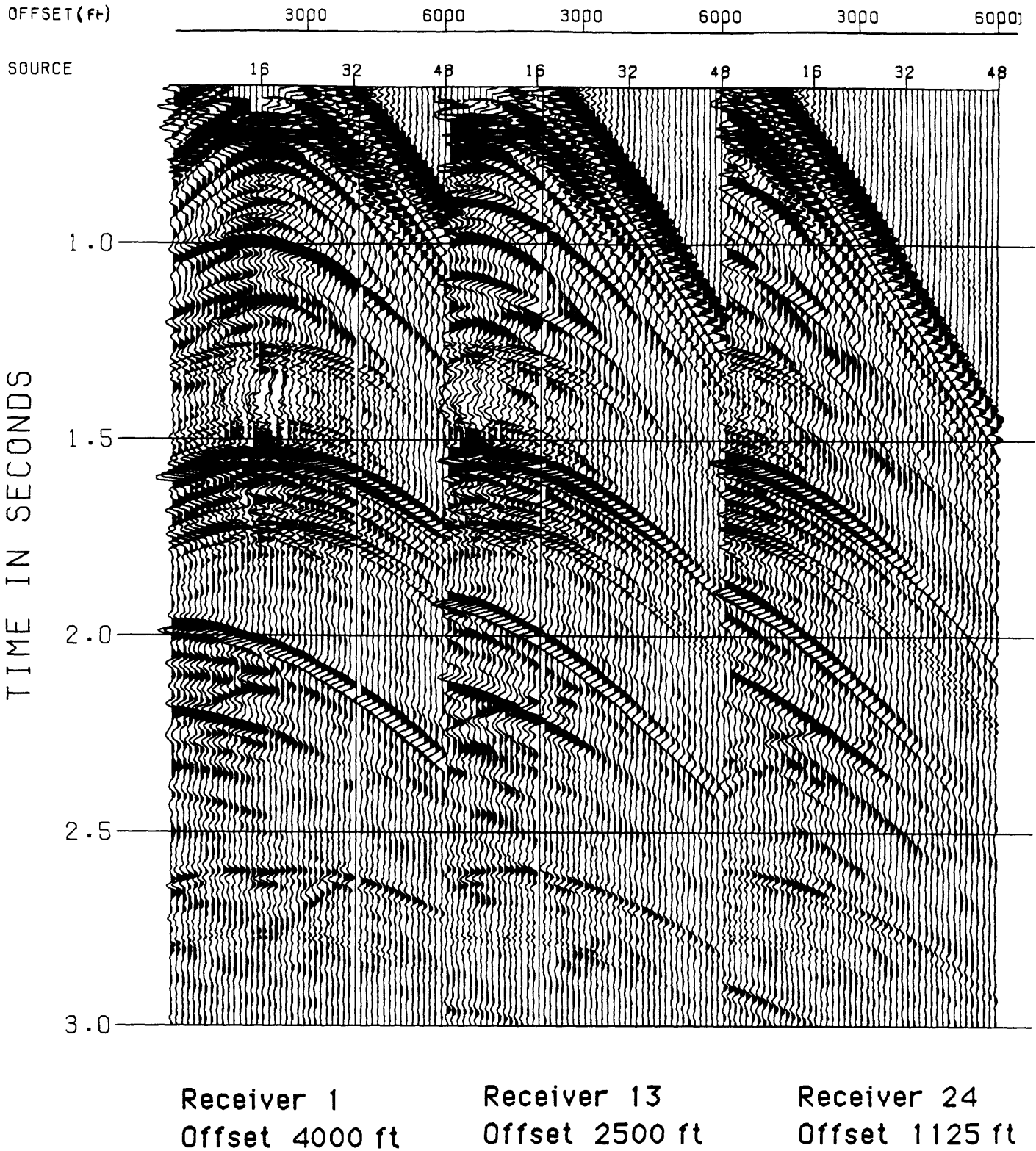
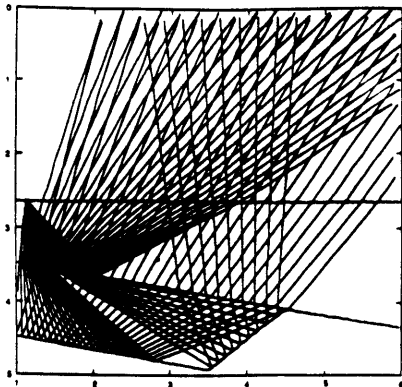


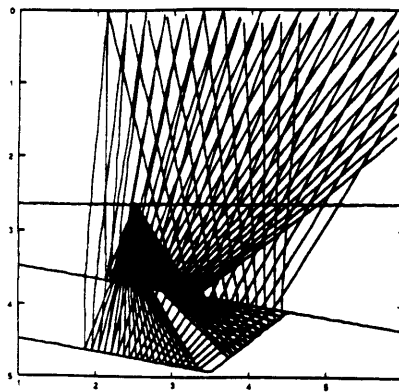
Figure 4-5: (b) Ultrasonic deconvolved time section. The receiver points 1,13 and 24 are plotted.

COVERAGE OF THE INTERFACES

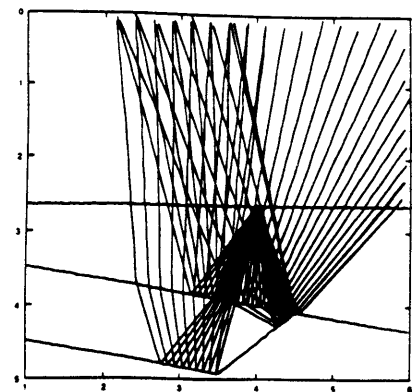
Receiver 24
Offset 1125 ft



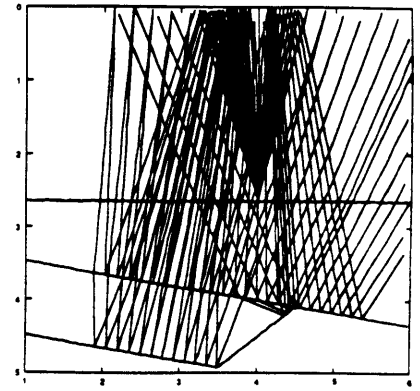
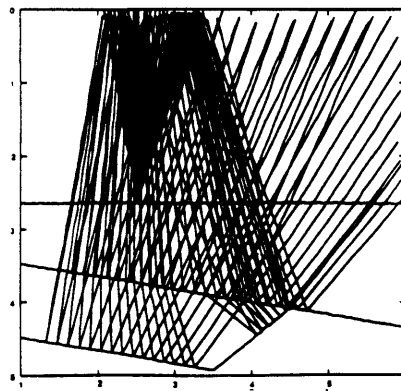
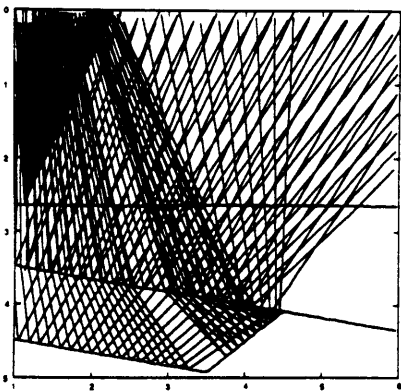
Receiver 13
Offset 2500 ft



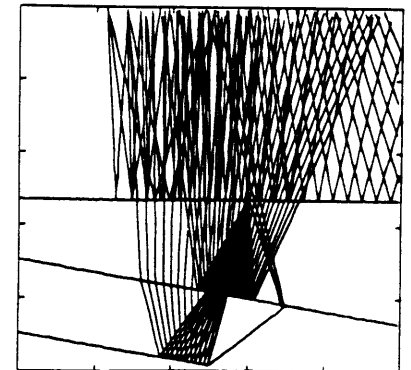
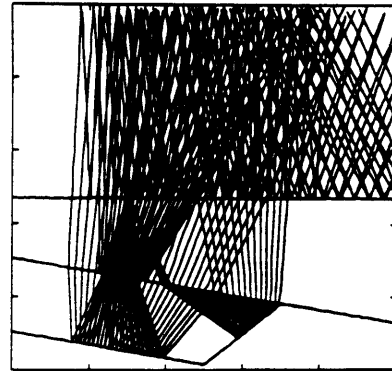
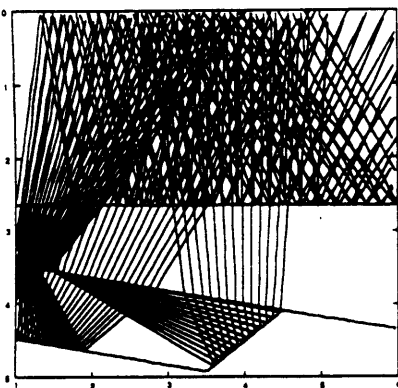
Receiver 1
Offset 4000 ft



PRIMARY RAYS



RECEIVER MULTIPLE RAYS



SOURCE MULTIPLE RAYS

Figure 4-6: Coverage of the interfaces for the three primary, receiver multiple and source multiple.

SYNTHETIC DATA TIME SECTIONS

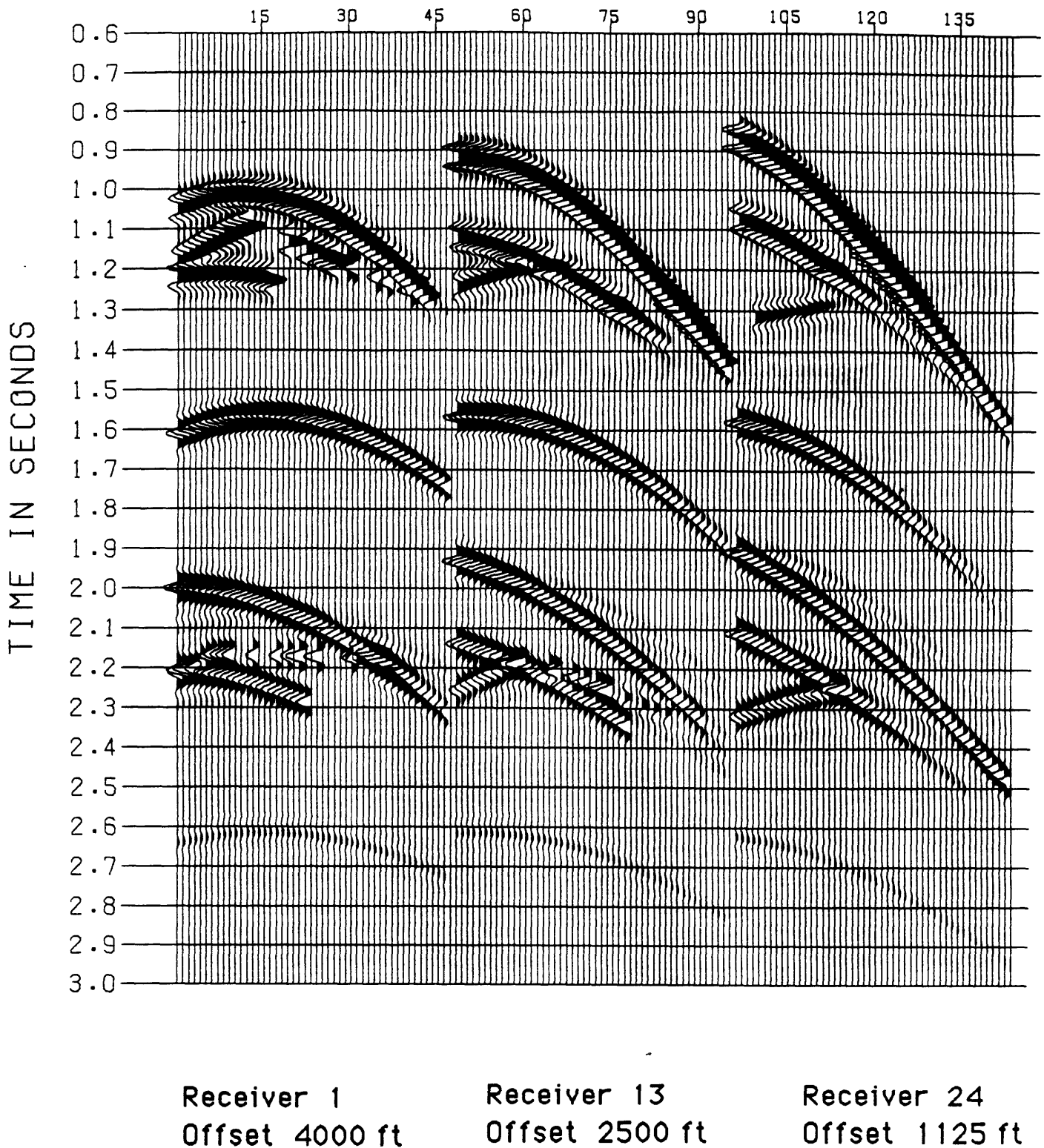
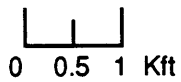
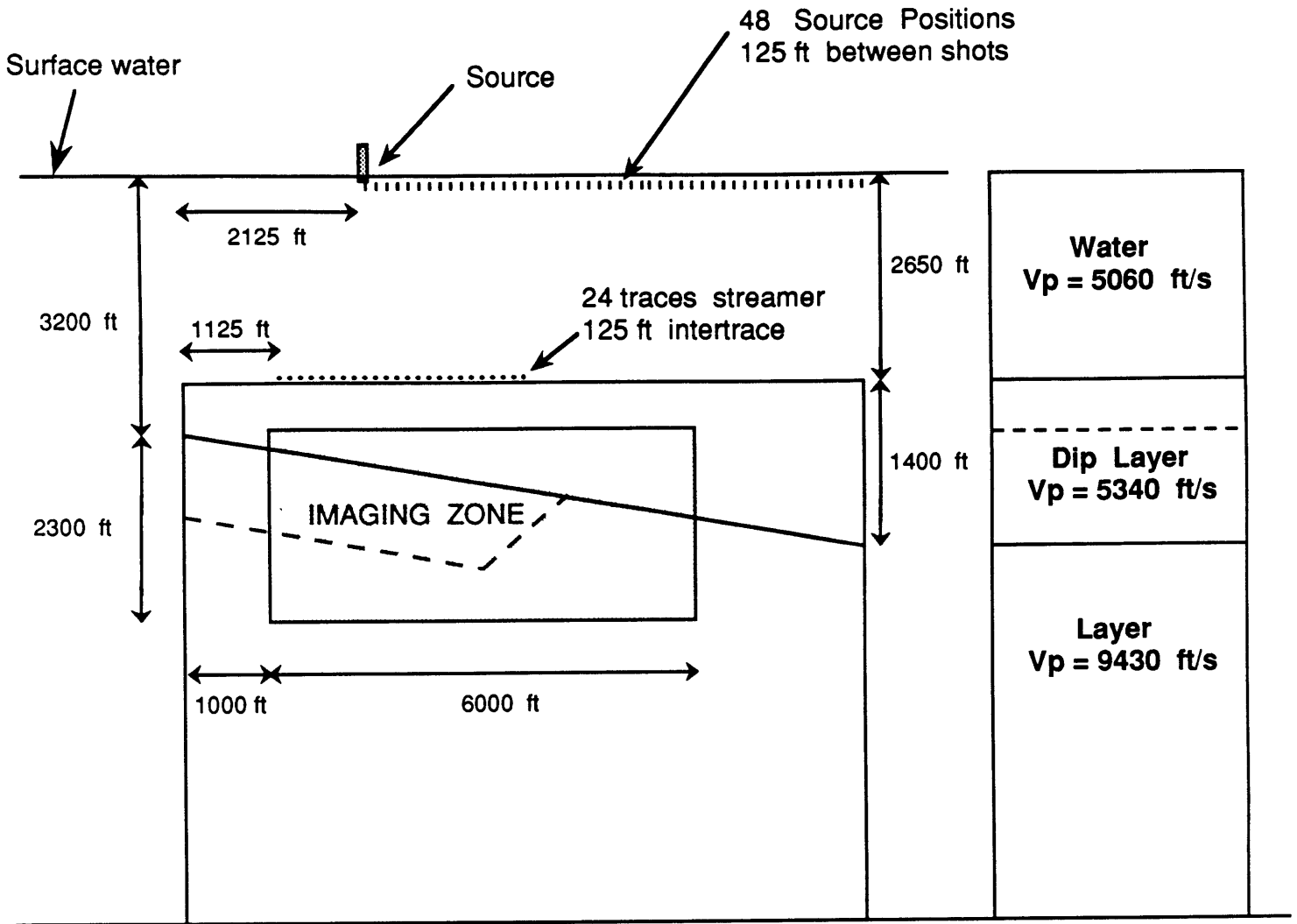


Figure 4-7: Partial synthetic time section. The receiver points 1,13 and 24 are plotted.

Imaging zone - model 2

2D profile

Scale factor used : 12000



Scale 1:24000

Figure 4-8: Imaging zone

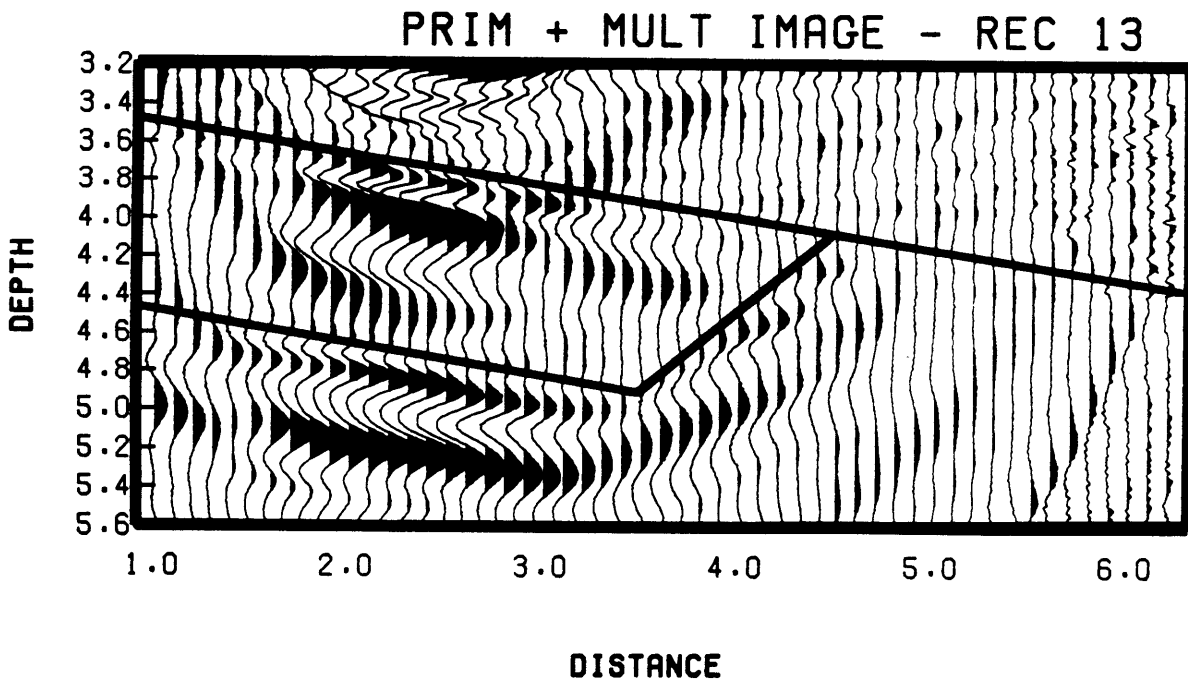
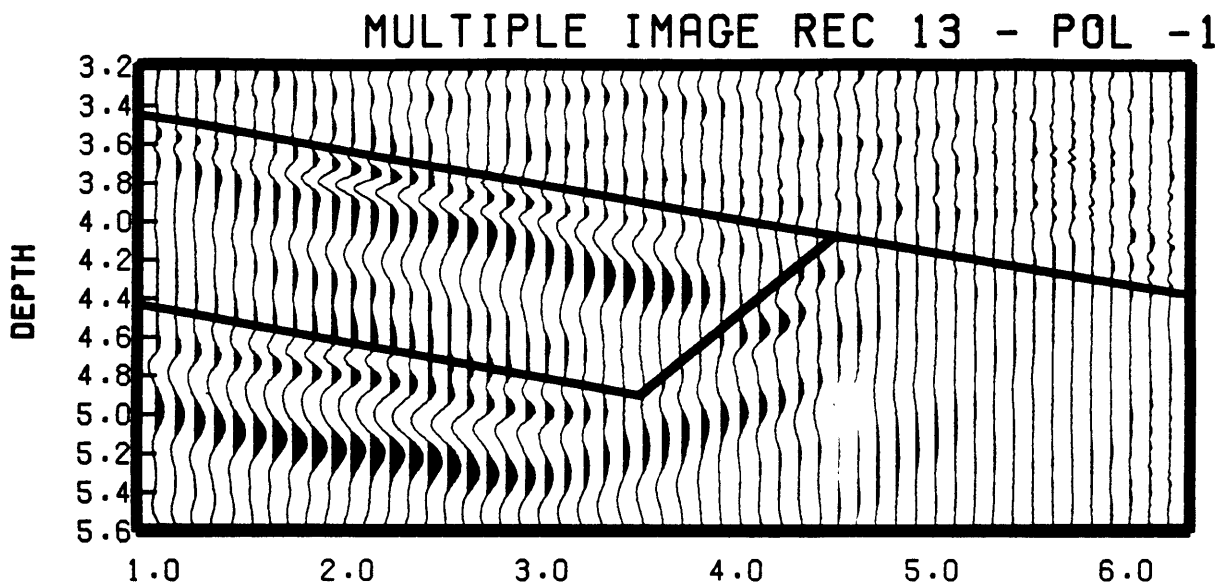
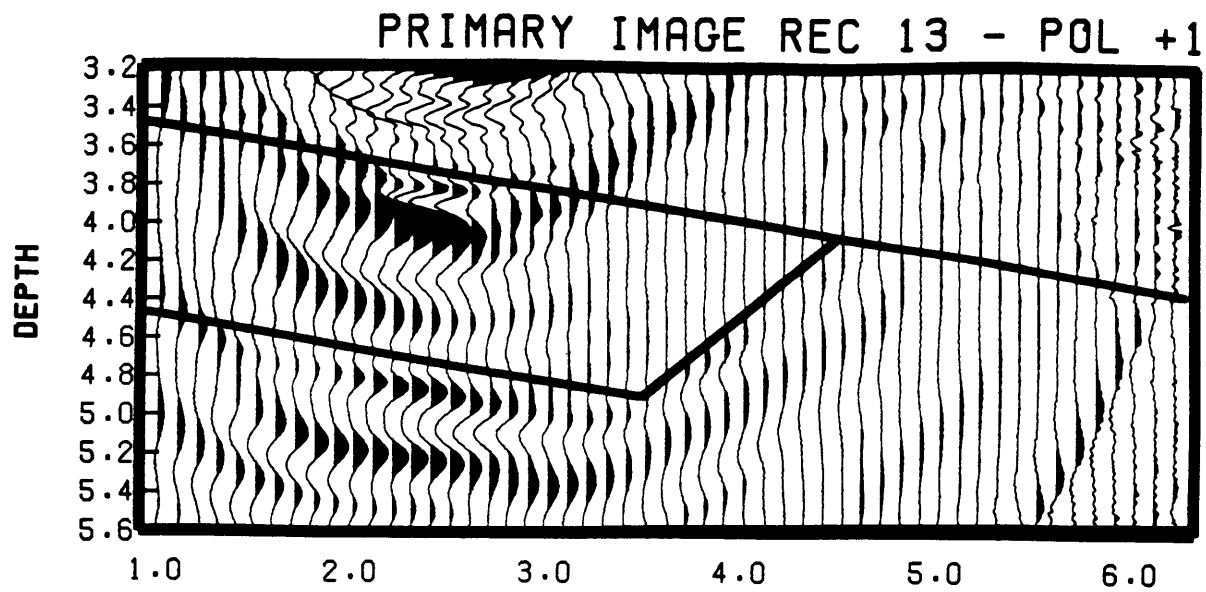


Figure 4-9: (a) Migration from the raw data time section for the receiver 13. Primary, receiver multiple and composite image.

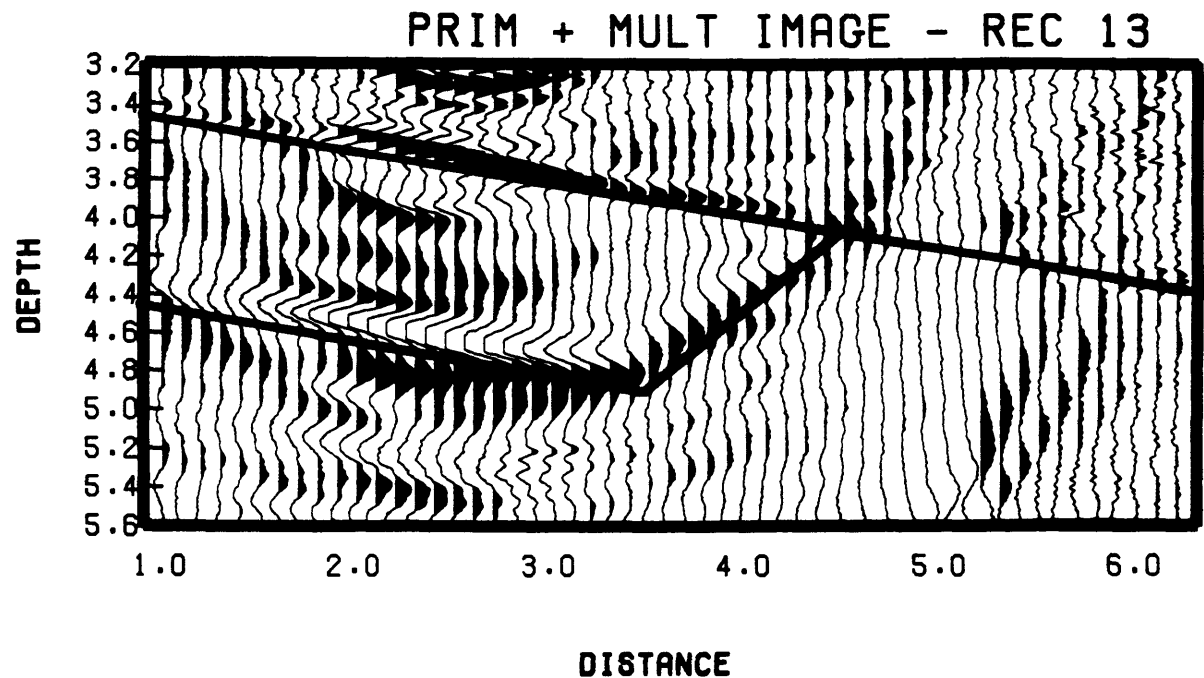
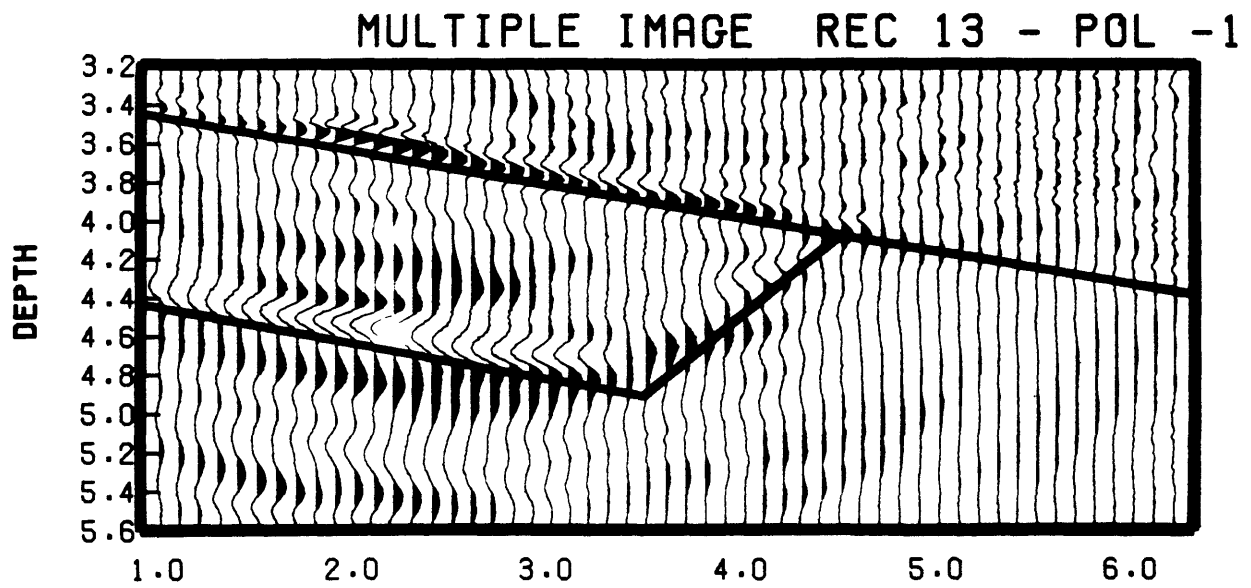
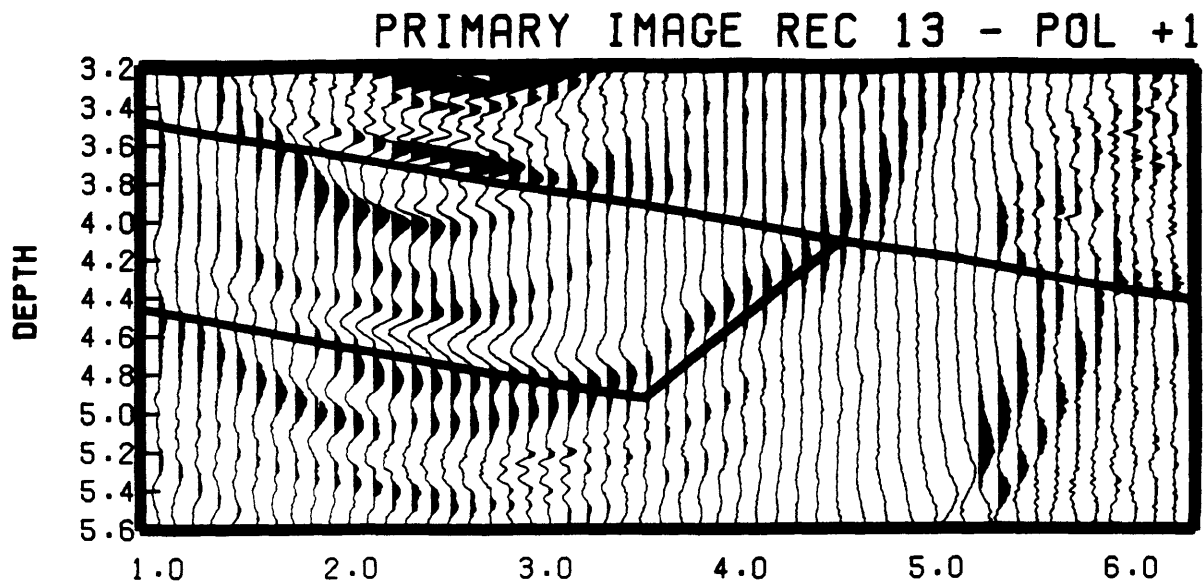
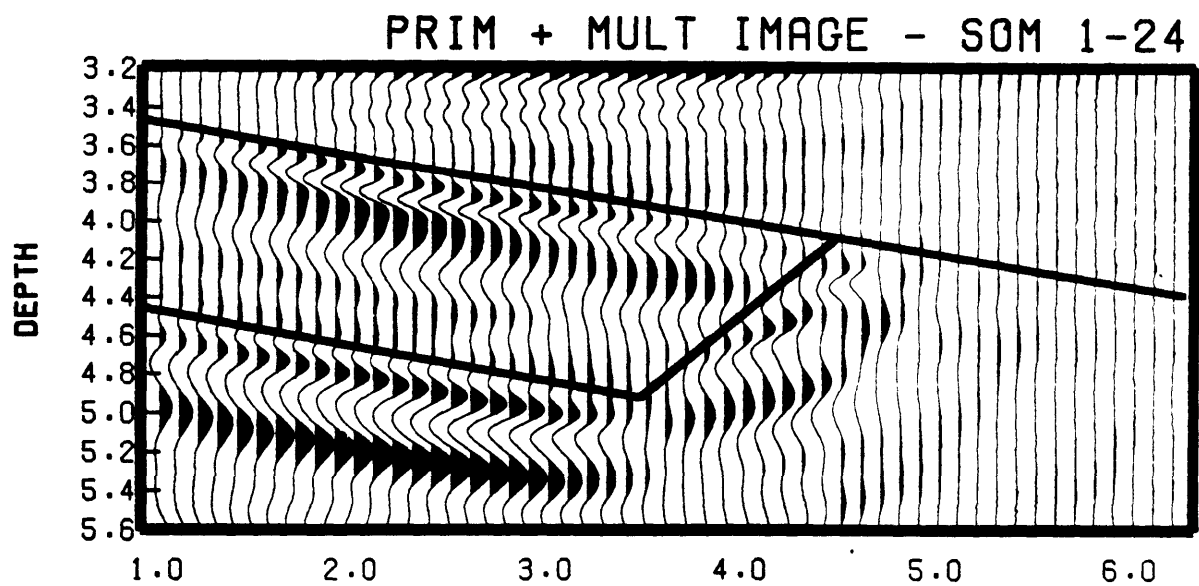
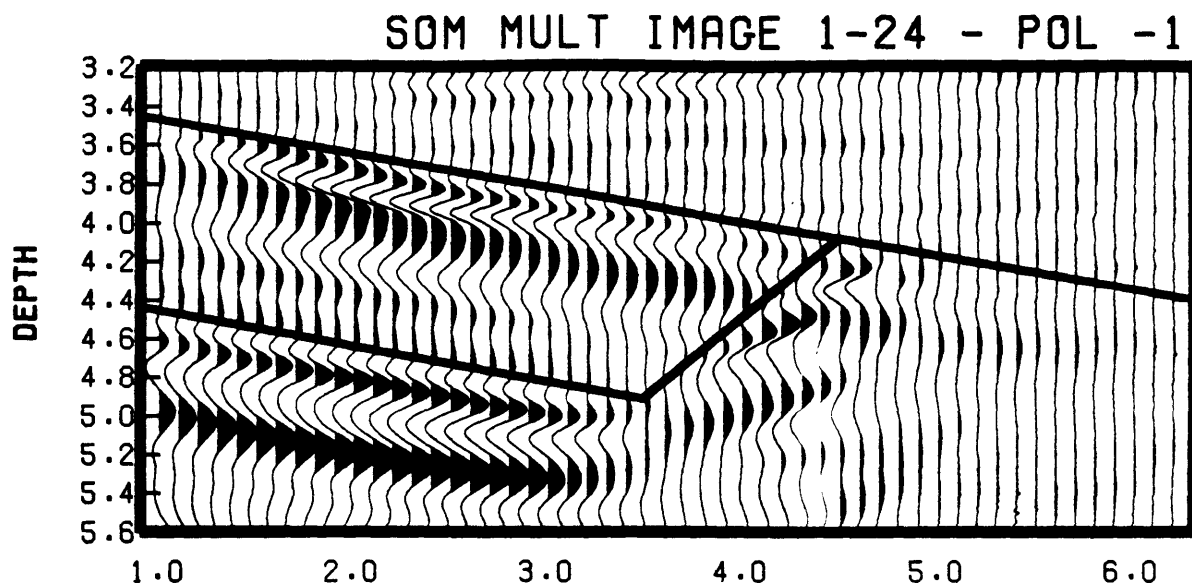
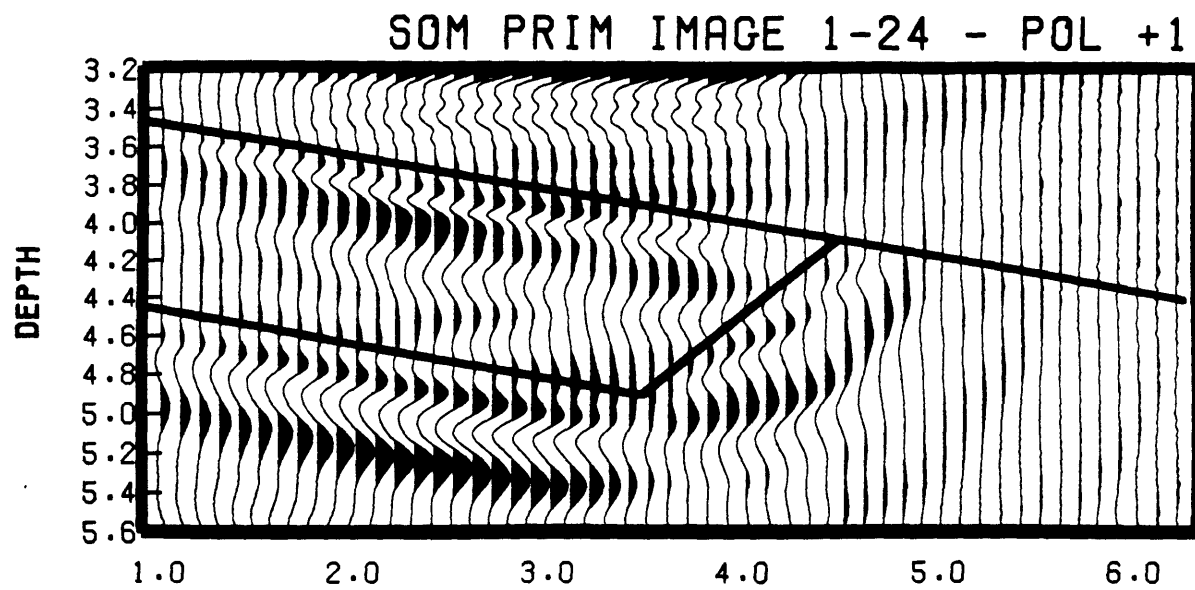


Figure 4-9: (b) Migration from the deconvolved time section for the receiver 13. Primary, receiver multiple and composite image.



DISTANCE

Figure 4-10: (a) Migration from the raw data time sections. Sum of the 24 receivers images.

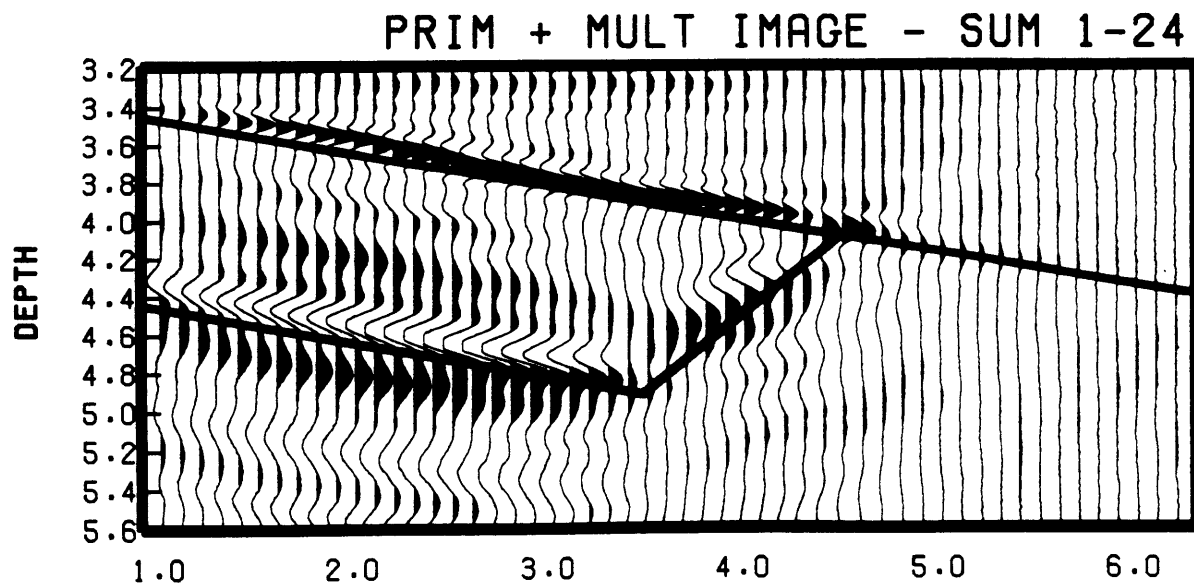
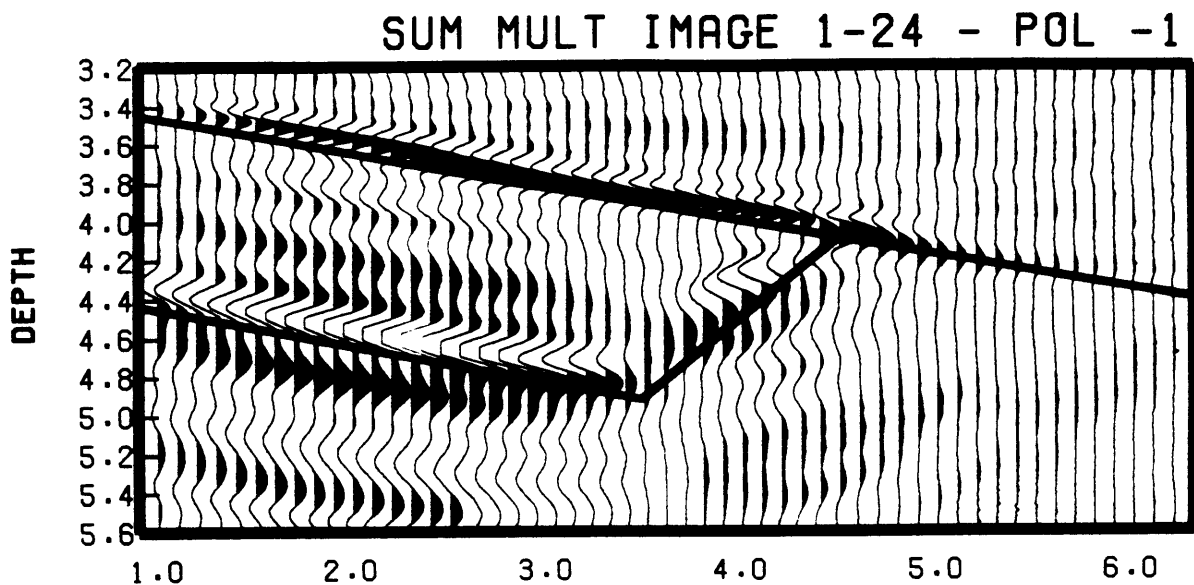
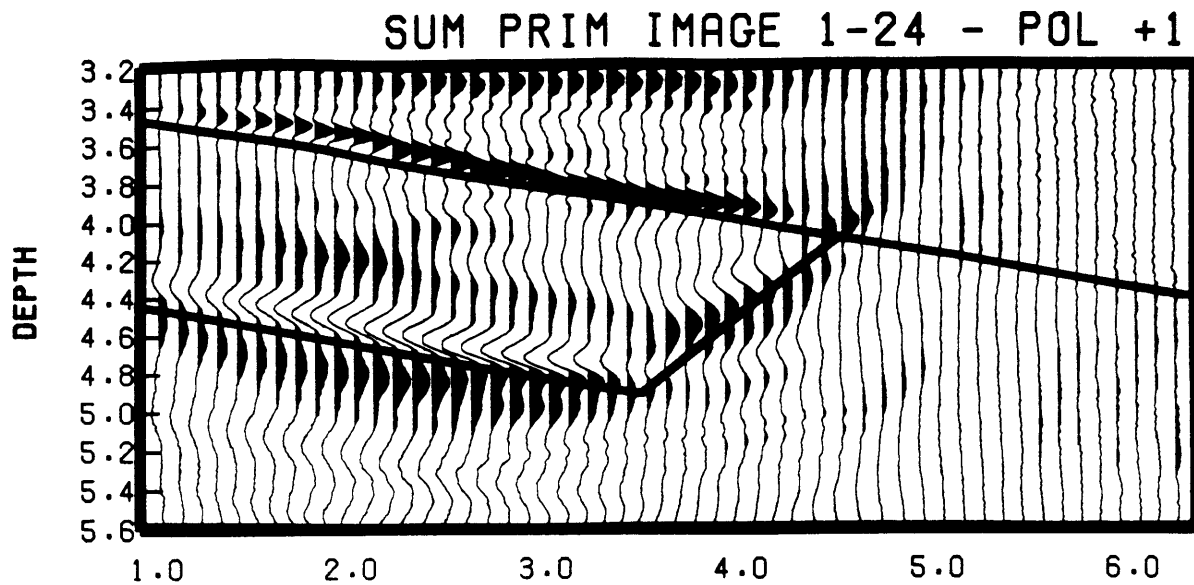


Figure 4-10: (b) Migration from the deconvolved time sections. Sum of the 24 receivers images.

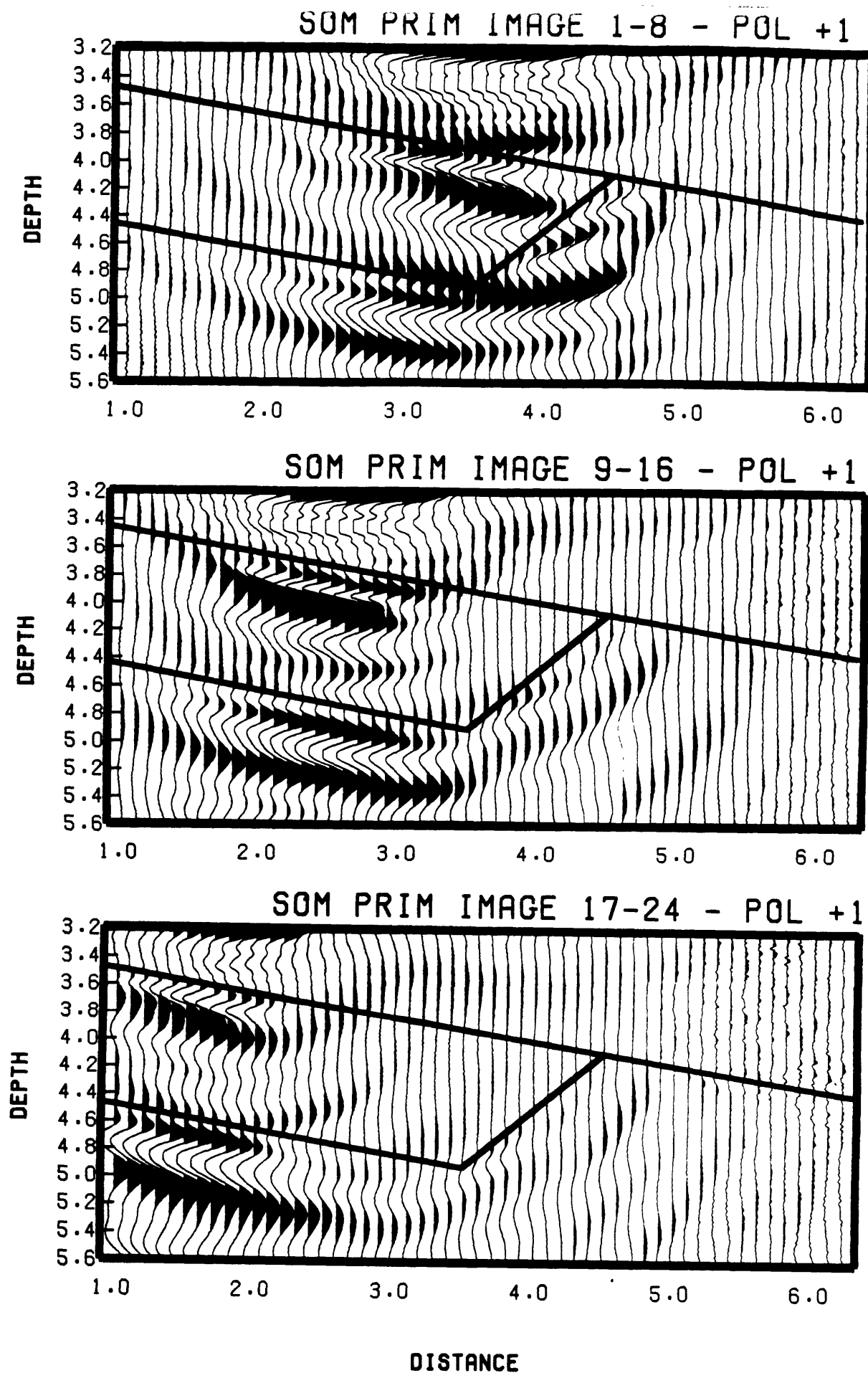


Figure 4-11: (a) Migration from the raw data time sections. Primary images. 3 set are plotted which corresponds to the sum of eight successive receiver points.

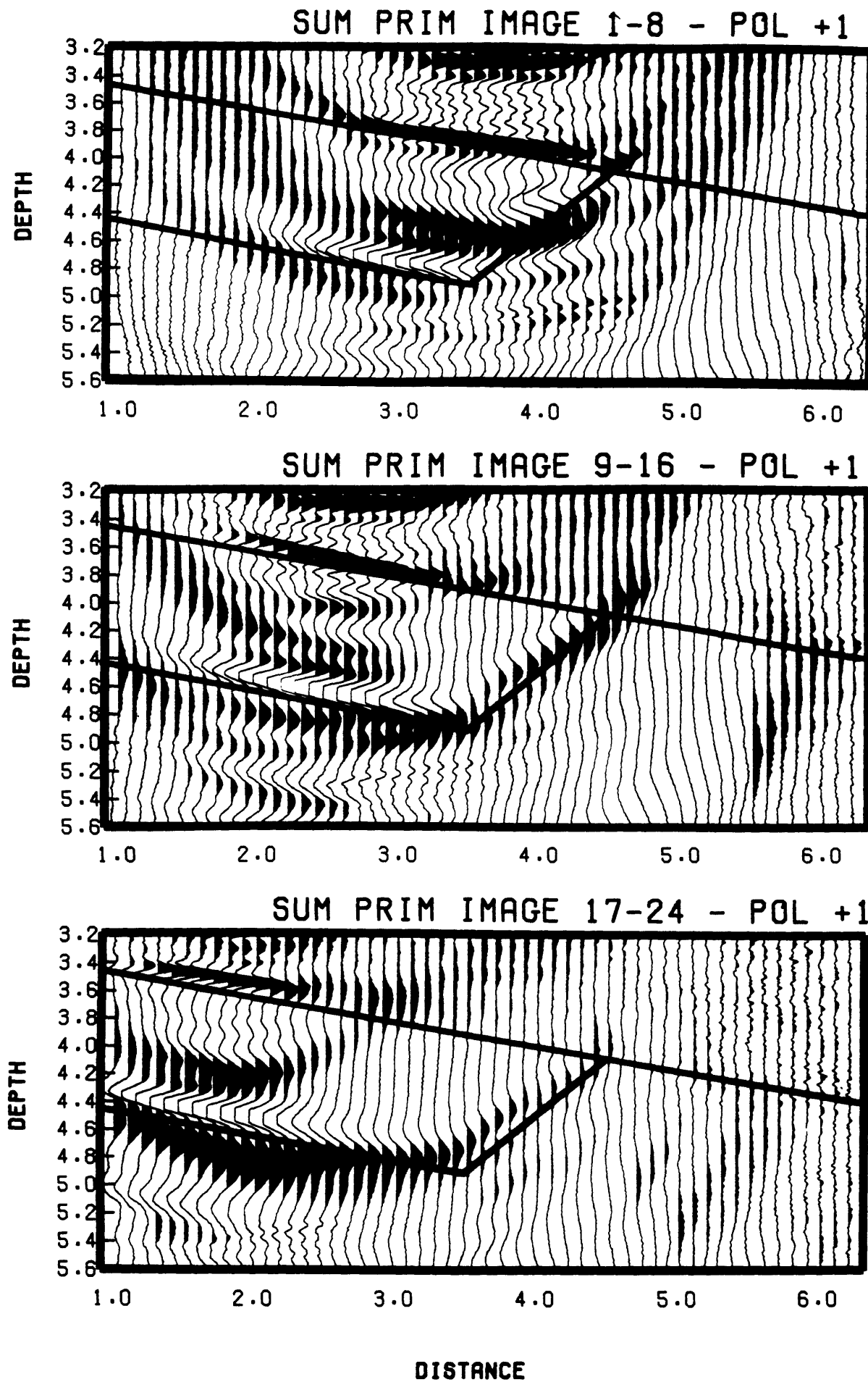


Figure 4-11: (b) Migration from the deconvolved time sections. Primary images. 3 set are plotted which corresponds to the sum of eight successive receiver points.

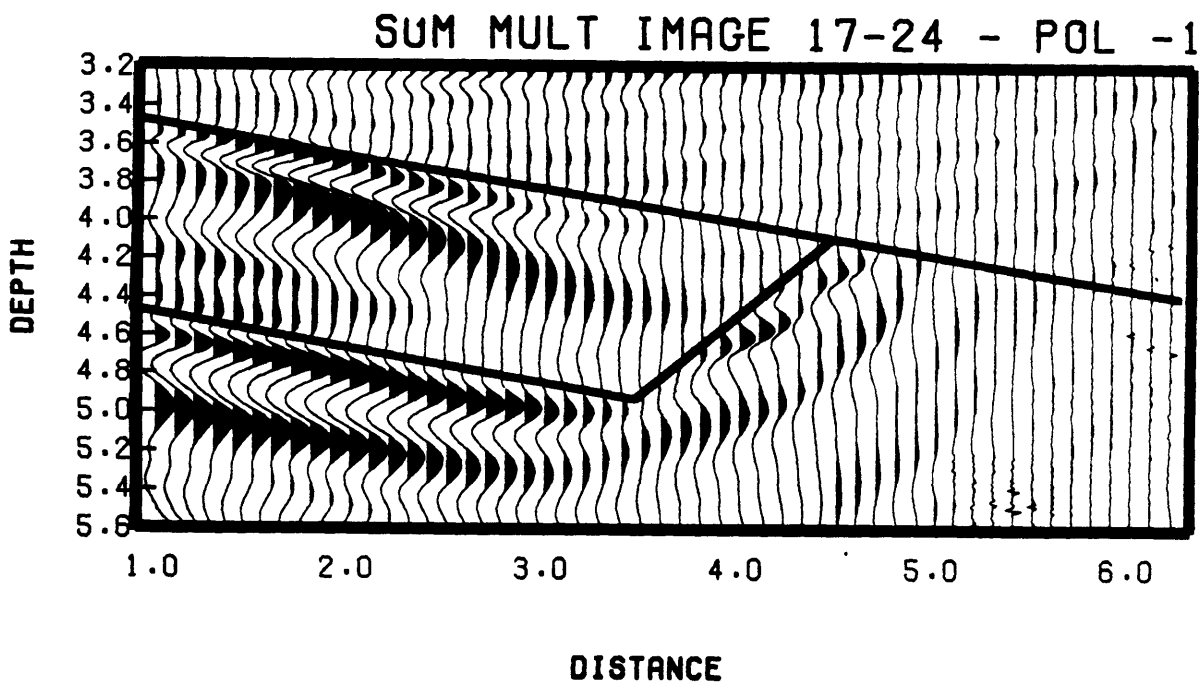
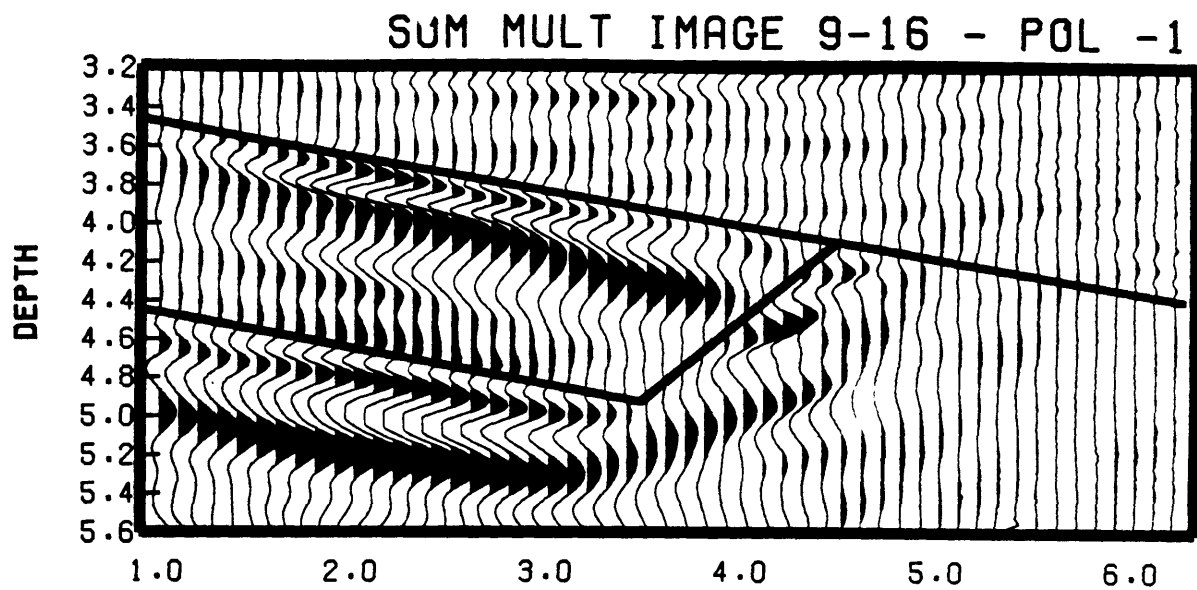
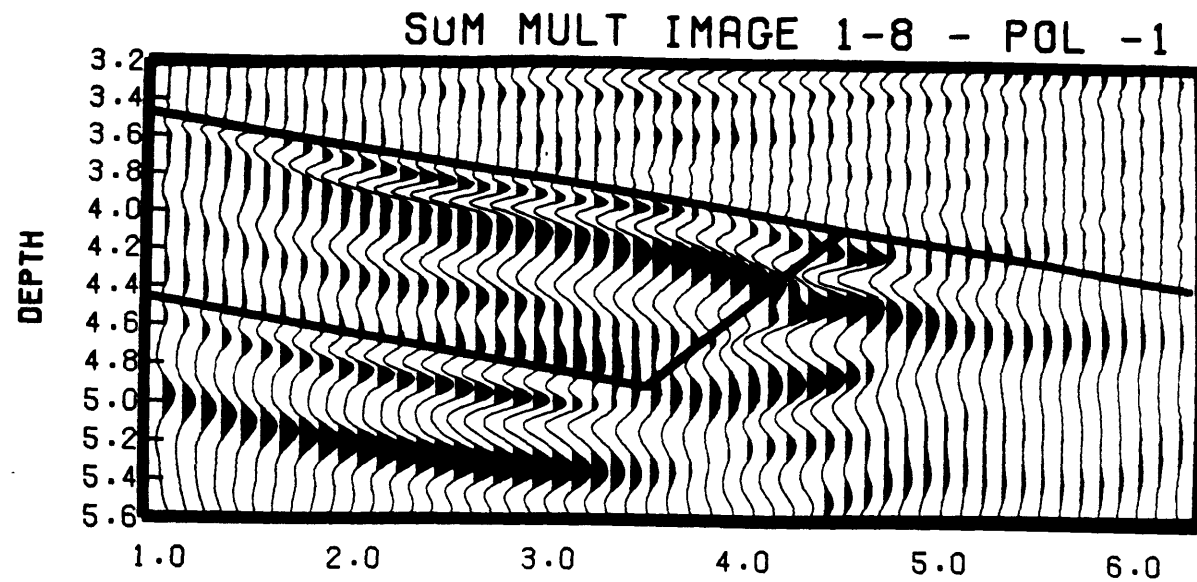


Figure 4-12: (a) Migration from the raw data time sections. Receiver multiple images. 3 set are plotted which corresponds to the sum of eight successive receiver points.

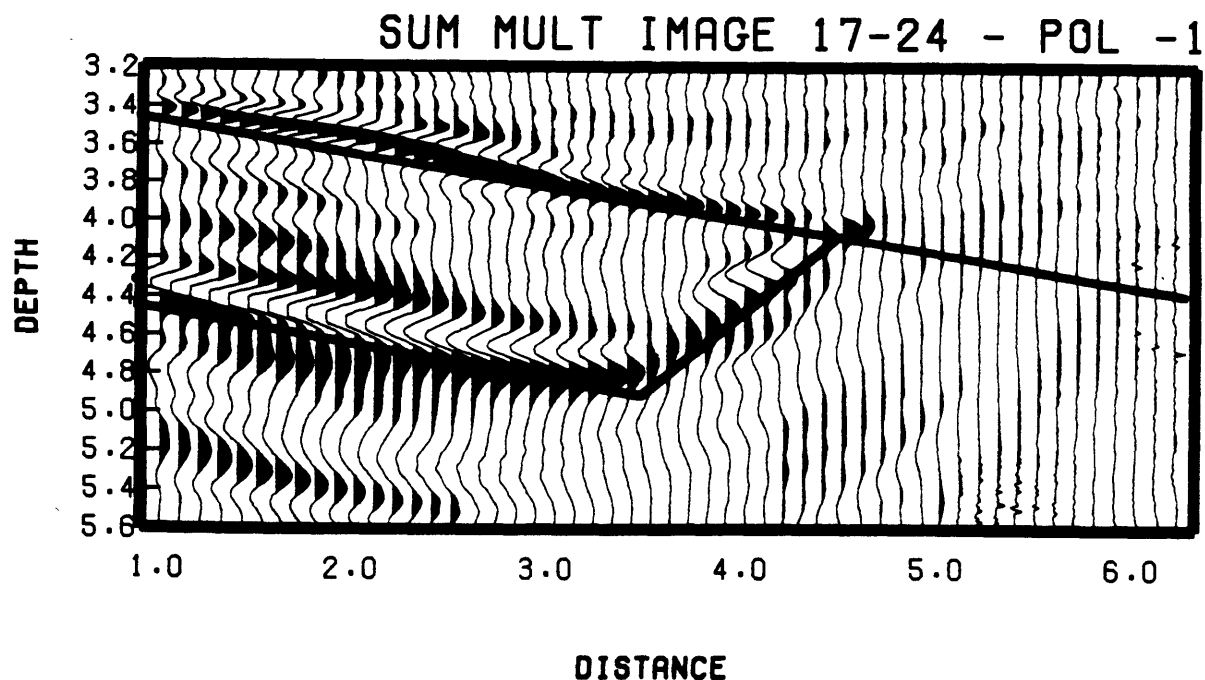
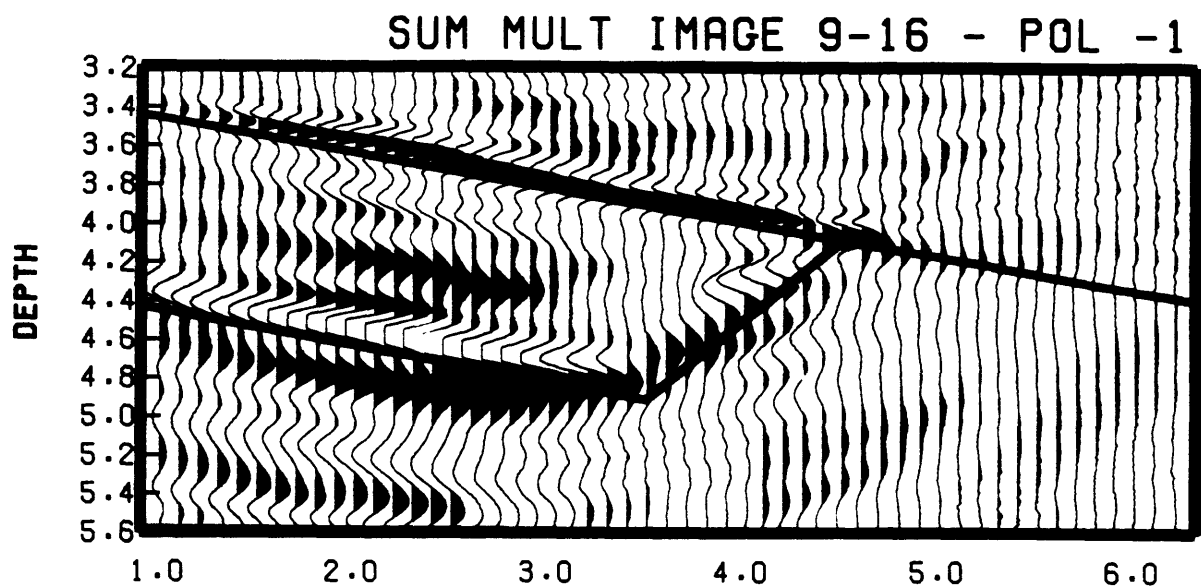
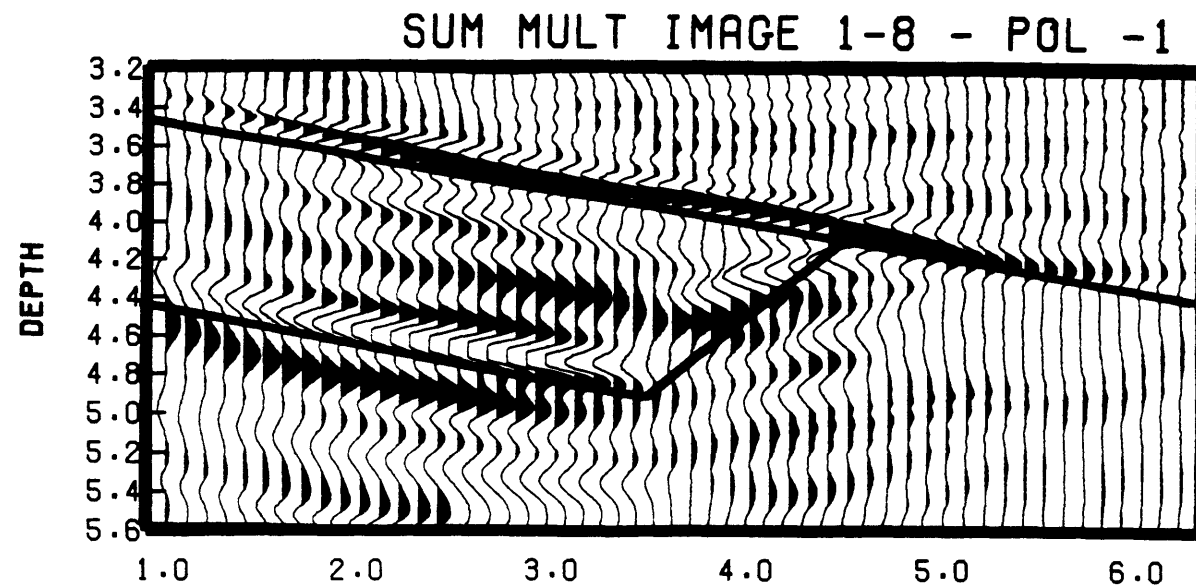


Figure 4-12: (b) Migration from the deconvolved time sections. Receiver multiple images. 3 set are plotted which corresponds to the sum of eight successive receiver points.

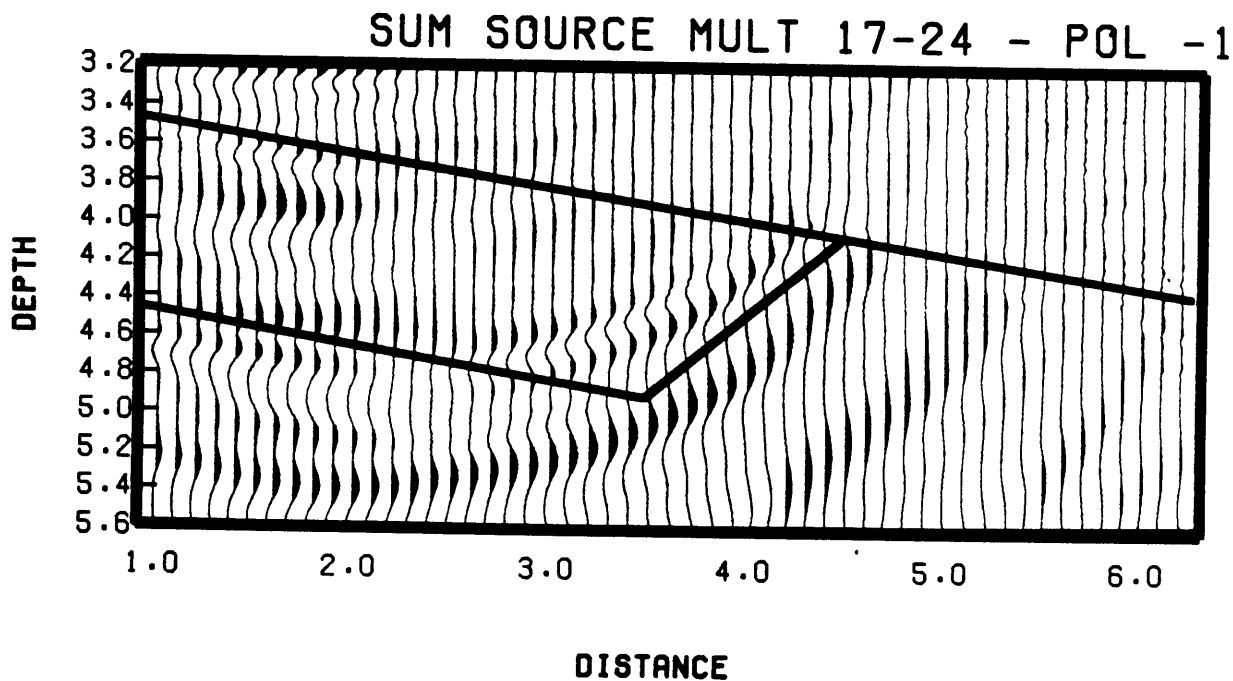
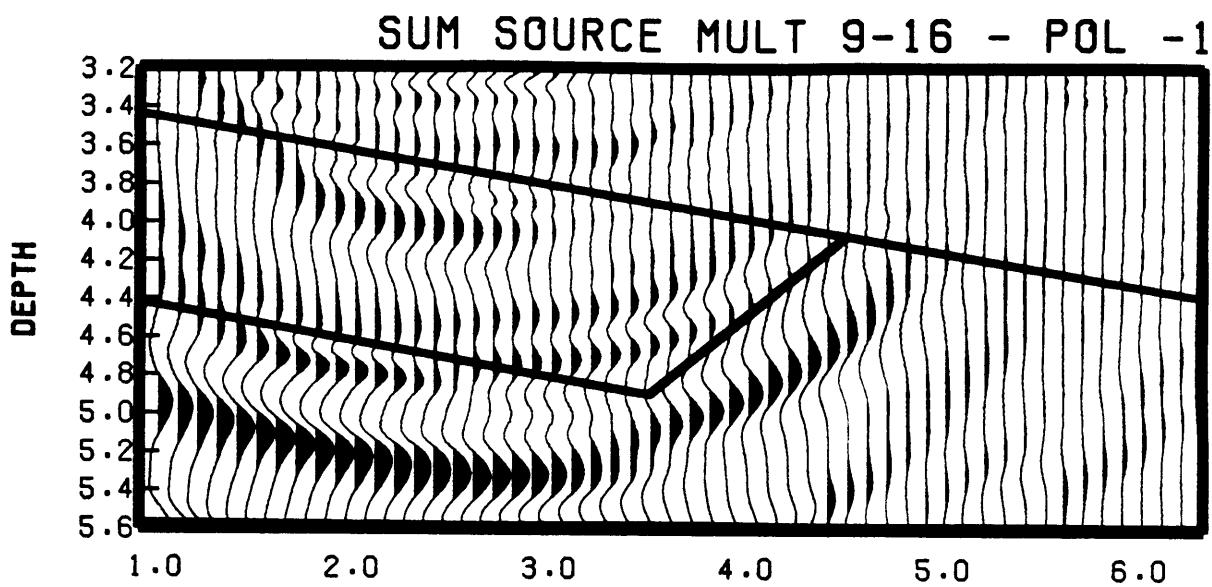
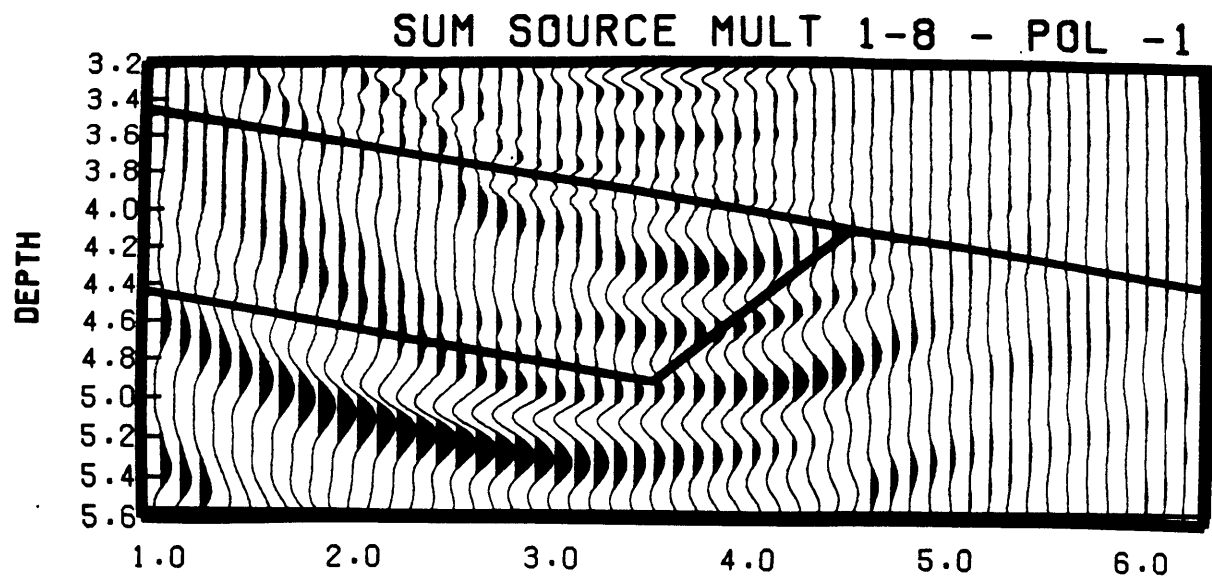


Figure 4-13: Migration from the raw data time sections. Source multiple images. 3 set are plotted which corresponds to the sum of eight successive receiver points.

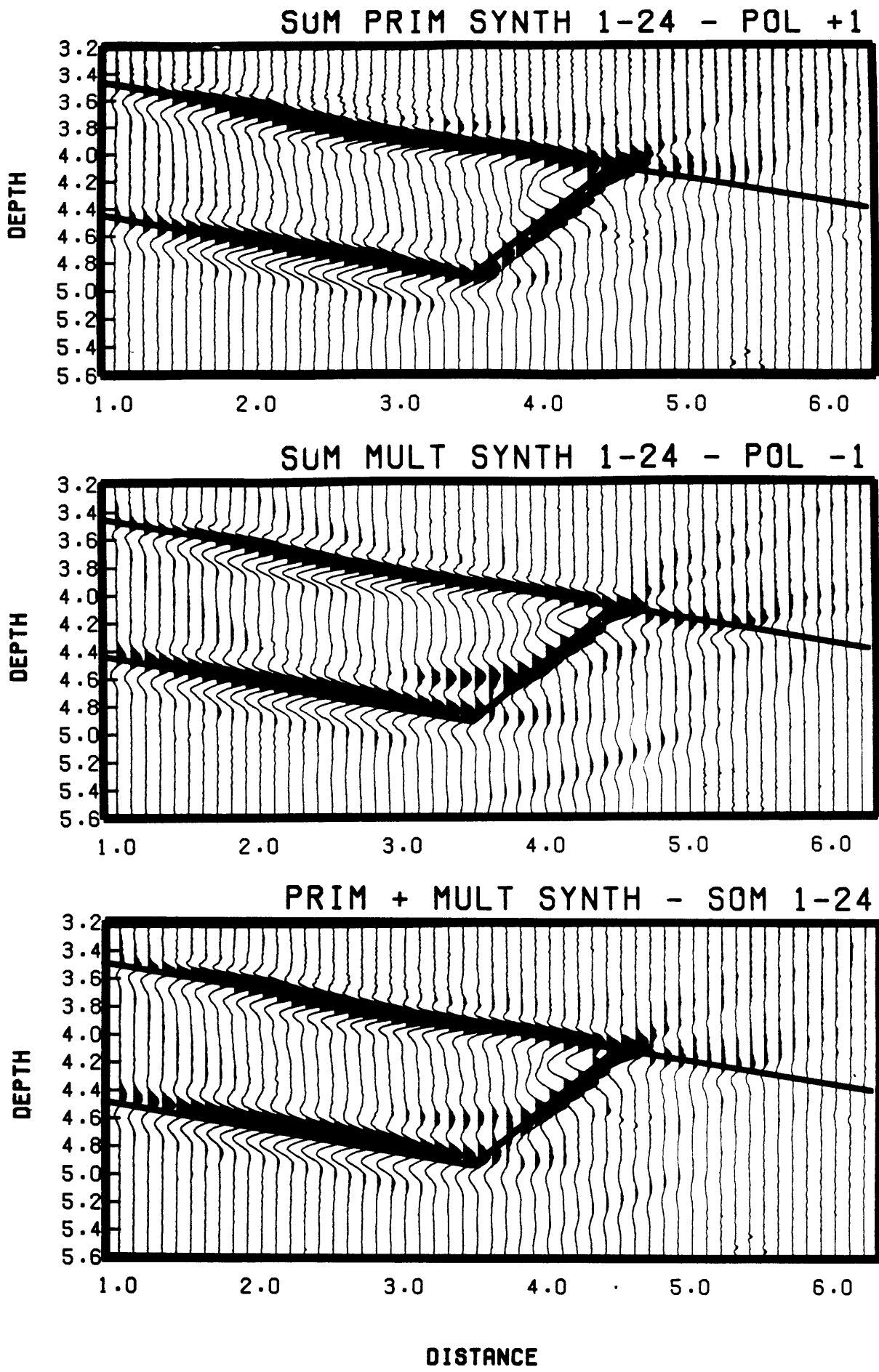


Figure 4-14: Synthetic images. The sum of the 24 receivers points are plotted for the primary, receiver multiple and composite images.

Appendix A

Piezoelectricity and transducer applications

A transducer is a device which converts a certain form of energy into another one. Transducers are usually reversible. In ultrasonics, mechanical and electrical energy are involved. Piezoelectricity is one way to achieve this transformation. Let us first give the following definition because of some confusing uses:

Piezoelectricity : Property of a crystal to develop an electric charge or polarisation field proportional to a mechanical stress. This feature is known as the direct piezoelectric effect. The converse piezoelectric effect is the proportional strain change when subjected to an applied electric field.

Electrostriction : The deformation produced by an electric field is *independent* of the polarity of the field.

Ferroelectricity : The crystal has an internal dipole moment even in the absence of an electric field. This dipole tends to align itself in an allowed direction closest to an applied field.

Pyroelectricity : An electric charge is developed proportional to temperature when the material is heated.

All ferroelectric and pyroelectric crystals are piezoelectric. The two basic equations of state for piezoelectric materials are the following:

Direct effect :

$$D_i = d_{ij}T_j + \varepsilon_{il}E_l \quad (\text{A.1})$$

Converse effect :

$$S_m = d_{lm}E_l + s_{mj}T_j \quad (\text{A.2})$$

Where:

$D[3,1]$ is the electric displacement (directly related to electric charges)

$E[3,1]$ is the electric field

$T[6,1]$ is the stress tensor

$S[6,1]$ is the strain tensor

$d[3,6]$ is the piezoelectric constant tensor in Coul/Newton or in m/V

$s[6,6]$ is the elastic stiffness tensor, derived here for *E constant*

$\varepsilon[3,3]$ is the dielectric tensor, derived here for *T constant*

The piezoelectric efficiency depends on the high value of the dielectric and piezoelectric constants. Consequently, ceramics such as Lead-Zirconate-Titanium (PZT) or Lead-Metaniobate are the piezoelectric materials mainly used in the transducer design. On the grounds that genuine zones of polarisation are randomly distributed in the polycrystalline ceramic, a preliminary process called "poling" is done, with the application of an important strong electric field, either continuous or intermittent, to align all the electric moments in the ceramic.

The above equations directly relate electric charge to the stresses. Hence, the poled ceramics have a capacitive behaviour. More general equivalent circuits including losses (with resistance) and resonance (with coil), describe the electric behaviour of the transducer.

Stresses are produced by the application of a voltage between the two face of the poled ceramic. Hence, the maximum voltage is defined by the maximum dynamic elastic strength and can be calculated in a straightforward way, given the material properties.

Appendix B

Transmitter power and receiver sensitivity

The minimum transmitting power and the minimum receiving sensitivity are computed for a desired signal-to-noise ratio, given an ultrasonic model. The following quantities are defined:

P : The signal pressure level in Pascal.

T^* : The transmitting response amplitude spectrum of the transmitter in $\mu\text{Pa}/\text{V}/\text{Hz}$ re 1m.

T : The transmitting response of the transmitter in $\mu\text{Pa}/\text{V}$ re 1m.

V_T : The voltage drop provided to the transmitter (an heaviside function is assumed).

R^* : The sensitivity amplitude spectrum of the receiver in $\text{V}/\mu\text{Pa}/\text{Hz}$.

R : The sensitivity of the receiver in $\text{V}/\mu\text{Pa}$.

V_R : The receiver voltage output.

N^* : The ultrasonic noise amplitude spectrum in $\text{V}/\mu\text{Pa}/\text{Hz}$.

N : The ultrasonic noise level in $V/\mu\text{Pa}$.

Ne^* : The equivalent input electronic noise amplitude spectrum in V/Hz .

Ne : The equivalent input electronic noise level in V .

f_c : The recorded medium frequency.

b : The recorded bandwidth.

d : The travel distance for a given ray.

l : The ray losses including reflection, transmission, frequency independent scattering and absorption losses.

sn : The desired signal-to-noise ratio, defined for peak-to-peak signals.

It is easier to deal with the decibel notation and the quantities are labeled with a preceding capital L. For example $LN = 20\log(N)$ is the noise level in db. The reference values are 1m for the distance, $1\mu\text{Pa}$ for the pressure and 1Hz for the frequency.

A flat frequency response in the sensitivity of the receiver (figure B-1) and a 40db/decade positive slope in the transmitting frequency response of the transmitter (figure B-2) are assumed. Similarly, white ultrasonic and electronic noise are assumed, although this assumption is not quite true (figure B-3). Then

$$LN = LN^* \quad (\text{B.1})$$

$$LNe = LNe^* \quad (\text{B.2})$$

$$LR = LR^* \quad (\text{B.3})$$

$$T = \frac{1}{b} \int_{f_c-b/2}^{f_c+b/2} T^*(f_c) \left(\frac{f_c}{f}\right)^2 df = T^*(f_c)(1 + T_b) \quad (\text{B.4})$$

i.e.,

$$LT = LT^*(f_c) + LT_b \quad (\text{B.5})$$

where we let:

$$LT_b = 20\log(1 + T_b) = 20\log\left[1 + \frac{1}{3b}\left(\frac{(f_c + b/2)^3}{f_c^2} - \frac{(f_c - b/2)^3}{f_c^2}\right)\right] \quad (\text{B.6})$$

It is obvious that (B.5) is only valid if the transmitter has the indicated 40 db increasing slope over the whole bandwidth considered. Then the transmitted pressure level is:

$$LP = LV_T + LT \quad (\text{B.7})$$

The received pressure level is:

$$LP = LV_T + LT - Ld - Ll \quad (\text{B.8})$$

And the receiver voltage output is:

$$LV_R = LV_T + LT - Ld - Ll + LR \quad (\text{B.9})$$

The condition to satisfy the signal to noise ratio is:

$$LV_R \geq \max(LN + LR, LNe) + Lsn \quad (\text{B.10})$$

The equation (B.10) yields first the minimum required receiving sensitivity for a given equivalent input electronic noise. It should be less than the natural ultrasonic noise.

A noise record (figure B-3) averaged 1000 times in the 0-1 Mhz bandwidth in the tank with the SEA hydrophone, has shown that the ultrasonic noise amplitude spectrum is of the order of $1\mu\text{V}/\text{Hz}$. The SEA hydrophone sensitivity amplitude spectrum has been evaluated at -240db re $1\text{V}/\mu\text{Pa}/\text{Hz}$ (with a slight decrease in the low frequency range, however). Then, the ultrasonic noise amplitude spectrum is about $1\text{Pa}/\text{Hz} = 120\text{db re } 1\mu\text{Pa}, 1\text{Hz}$ and the noise level is 120db re $1\mu\text{Pa}$.

The equivalent input electronic noise of the SEA preamplifier is about $0.4\mu\text{V}/\text{Hz}$.

Obviously, the SEA hydrophone fulfills the receiving sensitivity requirement, which is calculated to be -248db re $1\text{V}/\mu\text{Pa}/\text{Hz}$ sensitivity amplitude spectrum, ie -248db re $1\text{V}/\mu\text{Pa}$, if we assume a flat response.

The condition (B.10) included in equation (B.9) now yields the transmitting response of the source, given a specific ultrasonic experiment. To illustrate this computation, and relate it to our laboratory experiment, we assign the following values:

- $V_T = 200 \text{ V}$

- $d = 0.5\text{m}$

- $t = 100$

- $sn = 10$

- $f_c = 225 \text{ Khz}$

- $b = 375 \text{ Khz}$

This gives:

$$LT = 128 \text{ db re } 1\mu\text{Pa/V.}$$

Equation (B.6) gives $LT_b \simeq 7 \text{ db}$ and from equation (B.5), the required transmitting power at 250 Khz is then:

$$LT^*(f_c) = 121 \text{ db re } 1\mu\text{Pa/V.}$$

If this requirement is fulfilled, this means that the waves which undergo a ray travel of 0.5m and global losses of 100, are recorded on a single shot with a signal-to-noise ratio of 10.

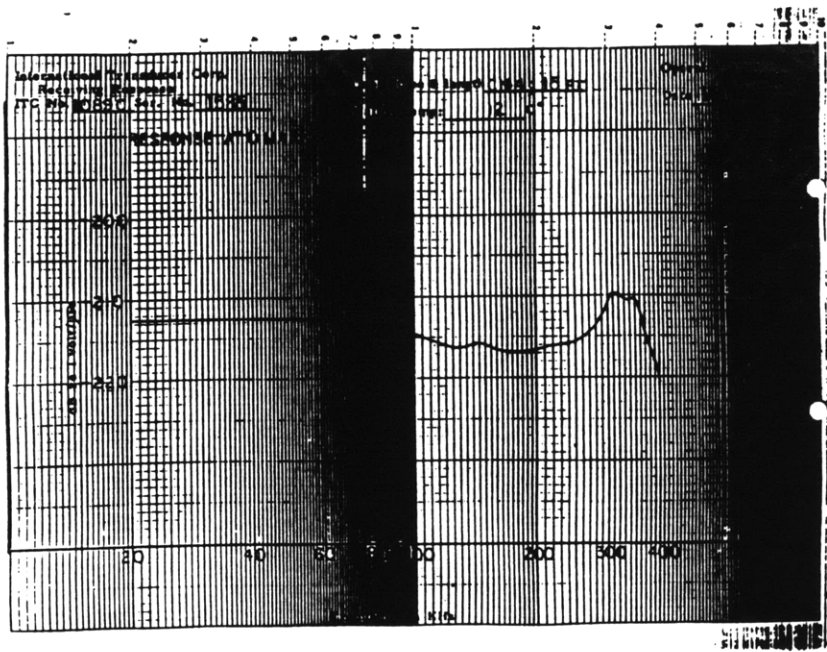


Figure B-1: Typical receiving sensitivity of a piezoelectric transducer (hydrophone ITC 1089) in logarithmic scale.

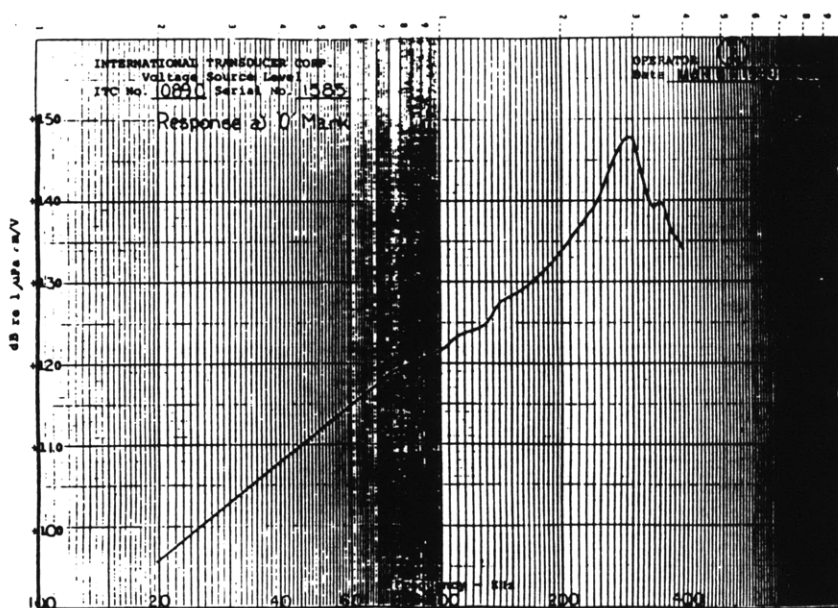
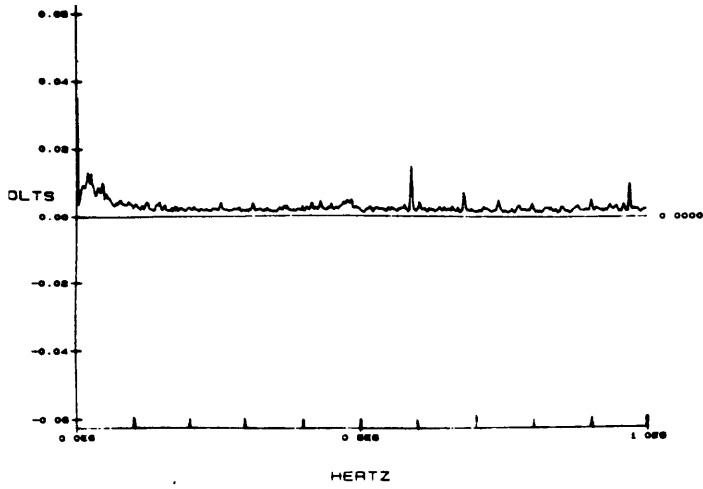
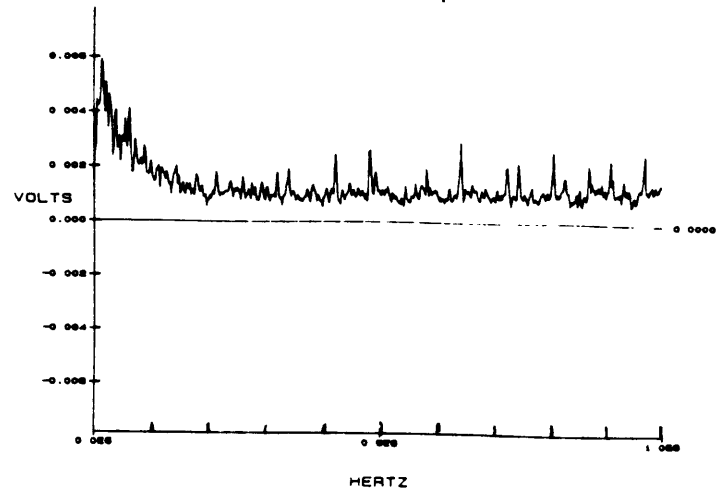


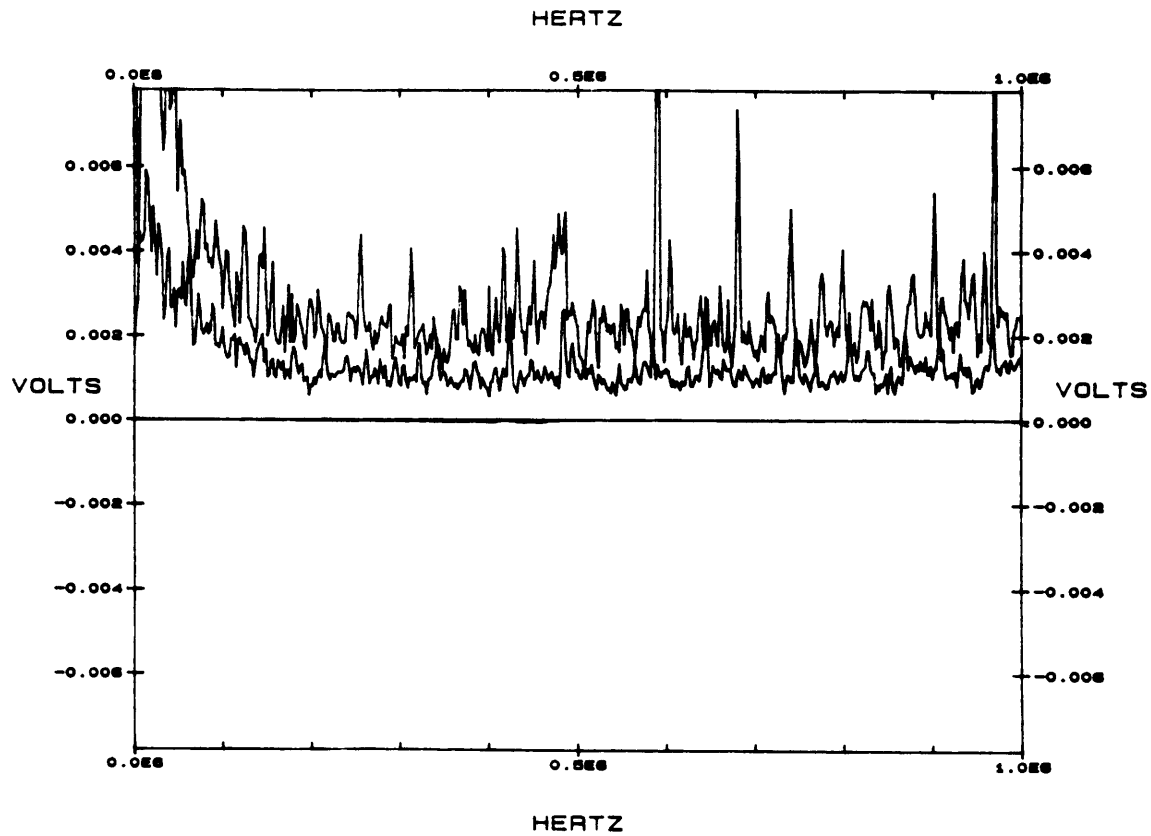
Figure B-2: Typical transmitting response of a piezoelectric transducer (hydrophone ITC 1089) in logarithmic scale.



(a)



(b)



(c)

Figure B-3: Natural ultrasonic and electronic noise. The amplification is 77db. (a) Ultrasonic noise; (b) Electronic noise; (c) Comparison: the ultrasonic is stronger.

Appendix C

Source wavelet improvement

In a pulser, the electric energy, stored in a capacitor is switched shortly (Thyristor switch in the Panametrics pulser) to provide a high-voltage short-time pulse. Such a pulse is shown in figure C-1. During that operation, the ratio between the pulser capacitance and the transducer capacitance influences the energy transfer and the source wavelet quality. Ideally, it must be large. Others passive elements can be used to improve the energy transfer. For example, in the Velonex pulser, an inductive coupling between the two capacitors is provided. More generally, it may be quite interesting to further develop a complete coupling device, designed with passive components to improve the source wavelet. This device may be a smooth notch filter at the resonant frequency of the transducer. For example, figure C-2 shows the pulse shape when the ITC 1089 is connected. In this case, the pulser does not act as a pure voltage source and is pertubated by the oscillations of the hydrophone signal.

A frequency sweep of several μs , delivered to the transducer by a frequency generator and a voltage amplifier, such as B&K 2713, can be an alternative to the ultrasonic pulse. An interesting advantage is that the source can provide more energy with frequency-sweep signal than with a pulse. This reduces the averaging to obtain a given signal-to-noise ratio. On the other hand, the record length of the oscilloscope can limit the applicability of the method.

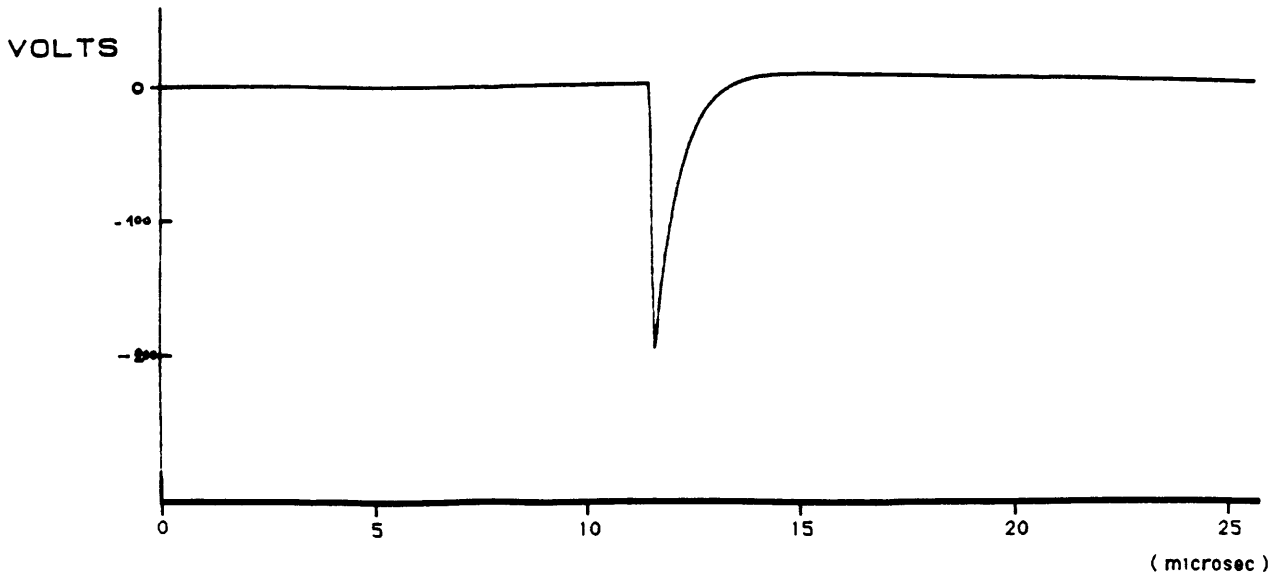


Figure C-1: Panametrics 5055R electronic excitation output pulse. Energy 4, damping 2. No transducer is connected.

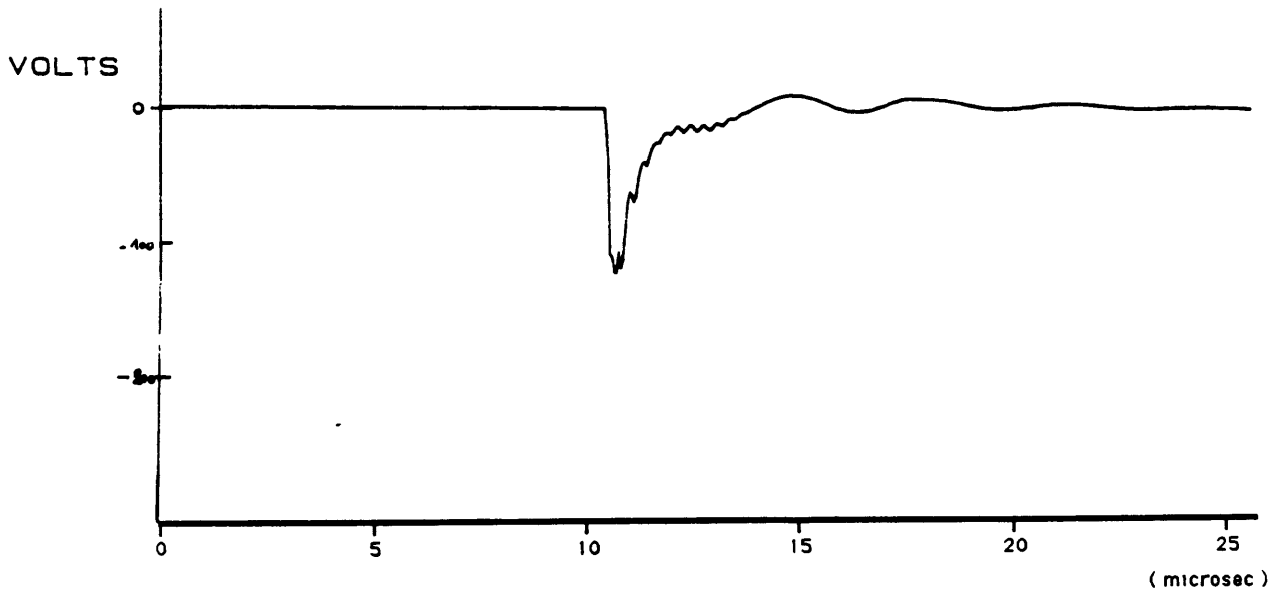


Figure C-2: Panametrics 5055R electronic excitation output pulse. Energy 4, damping 2. The ITC 1089 hydrophone is connected.

Appendix D

Acoustical properties of materials

Without being exhaustive, this table enumerates some of the convenient materials available for modeling purpose.

The properties of three main bonding epoxies is also shown.

Material		V _p (m/s)	V _s (m/s)	Density	Q _p
Metals	Aluminum	6270	3080	2.7	
	Brass	4430	2120	8.1	
	Lead	2220	700	11.4	
	Magnesium	5740	3080	1.7	
	Stainless steel	5790	3100	7.9	
	Titanium	6070	3125	4.5	

Material		V _p (m/s)	V _s (m/s)	Density	Q _p
Plastics	Bakelite	1590		1.4	
	Delrin	2430		1.42	30
	HUVM	2350	1320		
	Lucite	2650	1340	1.2	
	Nylon	2280	980	1.1	
	Nylon 6/6	2620	1070	1.11	30
	Polycarbonate	2270		1.2	24
	Polyethylene	1950	540	0.9	3
	PVC	2310	1080	1.14	12
	Teflon	1350		2.2	4
Epoxies	Araldite	2620		1.16	
	DER 738	2500	1020	1.14	
	Epotek 301	2640		1.08	
Composites	Devcon F	2790	1460	1.58	
	Devcon F2	2800	1420	1.64	
	Devcon F3	2440	1150	1.40	
	Devcon Plastic steel B	2160	1100	1.89	
	Devcon WR	2650		1.63	
Rubber	Neoprene	1600	1000	1.3	50
	Polyurethane	1760	1100	1.96	50
	Sylgard 184 (Silicone)	1030		1.05	

Bonding agents

Epoxy	Viscosity (cps)	Curing condition	Nb of mixing parts
DER 736	10	8 hrs at 70°C	4
VERSILOK	50	2 hrs, room temp	2
EPO-TEK	100	12 hrs, room temp	2

Appendix E

Additional comments on the transmitter

The figure E-2 shows the 48 raw traces and FK filtered time section of the first model recorded with the hydrophone ITC 1089. The acquisition parameters are listed in figure E-1. Although more energetic and quasi-omnidirectional, this transmitter shows some disadvantages for this particular case:

- Its wavelet is not as high resolution as the V323 wavelet.
- Its omnidirectional pattern produces the ghost reflection, which is furthermore angle and frequency-dependent because of the cable output node (figure 2-7), and it emphasizes the edge reflections of the model.

However, it can be valuable when the following conditions are needed:

- Low averaging to increase data acquisition rate.
- True amplitude as a function of angle because of its nearly omnidirectional pattern.
- A large model that requires high source signal amplitude.

- No specific requirements about the shape of the wavelet.

Typical applications include 3D experiments and tomography.

Neoprene-Aluminium Model No 1

3D model experiment No 2

- **Geometry :**

Source line : X

Source intertrace : 1/8"

Nb of source points : 48

Receiver line : O.B.H

Receiver intertrace :

Nb of receiver points : 1

- **Source parameters :**

Transmitter : ITC1089

Pulser : Panamatrix 5052PR

Energy setting : 2

Damping setting : 2

- **Receiver parameters :**

Receiver transducer : Miniature Hydrophone SEA

Preamplifier(s) : SEA + Panamatrix 5660B

Total gain in db : 77 db

Bandpass filter : Krohn-Hite 3202R

Low cut-off frequency : 50 Khz + AC on acquisition

High cut-off frequency : 400 Khz - Max flat -

- **Acquisition parameters :**

Acquisition unit : Ampli D1000 + Oscillo D6000

Time sampling : 400 nanosec

Time delay : 96 microsec

Number of points acquired : 512

Resolution : 12 bits companded

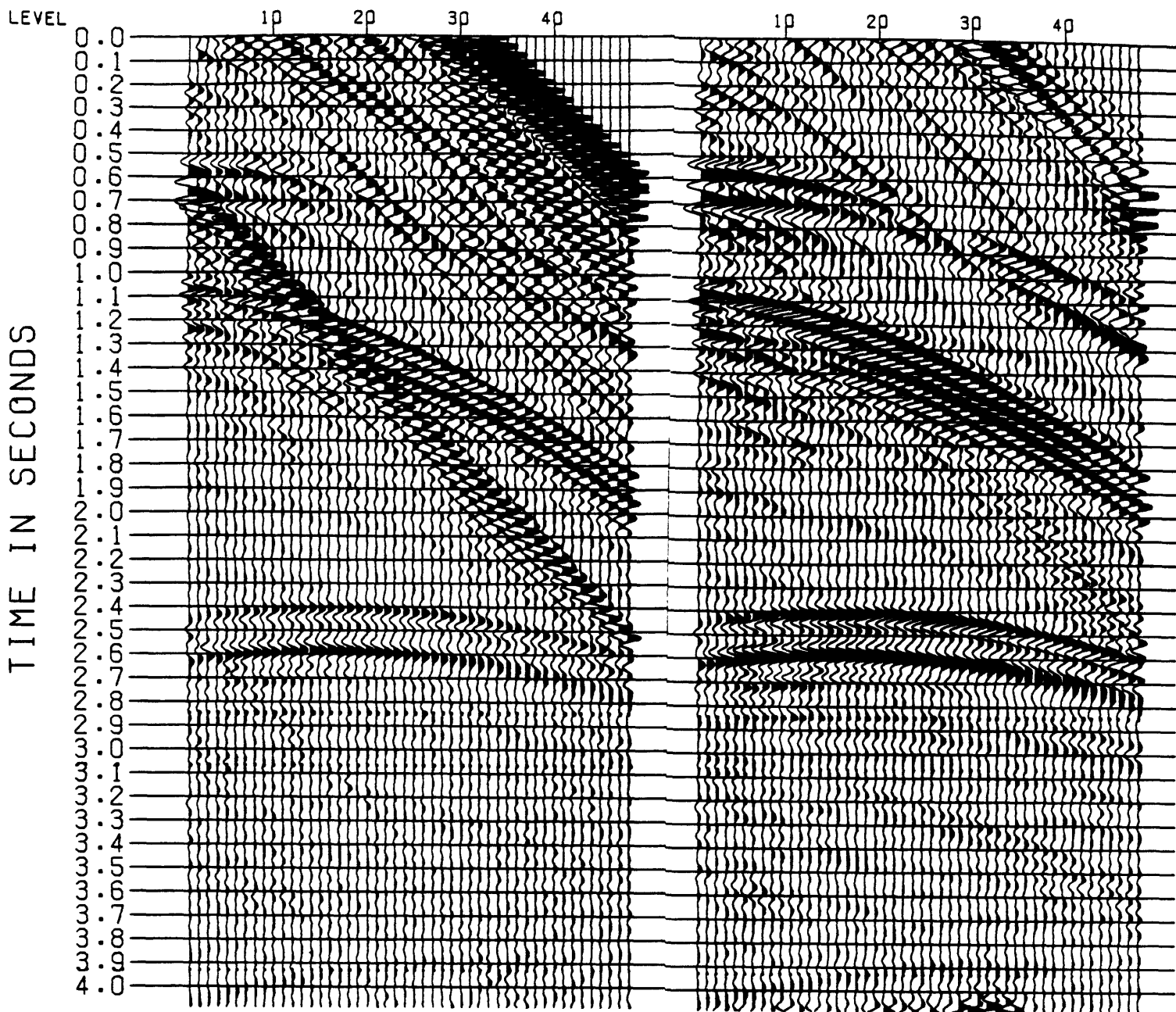
Y full-scale : 1.4 Volts

Y scale amplification : 2

Averaging : 64

Figure E-1: Acquisition parameters.

TIME SECTIONS W/ ITC1089 HYDROPHONE (SOURCE)



RAW DATA SECTION

FK FILTERED SECTION

Scale Factor = 20.000

Starting time = 1.92 sec

Fk Filtering : LP Boxcar 20 hz
+ Fan filter rejection
0 - 1550 m/s

Figure E-2: Raw data and FK filtered time section for the model 1. The ITC 1089 is the transmitter.

Appendix F

Deconvolution of the ultrasonic time sections

F.1 Introduction

The ultrasonic wavelet is not zero-phase and even not minimum-phase. In order to deal with a zero-phase wavelet as it is usually done with synthetic data, the ultrasonic time section has been deconvolved. Although the ultrasonic wavelet (figure 2-11) shows that a high-resolution time section can be achieved, the signature deconvolution operator allows us also to improve this resolution. Time and frequency domain deconvolution are briefly reviewed below and the time domain deconvolution was chosen for our application.

F.2 Time domain deconvolution

F.2.1 Theory

The convolution model is

$$w(t) = s(t) * r(t) * g(t) + n(t) \tag{F.1}$$

where:

- $w(t)$ are the recorded data
- $s(t)$ is the source signature
- $r(t)$ is the impulse response of the recording system
- $g(t)$ is the impulse response of the earth
- $n(t)$ is noise, usually white

The signature signal is recorded and the Wiener filter $f(t)$ is designed. This filter gives the closest output $d'(t)$ to the desired wavelet $d(t)$ with a least-square fit, when convolved with the signature $s(t)$. We have:

$$[d'(t) - d(t)]^2 \text{minimum} \quad (\text{F.2})$$

with

$$d'(t) = f(t) * s(t) \quad (\text{F.3})$$

the deconvolution is performed by:

$$w'(t) = w(t) * f(t) = d'(t) * r(t) * g(t) + f(t) * n(t) \quad (\text{F.4})$$

In the ideal case where $n(t) = 0$ and $r(t) = d'(t) = \delta(t)$ then:

$$w'(t) = g(t) \quad (\text{F.5})$$

A typical algorithm use Topplitz matrix inversion (Ziolkowski, 1984).

F.2.2 Application

The signature chosen to be deconvolved (figure F-1) is a little bit different from the directly recorded ultrasonic wavelet in water (figure 2-11). Indeed, the receiver multiple reflection in the time section of the first model (figure 3-8) is used to get

the signature $s(t)$ to be deconvolved. That choice is made to take into account the change in the ultrasonic wavelet shape due to the absorption in the neoprene. A time alignment (such as a NMO) of 50 traces and their sum were implemented in order to recover the reflected wavelet out of the complexity of the wavefield (figure F-1). A truncation, justified by the character of the wavelet in figure 2-11 gives finally the signature chosen. This procedure allows a better deconvolution than with the wavelet of figure 2-11.

The desired wavelet $d(t)$ is an harmonic function modulated by a zero-phase Gaussian envelope such as the wavelet used in the synthetics seismograms. However, the Gaussian damping has been increased to take advantage of the deconvolution procedure. The frequency of the harmonic function is the dominant frequency of the signature $s(t)$ so that the amplitude spectrum of $d(t)$ does not differ too much from the amplitude spectrum of $s(t)$. Theoretically, best results, in terms of signal-to-noise ratio, are achieved in such a case. The Wiener operator has a 0.8 sec length and produces the wavelet output $d'(t)$ (figure F-1) when convolved with the signature $s(t)$. The signal-to-noise ratio is acceptable although we get some noise 0.4 sec after the wavelet $d'(t)$.

F.3 Frequency domain

The deconvolution problem involves a spectral division, specifically:

$$\frac{w(\omega)s^*(\omega)d(\omega)}{|s(\omega)|^2 + c(\omega)} = g(\omega)d(\omega) + \frac{n(\omega)s^*(\omega)d(\omega)}{|s(\omega)|^2 + c(\omega)} \quad (\text{F.6})$$

where $c(\omega)$ is a noise stabilisation factor which could be chosen constant (i.e., white) or a function of ω .

TIME IN SECONDS

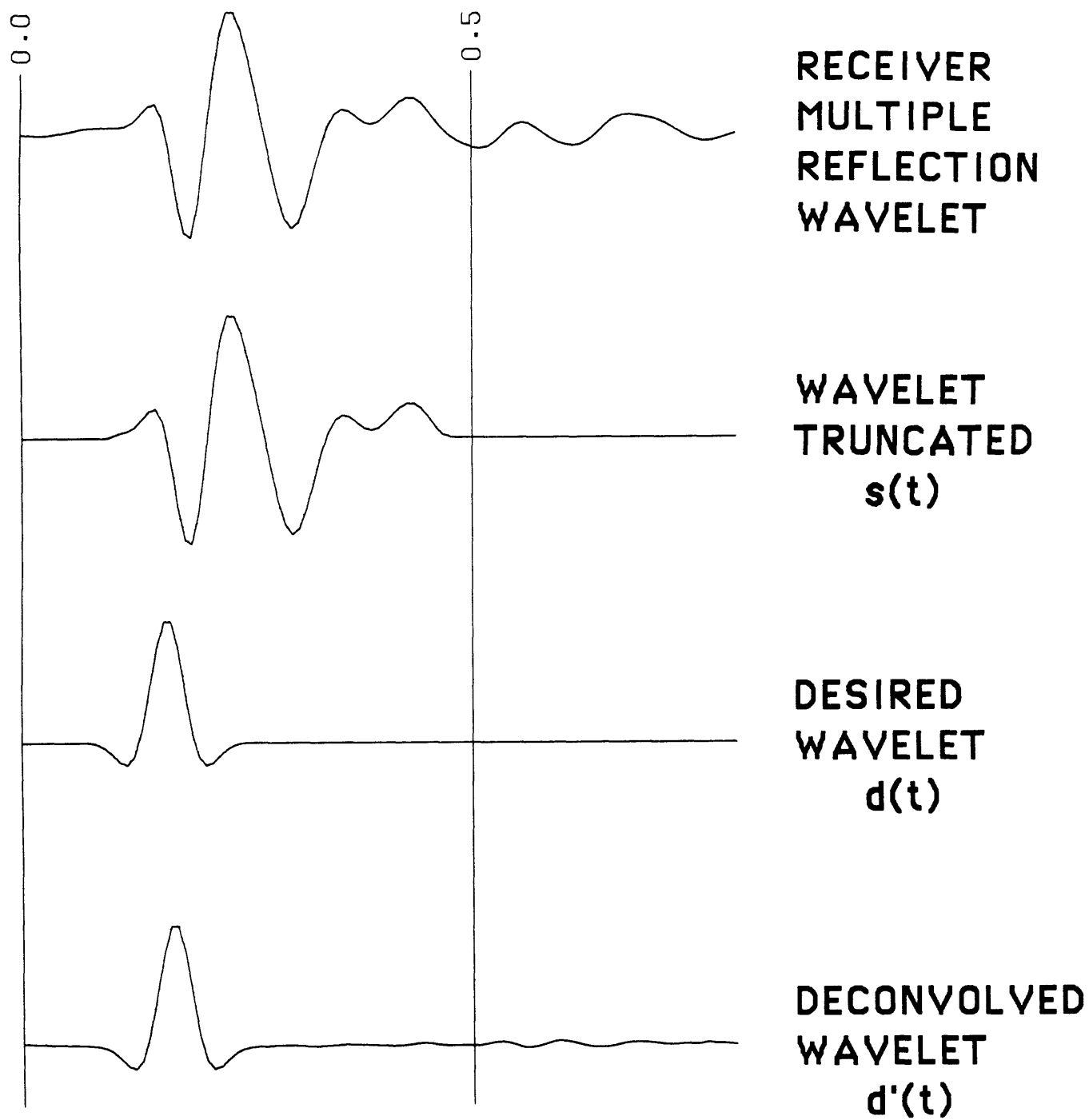


Figure F-1: Wavelets in the deconvolution procedure.

Appendix G

Fault-syncline model

This appendix does not deal explicitly with the thesis subject. However, it is included because it illustrates the resolving power that can be obtained in laboratory modeling. The ultrasonic model is shown in figure G-1 and consists of an aluminum block whose the highly polished surface features a fault dipping 45 degree and a half-syncline with constant second-derivative variations.

The time section in figure G-2 clearly shows the different waves:

- The P head-wave travelling along the aluminum surface.
- The S head-wave, which shows up because the S velocity of the aluminum is greater than the velocity of the water.
- The diffractions due to the corners of the fault.
- The tie-bow character of the syncline.
- The waves issued from the double reflections of the fault and the syncline part of the aluminum surface.

After the primaries, the section shows the complex water-multiple wavefield.

Fault -Synclinal model - Geometry

Front view

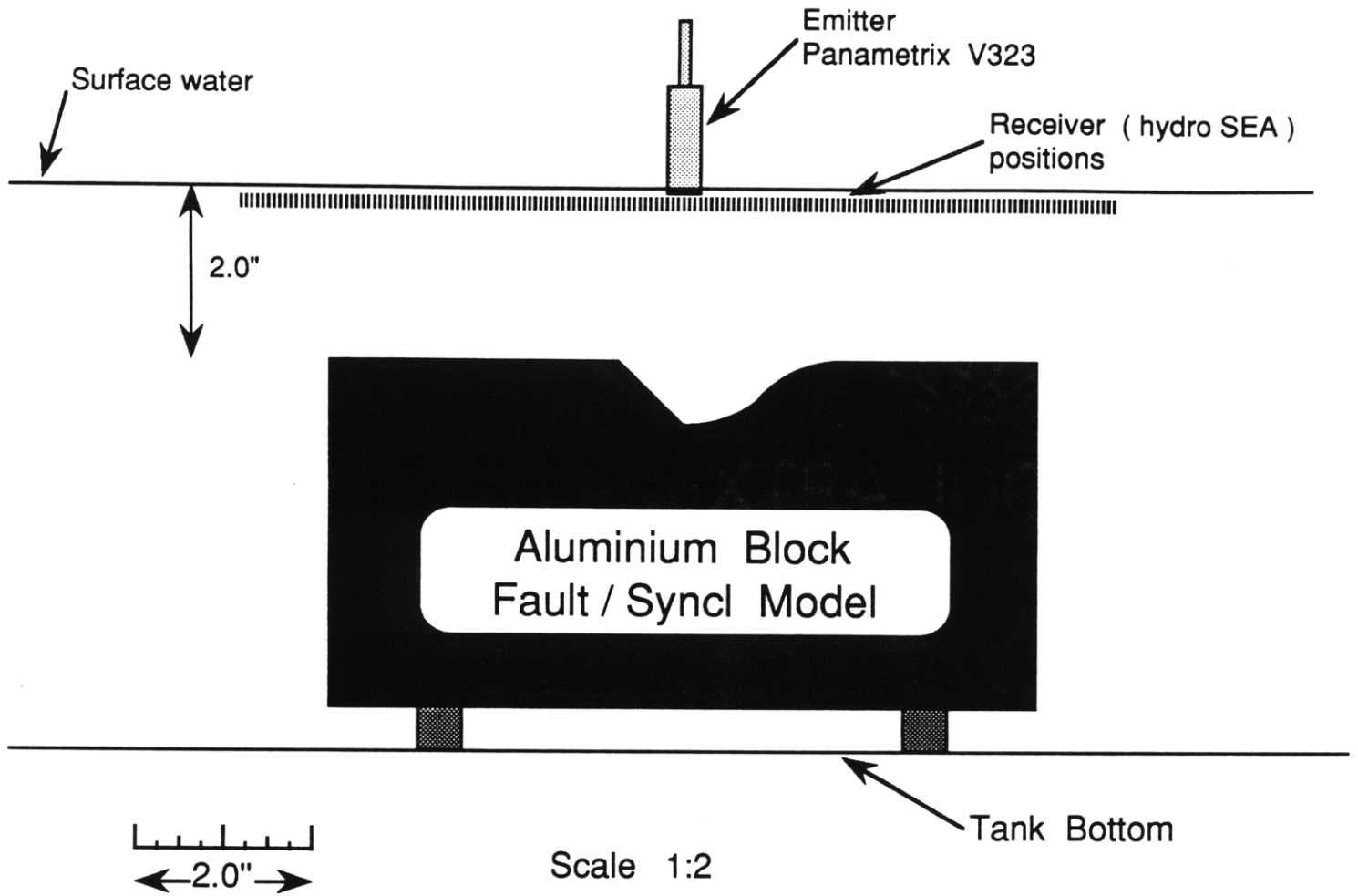


Figure G-1: Experimental set-up for the fault-syncline model.

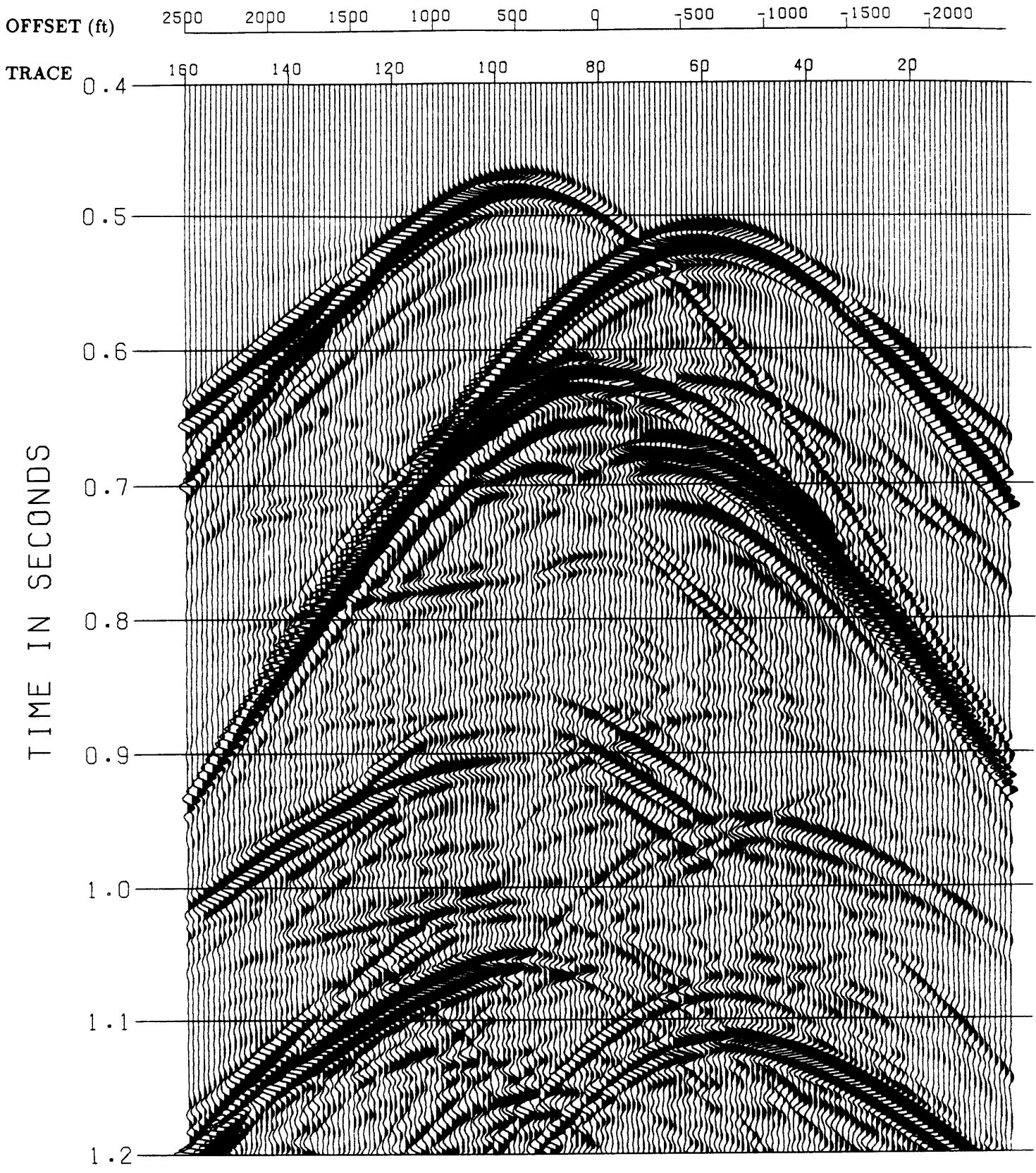


Figure G-2: Raw data time section for the fault-syncline model.

References

- Cervený, V., Molokov, I.,A., and Psencik, I., 1977, *Ray methods in seismology*, Univ. Karlova.
- Hueter, T.,H., 1955, *Sonics, Techniques for the use of sound and ultrasound in engineering and science*.
- Koelsch, D.,E., Peal, K.,R., and Purdy, G.,M., 1982, *A digitally recording ocean bottom hydrophone*, Woods Hole Oceanographic Institution Technical Report.
- Mitchell, A.,R., and Kelamis, P.,G., 1990, *Efficient tau-p hyperbolic velocity filtering*, *Geophysics*, **55**, 619-625.
- Reiter, E.,C., 1990, *Imaging with deep water multiples*, 60th Ann. Internat. Mtg. Soc. Expl. Geophys., Expanded Abstracts.
- Schwab, F., and Burridge, R., 1968, *The interface problem in model seismology*, *Geophysics*, **33**, 473-480.
- Selfridge, A.,R., 1985, *Approximate material properties in isotropic materials*, I.E.E.E transactions on sonics and ultrasonics, **SU-32**, **3**, 381-394.
- Tatham, R.,H., Goolsbee, D.,V., Massell, W.,F., Nelson, H.,R., 1983, *Seismic shear-wave observations in a physical model experiment*. *Geophysics*, **48**, 688-701.
- Toksöz, M., N., and Schwab, F., 1964, *Bonding of layers in two-dimensional seismic modeling*, *Geophysics*, **29**, 405-413.
- Ziolkowski, A., 1984, *Deconvolution* ,